Delft University of Technology

Creep of alkali-activated fly ash and slag concrete
Unveiling multiscale dynamics

Kostiuchenko, A.

Important note
To cite this publication, please use the final published version (if applicable).
Please check the document version above.

CREEP OF ALKALI-ACTIVATED SLAG AND FLY ASH CONCRETE UNVEILING MULTISCALE DYNAMICS

ALBINA KOSTIUCHENKO

CREEP OF ALKALI-ACTIVATED FLY ASH AND SLAG CONCRETE

UNVEILING MULTISCALE DYNAMICS

CREEP OF ALKALI-ACTIVATED FLY ASH AND SLAG CONCRETE

UNVEILING MULTISCALE DYNAMICS

DISSERTATION

for the purpose of obtaining the degree of doctor
at Delft University of Technology
by the authority of the Rector Magnificus Prof.dr.ir. T.H.J.J. van der Hagen
chair of the Board for Doctorates
to be defended publicly on
Tuesday 18 June 2024 at 12:30 o'clock

by

ALBINA KOSTIUCHENKO

Master of Science in Applied Physics,
ITMO University, St-Petersburg,
born in St-Petersburg, Russia

This dissertation has been approved by the promotors:

Prof. dr. ir. K. van Breugel

Dr. G. Ye

Composition of the doctoral committee:

Rector Magnificus,	chairperson
Prof. dr. ir. K. van Breugel,	Delft University of Technology, promotor
Dr. G. Ye,	Delft University of Technology, promotor

Independent Members:

Prof. dr. ir. E. Schlangen,	Delft University of Technology
Dr. ir. M. Lukovic	Delft University of Technology
Prof. dr. K. Kovler	Technion, Israel
Prof. dr. ing. F. Dehn	KIT, Germany
Prof. dr. ir. M. Hendriks	Delft University of Technology

Acknowledgements

Contents

VIII

List of variables

Roman lower case letters

b	porosity constant	
d_{50}	the particle size	[μm]
f	strength of the material	[MPa]
f_0	compressive strength	[MPa]
f_{01}	the intrinsic strength of non-porous material	[MPa]
f_{cm}	compressive strength of concrete	[MPa]
f_{sp}	splitting strength	[MPa]
h_0	the fictitious thickness of concrete member	[mm]
k	the Boltzmann constant	[J/K]
$n(B/F)$	power factor depended on the precursor ratio	[-]
n_0	material constant	[-]
p	porosity of the material	[%]
p^*	proportionality factor	[-]
p_0	the hypothetical value of capillary porosity	[%]
t	the duration of the test	[days]
t'	the age of concrete when the sustained load is applied	[days]
t_0	characteristic time of the shrinkage function	[days]
t_0^*	the characteristic time of creep coefficient function	[days]
t_0'	the characteristic time of creep strain function	[days]
u	the perimeter of the concrete member in contact with the atmosphere [mm]	[mm]

Roman capital case letters

$1/C$	the simulated creep constant	[GPa^{-1}]
A	the cross-sectional area of concrete sample	[mm^2]
A^*	the pre-exponent factor in activation	[mol^{-1}s^{-1}]
B	strength constant	[MPa]
B'	fitting parameter	[-]
B''	fitting parameter	[-]
C	the empirical ageing factor	

E	elastic modulus	[GPa]
E_{28d}	the 28 days elastic modulus	[GPa]
E_{ci}	the elastic modulus measured during the creep tests	[GPa]
E_i	the elastic properties of the diamond nanoindenter	[GPa]
G	shear modulus	[GPa]
$J(t,t')$	creep compliance function at time t induced by a unit stress σ acting from time t'	
K	bulk modulus	[GPa]
$L(t)$	the length of the concrete specimen (prism)	[mm]
L_0	length of the concrete specimen at the start of the test	[mm]
N	the number loading cycles	[-]
N_0	characteristic 'time' (specific number of loading cycles)	[-]
N_A	the Avogadro constant	[mol^{-1}]
Q	activation energy	[kJ]
R	the gas constant	[J·K^{-1}·mol^{-1}]
S_{BET}	the specific surface area	[mm^2]
T	temperature	[K]

Greek lower case letters

α_1, α_2, α_3	parameters calculated from the compressive strength f_{cm}	
$\beta(t')$	creep coefficient factor related the age of concrete at time of loading t_0	[-]
$\beta(f_{cm})$	creep coefficient factor related to the compressive strength of concrete	[-]
$\beta_c(t,t')$	factor that describes the development of creep with time	
β_H	a creep coefficient factor related to the relative humidity RH	[days]
β_{RH}	the factor depending on the relative humidity	[-]
γ	unit-cell angle	[°]
$\varepsilon(N)$	creep deformation (modelling)	[-]
$\varepsilon(t,t')$	the total measured strain	[-]
ε_0	the ultimate value of shrinkage strain	[-]
ε_{el}	the (initial) elastic strain	[-]
ε_{ci}	the instantaneous elastic strain observed in the creep tests	[-]
$\varepsilon_{sh}(t,t')$	the free shrinkage strain of a concrete specimen	[-]

ε_a	instantaneous strain	[-]
ε_{cc}	basic creep strain	[-]
ε_{cs}	the total shrinkage strain	[-]
ϕ	basic creep coefficient	[-]
ϕ_0	ultimate creep coefficient	[-]
φ_0	the notional creep coefficient	[-]
$\varphi_{0,AAC}$	the AAC creep coefficient factor	[-]
φ_{RH}	the factor for the effect of relative humidity RH	[-]
ν	Poisson's ratio	[-]
σ, σ_0	applied stress	[MPa]
τ_0	the shear stress	[GPa]

List of abbreviations

AAC	alkali-activated concrete
AAM	alkali-activated materials
ACI	American Concrete Institute
ASTM	American Society for Testing and Materials
BET model	Brunauer-Emmet-Teller model
BJH model	Barret–Joyner–Halenda model
CASH/C-A-S-H	calcium aluminosilicate hydrate
CSH/C-S-H	calcium silicate hydrate
EC	Eurocode
ESEM	environmental scanning electron microscope
FA	fly ash
FF	force field
GGBFS/GBFS/BFS	ground granulated blast furnace slag
GULP	General Utility Lattice Program
HD- /LD-gel	high density/low density gel
IR analysis	infrared analysis
LAMMPS	Large-scale Atomic/Molecular Massively Parallel Simulator
l/b	liquid-to-binder ratio
MCL	mean chain length
MD	molecular dynamics
MIP	mercury intrusion porosimetry
MC2010	the fib Model Code 2010
NASH/N-A-S-H	sodium aluminosilicate hydrate
NMR spectroscopy	nuclear magnetic resonance spectroscopy
OPC/PC	(ordinary) Portland cement
PBC	periodic boundary conditions
RH	relative humidity
RILEM	Reunion Internationale des Laboratoires et Experts des Materiaux
XMPS/MPS theory	(extended) micro-prestress solidification theory
XRD	X-ray diffraction
XRF	X-ray fluorescence

Chapter 1

Introduction

1.1   General

In 2019 the European Commission presented The European Green Deal – a roadmap for making the EU's economy sustainable by turning climate and environmental challenges into opportunities across all policy areas and with an aim of turning Europe into the first climate-neutral continent by 2050 [1]. The industry of construction materials has been forced to mitigate the environmental impact of concrete production. This includes not only better performance of products, but also replacement of traditional ordinary Portland cement (OPC) with low-clinker cement and innovative binders made of locally available materials. In many industrial regions, particularly those recognized for their steel production and coal-fired power generation, alkali-activated materials (AAM) made from industrial by-products have emerged as a very promising contribution to the development of such a new generation of construction materials [2].

The chemical reaction between a solid aluminosilicate precursor and an alkaline activator is well known and has already been applied for a long time. The first mention of "slag-soda based cement" refers to 1895 [3]. Purdon registered the first patent of clinker-free cement consisting of slag and sodium hydroxide in 1940 [4]. The intensive research from 1957 [5] till now made tremendous progress in understanding and controlling engineering properties of AAM [6]. The accumulated experience has created appealing premises for applying alkali-activated concrete (AAC) in construction practice. Modern AAC mixtures show excellent engineering performance and leave much lower carbon trace compared to OPC concrete [7].

Despite its various advantages, AAC is still far from widespread in the market. The introduction of any new construction material requires full certification based on confirmed and reproducible mechanical testing results. Presently, the current version of EuroCode 2 (EN 1995-1-1) [8] does not offer special recommendation for AAC usage.

Furthermore, producers continue to face a lack of experimental data and reliable predictive models concerning the long-term mechanical properties related to volume and shape stability, in particular creep and shrinkage phenomena.

Creep and shrinkage are an issue for ensuring the durability and long-term serviceability of concrete structures. These strains can cause non-negligible deflections in bridges, intolerable shortening of structural elements, surface cracking, and subsequent fracture leading to water penetration and corrosion of reinforcement. Additionally, creep and shrinkage can compromise structural safety by inducing prestressing force losses or stress redistribution, potentially resulting in fracture and loss of structural integrity. For instance, the tragedy of Koror–Babeldaob Bridge in Palau in 1996 was most likely triggered by creep-induced buckling [9].

This study is meant to contribute to the construction industry's acceptance of locally sourced AAC. The thesis seeks to advance the current knowledge about concrete creep, analyze the distinctive features of AAC, and propose a model for predicting the long-term creep in AAC.

1.2 Creep and shrinkage measurement in building materials

Creep is defined as the increasing deformation of structures under the influence of any sort of sustained loading - tension, bending, compression (Figure 1.1). Creep deformations continue to develop even after several years of operation of the structure. The creep that occurs at constant temperature and moisture content of concrete is called basic creep. Simultaneous drying causes additional creep, called the drying creep (or Pickett effect)[10, 124].

Shrinkage also includes a time dependent deformation, which reduces the volume of concrete, without the presence of external forces. Free shrinkage is considered to be the sum of autogenous shrinkage and drying shrinkage. *Autogenous shrinkage* of cement-based systems occurs mainly due to the reaction process during the first weeks after casting and continue up to several months due to creep and self-desiccation [11, 89, 250, 251]. In contrast, *drying shrinkage* and/or *swelling* are the result of moisture exchange with the environment [11, 121, 252].

The measured total deformation $\varepsilon(t,t')$ of a concrete sample under sustained compressive loading, constant temperature and relative humidity conditions can be divided into three linear components: creep strain $\varepsilon_{cc}(t,t')$ from the time of loading t' until time t, the total shrinkage strain $\varepsilon_{cs}(t,t')$, and the instantaneous elastic deformation $\varepsilon_{el}(t')$ at the time of application of the load. In formula form:

$$\varepsilon_{cc}(t,t') = \varepsilon(t,t') - \varepsilon_{cs}(t,t') - \varepsilon_{el}(t') \tag{1.1}$$
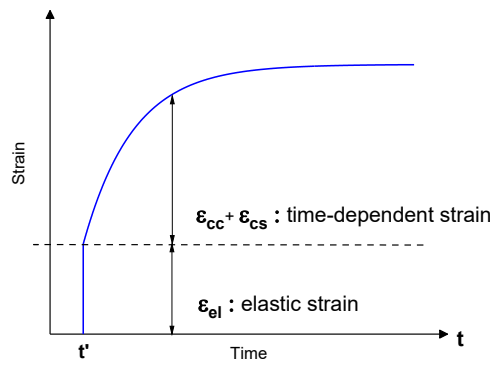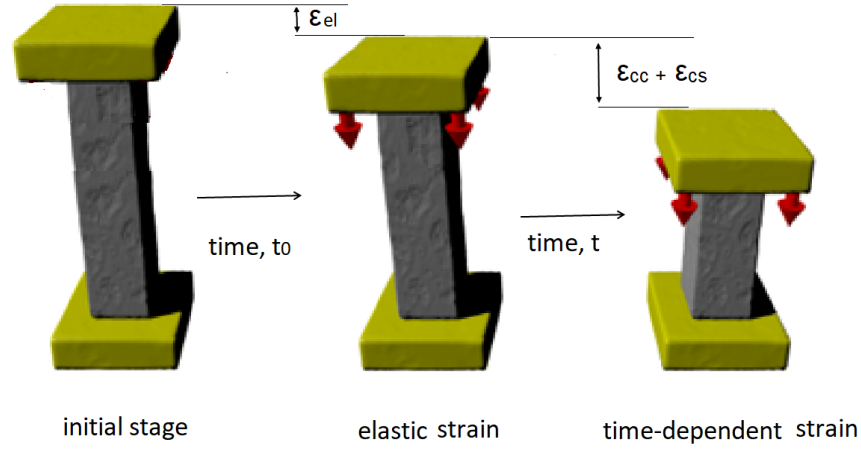
Figure 1.1 Compression creep phenomena illustration. $\varepsilon_{el}(t')$ stands for the instantaneous elastic deformation at the time of application of the load, $\varepsilon_{cc}(t,t')$ is the creep strain from time of loading t' until time moment t, $\varepsilon_{cs}(t,t')$ is the total shrinkage strain.

The magnitude of creep is normally described using the creep coefficient $\phi(t,t')$ and the creep compliance function $J(t',t)$. The creep coefficient ϕ is the creep strain relative to the initial elastic strain:

$$\phi(t,t') = \frac{\varepsilon_{cc}(t,t')}{\varepsilon_{el}(t')} \tag{1.2}$$

The value of creep compliance function $J(t,t')$ is defined as the sum of elastic and creep strains at time t induced by a unit stress σ acting from time t'. For t > t' it holds (if $t < t'$, the value of J must be zero)[10]:

$$J(t,t') = \frac{\varepsilon_{cc}(t,t') + \varepsilon_{el}(t')}{\sigma} \tag{1.3}$$

The creep strain of the tested concrete mixture can be influenced by many factors, such as shape and size of the samples, ratio between compressive strength and applied load, concrete age at time of loading, curing conditions and time, temperature, relative humidity, etc.

15

1.3 Investigation and modelling of creep of AAC

Concrete creep is an extremely broad and complex research topic. Creep mechanisms are still incompletely explored, even after centuries of investigations. Most researchers agree that one of the reasons of concrete creep is *the viscoelasticity* of the cement paste in the concrete. This assumption, supported by accumulated experimental data, enabled the development of fundamental theories of basic creep and the formulation of various models.

In all modern creep theories a relationship between material structure and time dependent behaviour is assumed. In fact, however, the heterogeneous and hierarchical structure of cement-based materials makes concrete creep a multiscale phenomenon, governed by several concurrent mechanisms, such as solidification, grain sliding, dissolution-precipitation, etc. The chemical composition and specific features of the structure of alkali-activated binders imply distinct thermodynamics and kinetics of creep mechanisms, which are not described yet.

The description of each individual mechanism that may contribute to the total creep strain and the kinetics in a single model is extremely complicated. A practical creep prediction model should be simple enough for analysing structural problems. However, theoretical models offer many advantages in terms of physics involved and serve as an essential background for the formulation of a more accurate predictive model.

1.4 Specific features of alkali activated binders

AAMs are obtained by the chemical reaction between reactive aluminosilicate materials (precursors) and an alkaline activator. AAMs were chosen as a possible alternative for OPC in some applications because of many advantages: short setting time, high compressive strength, high fire and acid attack resistance [12, 20, 22].

Unlike hydrated OPC, which primarily forms C-S-H (CaO-SiO_2-H_2O) gel as its main hydration product, alkali-activated materials yield a wide range of reaction products. Typical reaction product of aluminosilicate precursors with high calcium content is C-(A)-S-H (CaO-(Al_2O_3)-SiO_2-H_2O) gel, while a low calcium content generates N-A-S-H gel (Na_2O-Al_2O_3-SiO_2-H_2O) with a pseudo-zeolitic structure (Figure 1.2). The reaction products of a blended system are more complicated. Moreover, the microstructure, morphology and properties of the particular AAC depend on the type of precursor, the amount and concentration of the alkaline solution used for the activator, and the curing temperature. Differences in the structure of reaction product may result in differences in the time dependent behaviour.

(a)   C-S-H gel structure   (b)   N-A-S-H gel structure (pseudo-zeolitic)
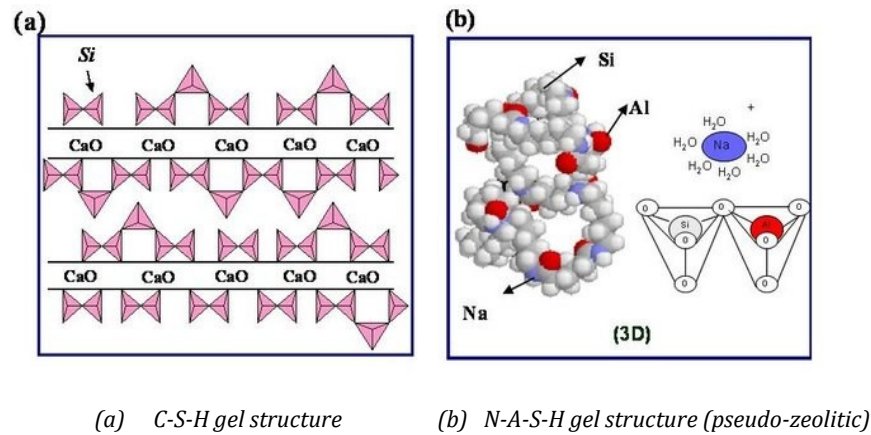
Figure 1.2 Schematic illustration of (a) C-S-H gel structure and (b) N-A-S-H gel structure. Captured from [13].

1.5   Aim, objectives and strategy of the project

The aim of this project is to investigate the shape stability (i.e., creep) of AAC: to clarify creep mechanisms in AAC and to develop recommendations for a creep prediction model for AAC.

In order to reach this aim the following three tasks were defined (Figure 1.3):

1. Measuring creep of alkali-activated concrete.

    Creep tests on concrete specimens were performed in accordance with the standard recommendations [14]. In order to study various influencing factors, the nature and type of precursors, curing conditions and age of samples were considered. The correlations between the influencing factors and creep strains were analysed qualitatively and quantitatively. The results were compared with the results for ordinary concrete of the same strength class.

2. Investigation of creep mechanisms in alkali-activated paste.

    For investigating the mechanisms behind the creep in alkali-activated paste, nano- and microscale analyses were performed: molecular dynamics simulations, characterization of main reaction products by X-ray diffraction (XRD), nanoindentation, porosity measurement by nitrogen adsorption. New insights should be gained about the governing mechanisms of creep in AAC based on the obtained data.

3. Formulation of a creep model for AAC.

    An engineering model for the creep coefficient of AAC will be developed similar to existing models for OPC concrete, taking into account influencing factors and the fundamental material phenomena of AAC.
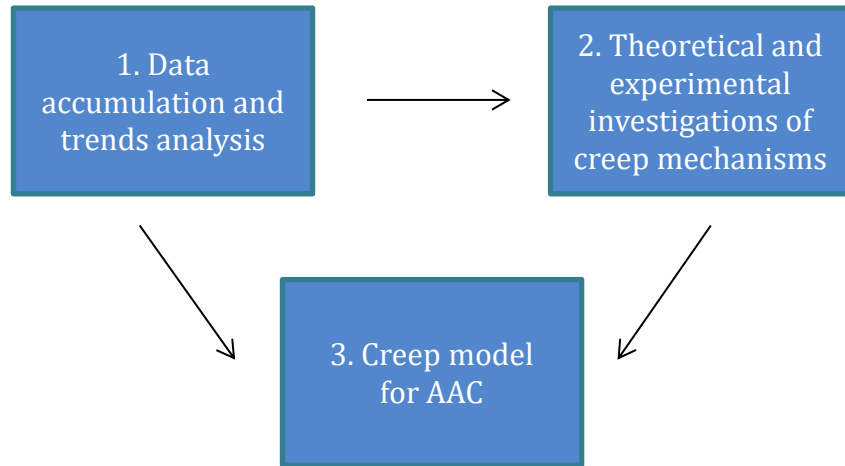
Figure 1.3 Illustration of the project strategy - schematic.

1.6   Research scope and methodology

This study involves the use of both scientific and engineering research methods, as well as experimental and theoretical approaches. For the experimental research, we chose typical precursors, viz.: granulated blast furnace slag (GBFS) and fly ash (FA). Sodium hydroxide and sodium silicate solutions were used as activator. The mixture design of the binders studied in this thesis was developed by Nedeljković [15].

This thesis focuses on investigating and multiscale modelling of the creep process in alkali-activated construction materials. The material behaviour was investigated from the molecular scale (the reaction products level) to the microscale processes (on the paste level) and then to the macroscale (on the concrete level).

The molecular scale simulations were focused on the creep behaviour of the main crystalline reaction products: C-S-H and C-A-S-H structures. The effects of water molecules and Al atoms within the molecular structure were considered.

With the microscale tests the evolution of the microstructure and elastic properties of alkali-activated binder as a function of the precursors' ratio were investigated.

The macroscale tests aimed to measure the evolution of mechanical properties and long-term creep deformation. The experiments were performed under isothermal conditions. The load level during creep tests was set at no more than 40% of compressive strength at 28 days of age, and measurements were performed for one year or more after loading.

1.7 Thesis outline

The chapters are organized according to the project strategy.

The thesis begins with a review of existing theories about creep in concrete (Chapter 2). The text that follows is divided into six chapters:

- Chapters 3 and 4 report the results of tests on mechanical properties and creep and drying shrinkage tests on the selected alkali-activated concrete mixtures. Tests on mechanical properties concern compressive, tensile splitting strength and elastic modulus on the concrete samples of different ages. The results were used for analysis of the influence on creep of the main affecting factors – precursors' composition and curing conditions.

- Chapter 5 summarizes the findings of the microscale experimental investigation of the creep mechanism of alkali-activated binder. The nanoindentation, nitrogen adsorption and XRD technique were used to measure mechanical properties and porosity of alkali-activated pastes.

- Chapter 6 deals with the investigation of the creep phenomenon on the molecular scale. Molecular dynamic simulations of main reaction products of slag-based AAC – C-S-H and C-A-S-H gels – were performed to study the presumed origin of creep at the molecular scale.

- Chapter 7 is dedicated to the modelling of the creep behaviour and formulation of the creep model for AAC.

- The final Chapter 8 summarizes the research results, gives the conclusions and some recommendations for the EuroCode 2 standards and application of AAC.

Chapter 2

Literature review

2.1 Introduction

Time-dependent deformation in concrete structures, such as those due to creep and shrinkage, are hard to avoid. Creep deformations naturally occur under stress generated by permanent loads, such as the dead load of a structure. Creep strains can trigger changes in the stress state and redistribution of initial stresses [10, 121, 125]. The altered stress state may reach a critical level, threatening the integrity of the structure. Stress-induced cracks often occur, leading to mechanical damage of structures. Similar problems appear in bridges. A significant number of bridges showing long-term excessive deflections were documented in the RILEM data bank established by RILEM Committee TC-Multi-Decade Creep [16]. The particularly remarkable case was the deflection of Koror-Babeldaob (KB) Bridge in Palau, which collapsed in 1996, probably as a consequence of creep [16, 17].

These examples of the consequences of creep raise the question how to ensure the long-term serviceability of structures. The conventional method of predicting the long-term mechanical behaviour of a structure involves the use of design codes such as the EuroCodes. EuroCodes specify structural design requirements in the European Union. These codes incorporate models of time-dependent phenomena, including creep. As mentioned in Chapter 1, EuroCode 2 (EC 2) describes creep of concrete using a creep coefficient, which is a function of time and age of the concrete at the moment of loading, taking into account a number of input parameters: temperature, humidity, cross-section area, and compressive strength of the concrete mixture at the age of 28 days [8]. However,

EC 2 was developed for OPC concrete and cannot be applied to any other material without adjustments. The use of EuroCode 2 for AAC without adjustment may lead to overestimation or underestimation of observed creep strains depending on the mixture design [18].

This chapter aims to review the most recent research findings on concrete creep with the certain focus on the differences of creep in AAC and OPC concrete to clarify the mechanisms of creep in AAC. The following information highlights recent scientific results regarding mixture design, reaction products, microstructure and mechanical properties of AAM applicable in structural design. The literature survey is considered comprehensive enough for serving as the current state-of-the-art on the time-dependent behaviour of AAC.

2.2   Alkali activated materials in construction

2.2.1   History

Ancient concrete structures preserved up to the present, which thus have demonstrated excellent durability, were found to contain alkali metal compounds in their cement composition [19, 20]. Unfortunately, the precise recipes of these concrete mixtures have been lost over time. The earliest documented data on a binder mixture containing highly alkaline components, such as granulated blast furnace slag, slaked lime and caustic soda, date from 1895 [3]. Later in the 1900s, H. Kühl presented studies on mixtures of ground slag and a solution of caustic potash [21], and in 1940, A. Purdon published the first extensive laboratory research on cements without OPC clinker, consisting of slag and alkali solution [4].

These preliminary studies inspired Victor Glukhovsky in the 1950s to formulate the hypothesis that compounds of the elements of the first group of the periodic table (alkali metals: Li, Na, K, Rb, Cs) have hydraulic binding properties similar to those of the elements of the second group alkaline (earth metals: Mg, Ca, Sr, Ba) [5]. This hypothesis became a significant step towards the modern scientific approach to alkali-activated materials (AAM). More recent experimental observations [22] have shown that alkali metal hydroxides and salts of alkali metals interact with clay minerals and aluminosilicate glasses to form *water-resistant alkaline and alkaline-earth aluminosilicate hydration products* that resemble natural minerals of zeolite and micac.

In the late 1970s, the French chemical engineer Joseph Davidovits reignited interest in this area by developing alkali-activated binders based on metakaolin, and coined the term "geopolymer" for his products [23]. The high early-age strength that can be achieved by certain combinations of alkali-activation chemistry has drawn interest from the industry, and researchers around the world have developed more detailed scientific foundations for understanding alkali-activation technology [6, 10, 20, 24-30].

Alkali-activated concrete (AAC) is similar to OPC concrete in terms of production process and testing methods, but it also has an essential difference - the replacement of the cement hydration with the alkali activation. In other words, instead of mixing cement with water,

a solid aluminosilicate (the 'precursor') is mixed with an alkali solution ('activator') (Figure 2.1) [6]. Different precursors and activators in various proportion have been tested to optimize the material design [6]. The concrete mixture must be sufficiently workable, while also achieving the required strength within 7 days after casting. Moreover, the long-term mechanical properties and durability of the concrete mixtures must meet standard requirements and norms. For application in the construction industry certain conditions also have to be met, such as the local availability of raw materials in sufficient quantities and acceptable levels of pH of the activation solution. Consequently, the list of raw materials suitable for construction purposes is relatively short, but researchers continue to explore new solutions in this area [31].
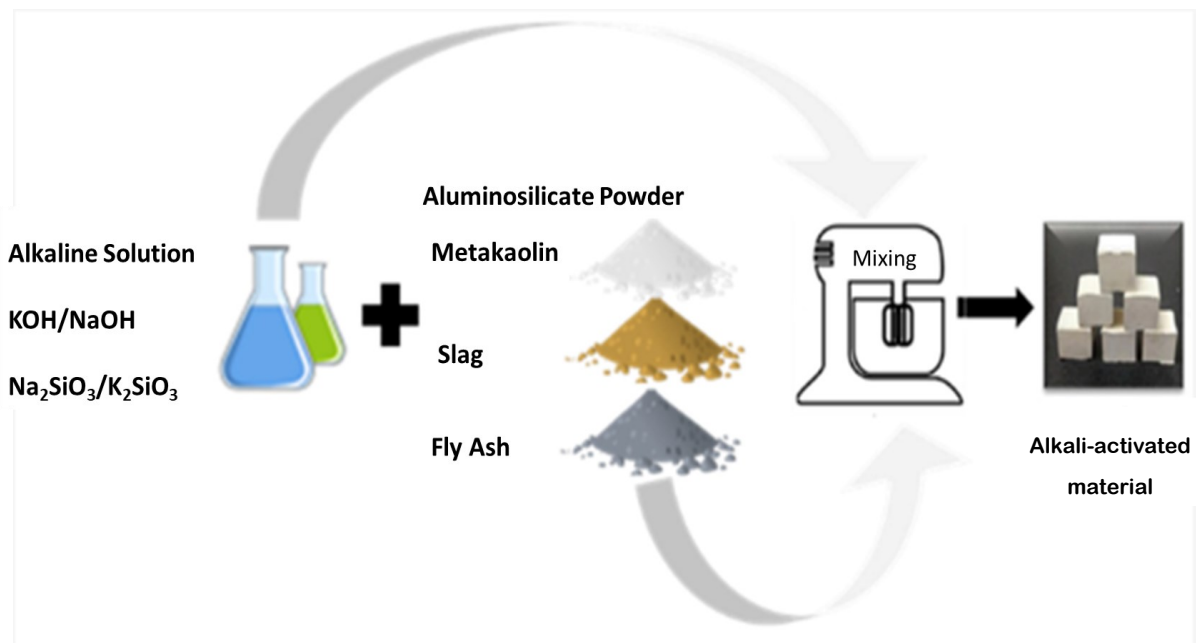
Figure 2.1 Schematic representation of AAM synthesis. Mixing of alkaline solution (activator) and aluminosilicate powder (precursor). Captured from Falah et al.[32].

2.2.2   Mixture design

2.2.2.1 Precursors

AAC mixtures are classified into two main groups, based on the calcium content in the precursors [12]:

1. High-calcium (Ca) precursors with a Ca/(Si+Al) molar ratio of approximately 1 or greater.

   These materials typically contain calcium and aluminum oxides. The most common Ca-rich precursor is slag, which is a non-metallic spin-off material produced during the production of steel [25]. The chemistry and particle size distribution of slag can vary depending on the type and quality of ore [33], [34]. BFS consists essentially of silicates, aluminosilicates and calcium-alumina-silicates. Nedeljkovic [35] showed

favourable use of high-Ca precursors at a moderately alkaline pH and curing the specimens at ambient temperature.

2. Low Ca precursors with Ca/(Si+Al) ratio lower than 1.

   These materials do contain low amount (below 10%) of calcium oxide, but instead contain a high amount of aluminosilicates. They are known as geopolymers, geocements or polysialates [36]. The mineralogical structure of the reaction products is similar to zeolites. The most common materials of this class for construction application are metakaolin and fly ash [12].

Metakaolin is a dehydroxylated form of the clay mineral kaolinite produced by controlled thermal treatment of kaolinitic clay at temperatures between 500 °C and 900 °C [37]. The notable use of metakaolin is due to its high reactivity [38] and low CO_2-emissions during the production process of the binder [34]. However, Kuenzel [39] showed that a high aluminium oxide (Al_2O_3) content leads to high shrinkage. Another disadvantage is its price, which is usually higher than that of other industrial by-products, such as fly ash [40].

Fly ash (FA) is a by-product of burning coal in thermoelectric power generation. It mainly consists of fine spherical aluminosilicate particles (<1–100μm) containing aluminum, silicon, calcium, iron, magnesium chemical components, and carbon wastes [22, 23, 41]. Class F (CaO <7.5%) FA in ASTM C618 or Class V (CaO <10%) in EN 450-1 is an often recommended raw material for synthesizing geopolymers because of its low price and attractive morphology [42, 51]. However, fly ash has extremely low reactivity at ambient temperature and therefore requires high-temperature curing, which consumes a lot of energy (see Section 2.2.3).

2.2.2.2 Activator

The second component of the alkali activation reaction is the alkaline solution (activator).

Alkaline activation is a chemical reaction that occurs when precursors (FA, GGBFS) are mixed with alkaline components (activators). The alkaline activator is commonly based on a compound of very active elements of the first or the second group in the periodic system (Na, K, Ca) [15]. The mechanism of alkaline activation starts with breaking of Si-O-Al bonds of the three-dimensional alumina-silicate network of SiO_4 and AlO_4 tetrahedrons in a strong alkaline environment (pH value above 13) [15]. The type and alkalinity of the activator greatly influence the microstructure of the solidified paste [12].

In his review, Krivenko [25] reported an extensive array of potential activators. However, more recent findings by Provis and Bernal [12] have shown that coupled alkaline activators consisting of sodium hydroxide solution (NaOH) and sodium silicate (Na_2SiO_3) are the most versatile. These activators are very efficient in activating both precursors with high and low calcium content.

2.2.2.3 Reaction products

The dependence of the composition and structure of reaction products on the chemistry and proportion of the precursors and activator used has also been subject of many studies

[12, 43, 44]. It has been shown that the use of NaOH solution resulted in products with higher Ca/Si ratio and a more pronounced crystallinity of the structure than the gel formed in reactions with sodium silicate hydrates [45].

The main reaction products of hardened pastes made from Ca-rich precursors (CaO>10%) were found to be similar to those in OPC: mainly C-S-H and C-A-S-H gels [46-50]. Figure 2.2 illustrates the C-A-S-H gel structure [48]. Similar to C-S-H gel, the C-A-S-H gel structure consists of layers of silicate chains linked tetrahedrically with a Dreierketten structure. The interlayer region contains Ca^{2+} cations, alkalis and water. The water is chemically incorporated into the gel structure. Al^{3+} replaces Si^{4+} in the bridging sites [49]. Accordingly, OH^- groups and alkaline cations balance the generated net negative charge [50].
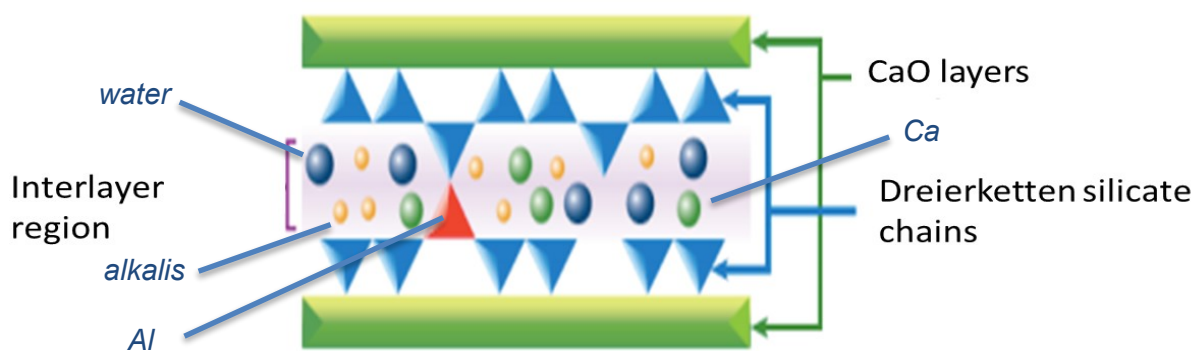
Figure 2.2 Illustration of molecular scale tobermorite-like C-A-S-H gel structure. Captured from [48].

Davidovits [51] described the reaction between low-Ca precursors, such as fly ash, and alkali solution, and called it geopolymerization, which is different from the hydration of OPC. The main reaction product of fly ash geopolymerization is a sodium aluminosilicate hydrate, i.e. N-A-S-H. In general, the structure looks like the three-dimensional network of SiO_4- and AlO_4- tetrahedrons sharing the oxygen atoms [52, 53] (Figure 2.3). The final configuration of the N-A-S-H gel was found to depend on the particular activator and curing conditions [43, 54].
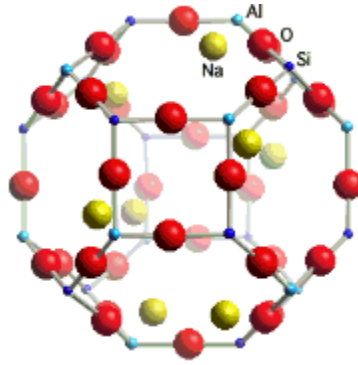
Figure 2.3 Molecular scale geopolymer structure with Na-polysialate. Na-poly(sialates) consist of an amorphous network of tetrahedral SiO_4 and tetrahedral AlO_4 bonded with Na^+ ions. Captured from [53].

In most cases, the concrete mixture contains two or more types of precursors to achieve the desired properties. Many studies have been devoted to investigating the gel formation and structure of pastes made from mixtures of blast furnace slag, fly ash and metakaoline in different proportions [52, 55, 56]. Figure 2.4 shows a ternary diagram of alkali-activated gels as a function of the relative content of CaO, SiO_2 and Al_2O_3.
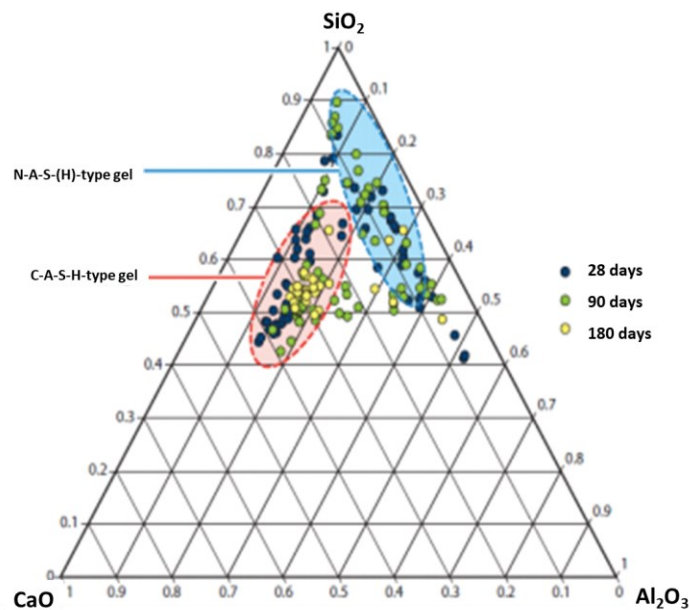
Figure 2.4 Ternary diagram with the elements CaO, SiO_2 and Al_2O_3, and the gels formed in the alkali-activated reaction. Captured from [41] with reference to Ismail et al [52].

2.2.3   Curing conditions

After casting, fresh concrete is exposed to prevailing curing conditions. Concrete curing implies maintaining a pre-defined environment (temperature and relative humidity) to ensure desired evolution of the reaction process at early ages. The concrete surface may be sealed with a plastic film (or by other means) to create a physical barrier to evaporation of moisture from the hardening mixture; or left exposed to free moisture

exchange with the environment. The curing period may vary from several hours to several days. Inappropriate curing conditions may result in carbonation at the concrete surface at a very early stage [57, 58], leading to a decrease of mechanical properties and durability.

The low-calcium alkali-activated pastes harden slowly at ambient temperature. Several studies [15, 28, 59] stated that curing at elevated temperature is necessary for fly ash-based AAC to achieve sufficient reaction rates and mechanical strength development.

Collins et al. [60] and some other research groups [61, 62] investigated the effect of the type of curing on the strength of alkali-activated slag-based concrete. The authors reported that concrete or paste exposed to air curing (RH≤80%), compared to sealed curing at the same temperature and during the same period of time, resulted in a coarser pore size distribution in the material, microcracking of the specimens and a decrease of the compressive strength.

2.3 Mechanical properties of AAC

2.3.1 Compressive strength

Among other mechanical properties, the compressive strength is the most frequently used one by researchers and engineers, as it determines the class of concrete and has often been used as a key parameter for estimating various properties of the concrete. The compressive strength depends on several factors, such as the type and fineness of the aggregates, the liquid-to-binder ratio, reaction products and curing regime [63, 64, 65].

Slag-based AAC has very high early-age strength and rapid strength development compared to OPC concrete. Deng et al. [66] outlines that the 1-day compressive strength can reach 60 MPa and the 1 year compressive strength can exceed 100 MPa.

However, slag-based concrete is sensitive to curing conditions. Collins et al. [60] reported that the compressive strength of slag-based AAC specimens subjected to bath (moist) curing continued to increase until 400 days, whereas the same specimens sealed with plastic film gained little strength, even after 91 days. Specimens subjected to bath curing showed visible microcracking and strength reduction after exposure to ambient conditions (23 °C and 50% RH).

Many studies have shown that partial replacement of slag by fly ash results in a lower compressive strength [67, 68]. The experimental results obtained by Nedeljkovic [15] showed that the 28-day compressive strength decreased from 85 MPa to 58 MPa as the replacement ratio of slag with fly ash increased from 30% to 70%. This difference in strength with the replacement of slag by fly ash is attributed to the low reactivity of FA and a consequently slower formation of reaction products. The hollow unreacted particles of FA create pores in the microstructure due to its too slow precipitation of reaction products to fill the hollow space [52, 67].

2.3.2 Splitting tensile strength

The splitting (tensile) strength is another mechanical property of the concrete used in structural design. The splitting strength can be measured by a splitting tensile test. However, often the splitting strength is estimated through the relationship with the compressive strength f_0 [62, 63, 69]. The EuroCode 2 estimates the splitting strength f_{sp} with the formula $f_{sp} = 0.33*f_0^{0.66(6)}$. The ACI building code 318 proposes the linear relationship with the square root of the compressive strength $f_{sp} = 0.55*f_0^{0.5}$.

Studies show both underestimation and overestimation of the splitting strength of alkali-activated slag-based concrete by the code-type models [62, 69]. Sofi et al. [70] found that the measured splitting tensile strength of slag-fly ash based concrete was overestimated by the ACI Building Code 318. They proposed that a more accurate prediction could be achieved by establishing a relationship with a lower coefficient of proportionality: $f_{sp} = 0.48*f_0^{0.5}$. Similar results with correction of the coefficient of proportionality to 0.45 were found by Lee and Lee [26]: $f_{sp} = 0.45*f_0^{0.5}$.

2.3.3 Elastic modulus

The elastic modulus of concrete is an important parameter for describing the elastic and viscoelastic properties of material. The E-modulus is determined by the microstructure and chemical composition of the binder [63], and is also affected by the type and amount of the coarse aggregate in concrete [71].

Several studies have reported values of the elastic modulus of slag-based AAC [72, 73]. The E-modulus at 28 days was in the same order of magnitude as that of OPC concrete: 15–40 GPa [52]. Some studies, however, reported the modulus of elasticity of slag-based AAC to be marginally lower than that of OPC concrete [60].

Fly ash-based AAC exhibit lower elastic modulus than slag-based AAC [65, 74]. This can be simply explained by the porous microstructure of the binder and mechanical properties of the gels: the Young's modulus of C-S-H and C-A-S-H of the alkali-activated slag is much higher than that of the N-A-S-H gel formed from alkali-activated fly ash [75, 76]. Hence, the partial replacement of slag with fly ash in the concrete mix design also reduces the resulting modulus of elasticity. Prinsse et al. [77] found that blending slag with 50% fly ash reduced the 28-days modulus of elasticity of concrete by almost 15%.

2.4 Time-dependent deformation of concrete - Creep

2.4.1 The creep phenomenon

On loading concrete does not only exhibit a direct elastic deformation, but on top of that also a time-dependent deformation, known as creep (Figure 2.5).

Creep has three stages, defined according to the creep rate: primary, secondary and tertiary creep (Figure 2.6) [10]. Primary creep starts rapidly with high strain rate that decreases with time. Secondary creep progresses at a constant low rate. Tertiary creep is characterized by an accelerated rate of deformation, which terminates when the material

fails (breaks or ruptures). The period until transition into the tertiary stage is very long and does generally not take place during a normal creep tests.

Creep is a fundamental property of concrete that characterizes its capacity to undergo deformation under a constant load over a long period of time. The creep that occurs at constant moisture content of concrete is called *basic creep*. For stress levels (up to 40% of the strength) and at constant moisture content, creep depends linearly on the applied stress σ_0 and can be explained by linear viscoelasticity of the binder [8, 10, 181, 182, 253].
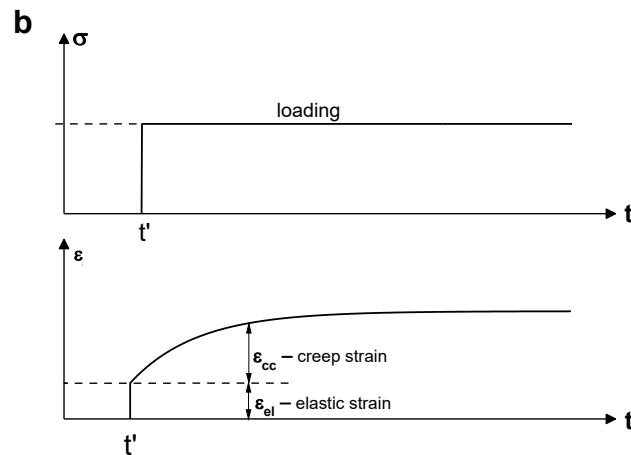
Figure 2.5 Schematic of evolution of basic creep strain with time. σ – loading, ε_{el} the instantaneous elastic deformation at the time of application of the load t', ε_{cc} is the creep strain from time t'.
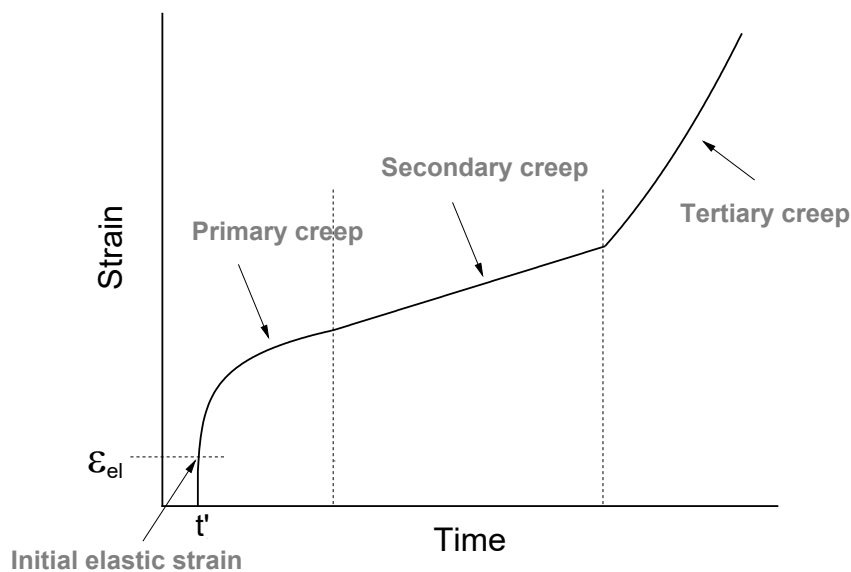
Figure 2.6 Schematic illustration of the creep stages from the time moment t' (including initial elastic strain ε_{el}).

2.4.2 The origin of creep - Activation energy approach

In 1889 Arrhenius proposed that certain reactions or processes must be supplied with *activation energy* in order to proceed [78]. This concept has been applied to describe the time-dependent behaviour of numerous materials, including creep in concrete. It has been postulated that numerous 'centres' at which activation processes occur exist within creeping material [79, 80]. One of the major advantages of this approach is that it does not require the detailed information about the material structure. 'Centres' need only be thought of as regions within a specimen where transformation of the material into a more stable configuration occurs, in other words, where the reduction of stress occurs, which leads to creep strain after overcoming an energy barrier (activation energy Q) (Figure 2.7).
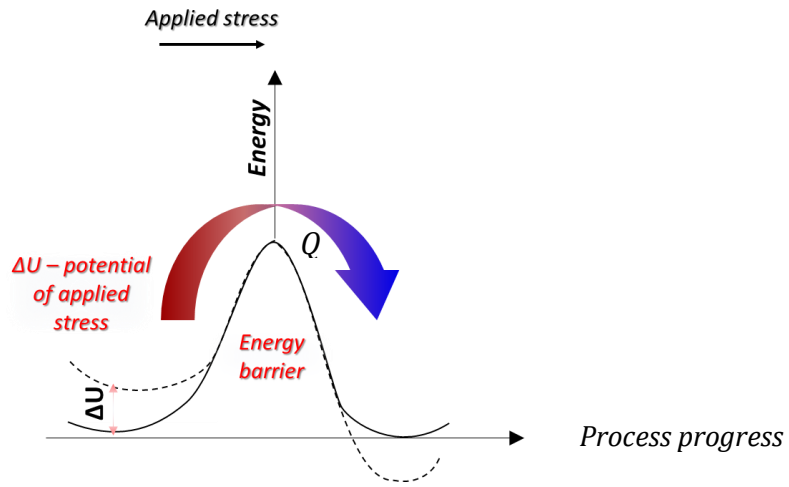
Figure 2.7 Energy landscape of a particular 'centre' with two states. In basal conditions, the states are separated by an energy barrier of height (Q). When an external stress (σ) is applied the energy barrier is lowered from (Q) to (Q-ΔU).

The description of this process as a function of time, t, can vary depending on how the stress is distributed within the material and how it evolves. The simplest case is an exponential decay law expressed as:

$$f_t(t) \propto \exp\left(-\frac{t}{\tau}\right) \qquad (2.1)$$

where $f_t(t)$ is a time-dependent function and τ is known as the characteristic time. This approach can be used to describe both stress relaxation and creep strain evolution [81, 106].

2.4.3 Creep rate

Many empirical functions have been proposed to fit experimental data of creep evolution [82, 83]. The starting point is the assumption that the creep rate can be described through multiplication of two separate functions of applied stress and ambient temperature.

$$\dot{\varepsilon}_{cr} = f_\sigma(\sigma_0)f_T(T) \tag{2.2}$$

The widely used functions of stress are power law [79], power law including the creep limit [84], exponential law [85], and hyperbolic sine law [86]. For low stress values the stress function can be described by the linear dependence on the stress [87]:

$$f_\sigma(\sigma_0) \approx \dot{\varepsilon}_0 \frac{\sigma_0}{n_0} \tag{2.3}$$

where $\dot{\varepsilon}_0$ and n_0 are material constants, that can be experimentally obtained from creep tests .

The dependence on the temperature is usually expressed by the Arrhenius law:

$$f_T(T) = \exp[-Q/kT] \tag{2.4}$$

where Q and k denote the activation energy and the Boltzmann constant, respectively.

2.5 Creep in heterogeneous cement-based systems

2.5.1 Proposed creep mechanisms

Various mechanisms have been adopted for explaining the time-dependent behaviour of heterogeneous systems, such as concrete [88-90]. Currently, however, there is no single comprehensive theory that can unify and define the relationship between these different mechanisms operating simultaneously or sequentially. Bažant [88] mentioned 7 mechanisms causing or influencing concrete creep:

1. Plastic flow.
2. Consolidation theory.
3. Load-bearing hindered adsorbed water.
4. Bond breakage in slip and its reformation.
5. Nonlinear deformations and cracking as a contribution to Pickett effect.
6. Solidification theory for short-term aging [91].
7. Microprestress of creep sites in cement gel microstructure, causing the Pickett effect and long-term aging [92].

The heterogeneous structure of concrete leads to complex stress and strain distributions throughout its volume. At different locations within a concrete body different mechanisms with different kinetics may be dominant. When subjected to an external load, however, the concrete responds macroscopically as a single system, and the resulting evolution of strain can be monitored and can generally be described by an exponential law.

The last two mechanisms from the list above are sufficient in most cases to adequately describe most of the experimental measurement of creep in hardening concrete [88]. These two mechanisms became the foundation of the micro-prestress solidification (MPS)

theory of creep [92]. The MPS theory gave satisfactory predictions of the long-term creep of concrete [93]. The studies of Vandamme et al. [94] and Sinko et al. [95, 96] allowed to develop the extended MPS (XMPS) [97], which further improved the reproduction of the creep process.

2.5.2 MPS (microprestress solidification) theory

The ideas on microstructure evolution that anticipated *microprestress-solidification* (MPS) theory were firstly suggested by Ghosh in 1971 [98, 99]. Later, Bažant proposed the hypothesis on concrete aging [100, 101] and formulated a solidification theory [91, 102]. The solidification theory of concrete creep is a fundamental concept in the study of the long-term behaviour of concrete. The solidification theory reflects the hydration process of OPC concrete, which leads to the formation of new gel layers in the pores. It is assumed that the mechanism of creep of solidifying gel is non-aging viscoelasticity.

MPS theory [92] is an extension of the above-mentioned solidification theory. According to the MPS theory the microprestress is caused by high local shrinkage, and suggests that locally acting stresses within the material, known as microprestresses, can relax over time due to a process called viscous shear slip. This occurs when opposite walls of nanopores in the concrete slide pass each other, breaking the bonds or bridges that cross these pores and form them again in a slightly different arrangement.

To simplify mathematical description, the total strain ε of concrete under the sustained stress σ can be expressed as the sum of the instantaneous strain ε_a, the viscoelastic strain ε_v, the purely viscous strain ε_f, the shrinkage strain ε_{sh}, and the thermal strain ε_T. Thus, the total strain can be expressed as [92]: $\varepsilon = \varepsilon_a + \varepsilon_v + \varepsilon_f + \varepsilon_{sh} + \varepsilon_T$. In this way the separation of solidification and microprestress greatly simplifies the related rheological model of creep, which is illustrated in Figure 2.8. The instantaneous strain is modelled by the elastic element, the viscoelastic strain (solidification) is modelled by a series of Kelvin-Voigt elements. The purely viscous strain is modelled by an aging dashpot, the flow (purely viscous) strain is modelled by a viscous flow element coupled in series to the elastic spring, the solidifying Kelvin chain and a viscous dashpot with age-dependent viscosity, the shrinkage strain rate is proportional to the RH and the thermal strain is proportional to the thermal coefficient α_T.

According to MPS theory the creep compliance function $J(t,t')$ can be written as [104]:

$$J(t, t') = q_1 + J_v + C_v(t,t') \tag{2.5}$$

where $q_1 = 1/E_0$ represents the elastic term (the spring with elastic modulus E_0 in Figure 2.8); $C_v(t,t')$ is the solidifying viscoelastic term, which is the volume growth function describing the solidification process (the Kelvin chain with elements, consisting of springs with elastic moduli E_j and dashpots with viscosities η_j in Figure 2.8); J_v represents the irrecoverable viscous flow term (the dashpot with age-dependent viscosity S in Figure 2.8).

With an adequate experiment data set, the model parameters (E_i, η_i, S) can be determined by fitting; in the absence of experiment data, they can be roughly estimated via empirical formulas for OPC concrete [104, 105].
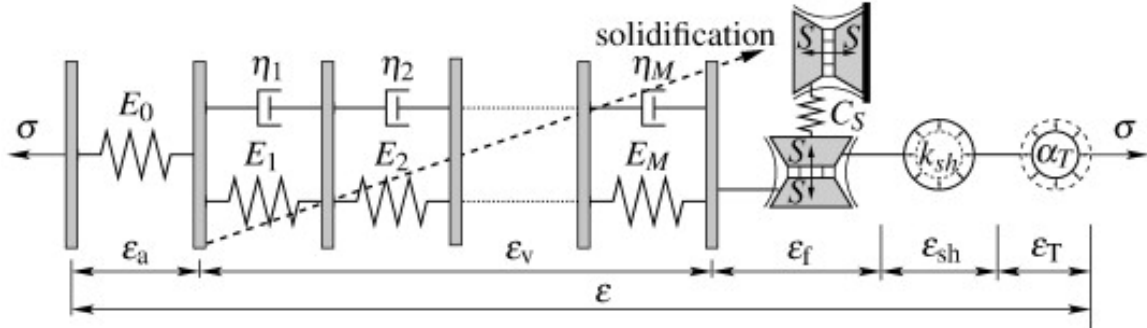
Figure 2.8 Rheological model of creep according microprestress solidification (MPS) theory. A nonaging spring unit representing instantaneous elastic strain ε_{el}; a solidifying kelvin chain unit representing the viscoelastic response with aging ε_v; a dashpot unit with viscosity dependent on microprestress ε_f; a shrinkage unit representing shrinkage strain ε_{sh}; and a thermal unit for thermal strain ε_T. The units are connected in series, with the identical stress σ. Captured from Jirásek et al. [103].

2.5.3   XMPS (extended microprestress solidification) theory

Extended microprestress solidification (XMPS) theory is an extension of the MPS theory described in the previous section. The XMPS theory, including the rheological model, was described by Rahimi-Aghdam et al. [97]. In the XMPS theory, the authors distinguish between nanoscale and macroscale viscosities. In the XMPS the flow term in equation (2.5) is a function of the macroscale viscosity, which serves as a parameter for the microlevel theory, given the rheological nature of the model. Macroscale viscosity depends not only on the microprestress but is also affected by the moisture, which is stated in the pores. [97]. To account for the effect of temperature on relative humidity in the pores, they use a humidity-dependent hygrothermic coefficient $\kappa = \partial h/\partial T$ [106, 107, 108].

2.6   Nano- and molecular scale models of creep

2.6.1   Nanoscale mechanism of concrete creep

The nanoscale mechanisms of creep in concrete are rooted in the colloidal nanostructure of the paste. Hardened cement paste in OPC concrete forms a non-homogeneous nanoporous network of colloidal particles of mostly calcium silicate hydrate (C-S-H), which consists of domains of low and high packing density. These regions are often referred to as LD-C-S-H (low density) and HD-C-S-H (high density), respectively [109, 110].

Three mechanisms have been proposed to explain creep behaviour in the paste of OPC concrete on the nanoscale: shear deformation of the individual C-S-H colloidal particles [111], sliding of the C-S-H colloidal particles [112], and the formation of micro- and nanocracks in the paste [113].

Haist et al. [114] showed that, as far as creep is concerned, LD- and HD-C-S-H phases behave as single granular phases. For both types of C-S-H phases, the major creep mechanism is the viscous slippage between C-S-H nanoparticles [112] separated by nanoconfined water layers (see Figure 2.9). The authors suggest that when there is enough water between globules, the sliding of the globules becomes the primary creep mechanism. In this scenario, the role played by microcracking of the paste and deformation of the individual C-S-H particles in the total creep deformation is negligible [90].
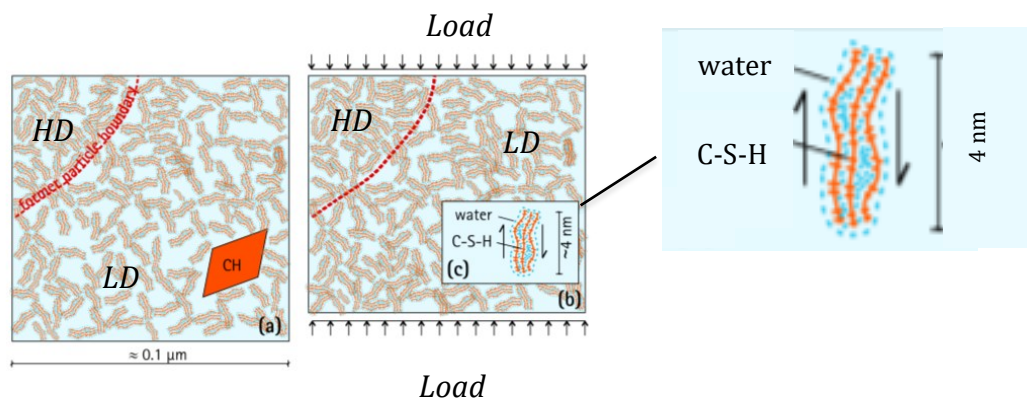
Figure 2.9 Sketch of the microstructure transformation of hardened cement paste during creep: HD- and LD-C-S-H phases in (a) the unloaded stage and (b) the loaded stage; (c) zoom area in (b) of a C-S-H layered nanoparticle. Captured from Haist et al. [114].

2.6.2   Molecular dynamic (MD) simulations of creep

The molecular structure of reaction products dictates the mechanical behaviour of the paste. However, it is extremely hard to test specimens at the molecular level experimentally. Molecular dynamics (MD) is one of the best tools available to numerically simulate and analyse the evolution of a nanostructure and used for modeling and investigation of time-dependent properties, like creep, at the molecular scale.

H. Manzano et al [115] and A. Morshedifard et al. [116] performed MD simulations of strain evolution of hydrated cement paste under shear stress. The simulation results reproduced the logarithmic creep response of cement paste. The authors attributed the strain of the C-S-H molecular structure to the sliding of C-S-H molecular layers and concluded that C-S-H particles themselves might be the cause of creep deformation.

A few publications on the molecular structure of C-A-S-H [117, 118] and N-A-S-H gel [119, 120] also presented the results of MD simulations. However, the authors primarily focused on creating realistic and accurate models of the molecular structure of AAM, and

do not address the time-dependent behaviour of the material. Studies on the nanoscale origin of creep in AAM are still missing.

2.7 Creep and shrinkage

2.7.1 Shrinkage strain

In practice creep deformations are almost always accompanied and influenced by shrinkage of the concrete. Shrinkage strains may come from self-desiccation of the concrete during hardening, known as autogenous shrinkage, or from moisture loss to the environment, i.e. drying shrinkage. Shrinkage of the paste will cause internal stresses in the concrete, maybe followed by microcracking. The shrinkage-induced stresses and microcracking will affect the stress-dependent creep strains of the concrete.

Shrinkage is the reduction in volume of the concrete due to the consumption or loss of water [121]. The shrinkage strain ε_{cs} can be described by an increasing function of time, reaching an upper limit with a gradually decreasing rate. The shrinkage evolution is directly related to the moisture content of the material. A typical drying shrinkage curve is shown in Figure 2.10.

Note that the shrinkage curve of Figure 2.10 indicates that further shrinkage ceases after a relatively short period. However, the duration of this period depends on the geometry of the concrete element. In the case of particularly thick concrete elements, drying shrinkage start slowly and can continue for years.
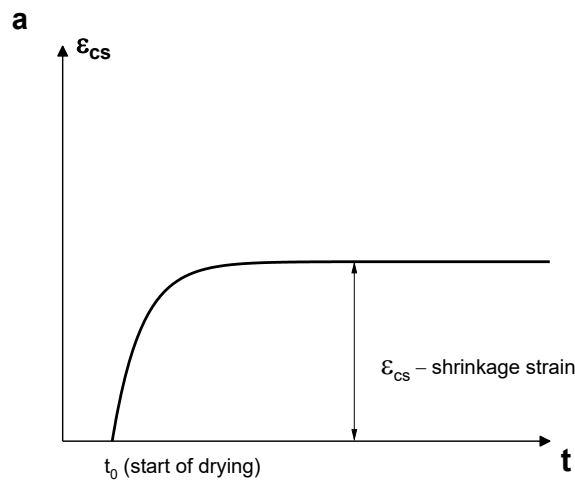
Figure 2.10 Typical shape of the evolution of shrinkage caused by drying. t_0 is the moment of the test initiation and ε_{cs} is the shrinkage strain.

Concrete exposed to moisture may exhibit less creep, while concrete that is subject to drying conditions will experience extra creep [122]. This additional creep is called *drying*

creep [10]. The intense drying and consequent high stress levels can cause a non-linear relationship between the load and the resulting strain function [73].

2.7.2   Shrinkage and shrinkage-induced phenomena in cement-based materials

As mentioned in the previous section shrinkage of cement-based materials may be caused by moisture loss to the environment (drying shrinkage) or hydration-induced self-desiccation. The latter type of shrinkage is known as *autogenous shrinkage*. Both types of shrinkage will result in internal stresses and eventually microcracking.

2.7.2.1 Autogenous shrinkage

During the first phase of the hydration process of cement-based materials so called *autogenous shrinkage* may occur. Autogenous shrinkage is caused by the self-desiccation process, which happens when the water in the concrete mix is consumed by the reaction and can continue for several weeks after the concrete has hardened. If the specimen is sealed it is the only type of shrinkage taking place [10]. For normal strength OPC concrete with high water-cement ratio (above 0.55) and no admixtures, autogenous shrinkage is usually negligibly small [10]. However, for high strength concretes with a very low water-cement ratio (0.4 or less) and various admixtures, as well as for AAC, autogenous shrinkage makes significant contribution to overall deformation [11].

Autogenous shrinkage can affect the creep behaviour of concrete in several ways. It causes the development of internal stresses within the concrete, which will cause creep of the material [11, 123]. Moreover, internal stresses may exceed the elastic limit and therefore cause nanocracks in the paste, which, subsequently, affect its mechanical properties impacting the creep behaviour of concrete.

2.7.2.2 Drying shrinkage and drying creep (Pickett effect)

Drying shrinkage often represents the substantial part of total shrinkage in concrete. While various factors can affect the shrinkage of concrete, numerous studies have shown that the main contribution to shrinkage comes from the concrete binder [121]. Coarse aggregates are generally considered to be non-shrinking. Drying shrinkage in ordinary Portland cement (OPC) concrete is caused by evaporation of water from the capillary pores. Evaporation occurs under ambient conditions with RH below 100%. This leads to an increase in capillary tension in the remaining pore water.

The drying creep, or Pickett effect, can be attributed to the coexistence of microcracking and stress-induced shrinkage. Due to the non-uniform distribution of moisture in a shrinkage specimen, the outer layer of the specimen dries out and contracts more and earlier than the inner layer, which remains wet and does not shrink. Consequently, during the initial stages of the drying process, the surface layer experiences tensile stress while the inner layer is under compression. This tensile stress may lead to the occurrence of localized microcracks in the surface layer, a phenomenon that has been extensively studied by various researchers [124-127]. As a result of the nonlinear and irreversible behaviour of concrete under tensile stress, the microcracks cannot fully close when the moisture distribution eventually approaches a uniform state. Consequently, the measured

shrinkage of the specimen is lowered by this effect. On the other hand, in the case of drying creep specimens, the cross-section of a concrete specimen is subjected to compression, thereby diminishing stress gradients and microcracking on planes perpendicular to the direction of compression. Consequently, the observed shrinkage of the specimen is less reduced by microcracking. This indicates that the drying creep must be greater than the combined values of the separately observed basic creep and shrinkage.

2.7.3 Shrinkage in alkali-activated systems

2.7.3.1 Shrinkage mechanisms and parameters

The list of the most important mechanisms governing the shrinkage of AAM is the same as for OPC concrete. These mechanisms can be divided into the following four types, i.e. capillary stress, which is referred to the evaporation of the liquid phase in capillary pores during drying to form a liquid–vapour meniscus; "surface tension" or "Gibbs-Bangham effect": the force's effect, which raises due to the diffusion of physically adsorbed water within the pore volume; disjoining pressure originating from the cohesion between the pore water and the pore wall surface; loss of interlayer water [56, 128].

The difference in shrinkage between AAC and OPC concrete has been attributed in recent publications to differences in the pore structure and reaction products of the pastes. The significantly higher shrinkage in alkali-activated systems was primarily attributed to the absence of certain crystal phases in the hydration products and the high ratio of mesopores in the pastes [11, 28, 32, 128].

2.7.3.2 Autogenous shrinkage of AAC

Collins and Sanjayan [129] attributed the significant autogenous shrinkage of alkali-activated slag (AAS) paste to its finer pore structure. Their experiments showed that when Na_2SiO_3 activated the AAS paste, approximately 80% of the pores were mesopores (1.25–25 nm), while ordinary Portland cement (OPC) paste contained only about 36% mesopores and a higher percentage of macropores (25–5000 nm). The fine pore structure of AAS resulted in a small radius of meniscus in the paste [130], causing high pore pressure. The presence of a substantial volume of mesopores in AAS was also confirmed by Lee et al. [131]. Additionally, Ballekere Kumarappa et al. [132] reported that AAS exhibited higher surface tension compared to OPC due to the abundance of ions, leading to increased pore pressure. Ye and Radlińska [133] proposed that the collapse and redistribution of the aluminium-modified calcium silicate hydrate (C-A-S-H) gel, caused by the incorporation of alkali cations, contributed to the high shrinkage of AAS, exhibiting visco-elastic and visco-plastic behaviour at the macroscopic scale.

Some authors suggested that, beyond self-desiccation, the higher value of autogenous shrinkage in AAS compared to high-strength OPC concrete could also be linked to the silica polymerization reaction during the formation of C-A-S-H gels (Uppalapati and Cizer [134], Ma and Dehn [135]). Nonetheless, references [117, 136] indicate that the degree of Si polymerization in C-A-S-H is largely in the Q2 form, akin to Si in C-S-H. Consequently, the hypothesis rooted in silica polymerization appears inadequate in explaining the significantly higher autogenous shrinkage observed in AAM compared to OPC.

2.7.4 Creep in alkali-activated concrete

As it was already mentioned, there is very limited research reported and explained for the creep phenomenon in AAC. However, over the last three decades, several studies have been conducted on the creep behaviour of AAC considering multiple influencing factors [18, 133, 135, 139, 245-249]. The investigations involved different material compositions [18, 135, 245, 246-248], curing [139, 248] and loading conditions [135, 249] and differences of creep mechanism in conventional concrete and slag-based concrete [18, 133, 162].

2.7.4.1 Raw materials and activator

The broad availability of raw materials for AAC presents both advantages and disadvantages. Variations in properties among the raw materials from different sources make accurately assessing the creep of related concrete mixtures challenging, allowing only a general analysis.

Collins and Sanjayan [245] investigated the creep characteristics of alkali-activated slag-based concrete. Their findings indicated that AAC exhibited a higher creep strain compared to OPC concrete. They also observed that the creep development of slag-based AAC and fly ash-based AAC was similar, with slow growth in the early stage and accelerated growth later on (see Figure 2.11).
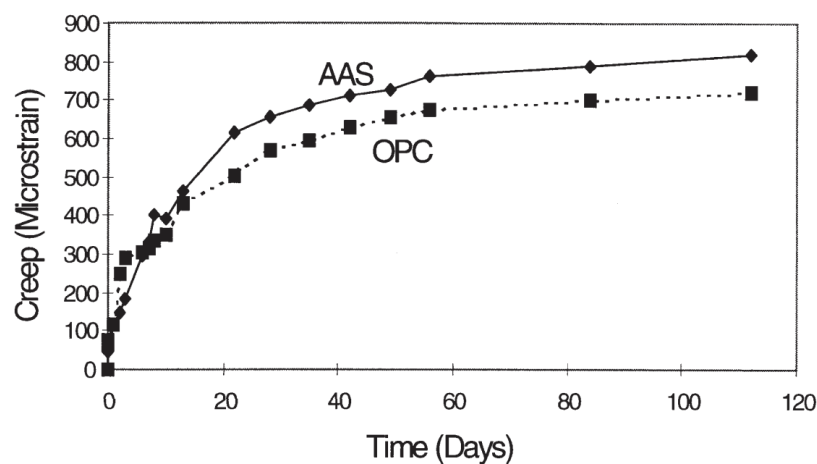
Figure 2.11 Overall strain due to creep following 112 days loading of slag-based AAC (AAS) and OPC concrete. Captured from [245].

Ma and Dehn [135] observed the creep of sealed and unsealed slag-based AAC cylinders under sustained loads with varying stress ratios. They found that the creep coefficients of AAS for both types of samples (sealed and unsealed) were greater than those of conventional OPC concrete with equivalent compressive strength (see Figure 2.14).

Un [18] investigated the creep characteristics of an AAC containing 5% fly ash and 95% slag. The findings distinctly demonstrate the differing creep behaviours between AAC and OPC concrete (see Figure 2.12). The creep progression of the OPC concrete sample

exhibited rapid development in the initial phase, followed by a tendency towards stability in the later stages with minimal creep increment. While the early-stage creep in AAC specimens was lower than in OPC concrete, the rate of creep in later-stage AAC did not decline rapidly, and the creep tendency in AAC continued to increase even after one year of loading.
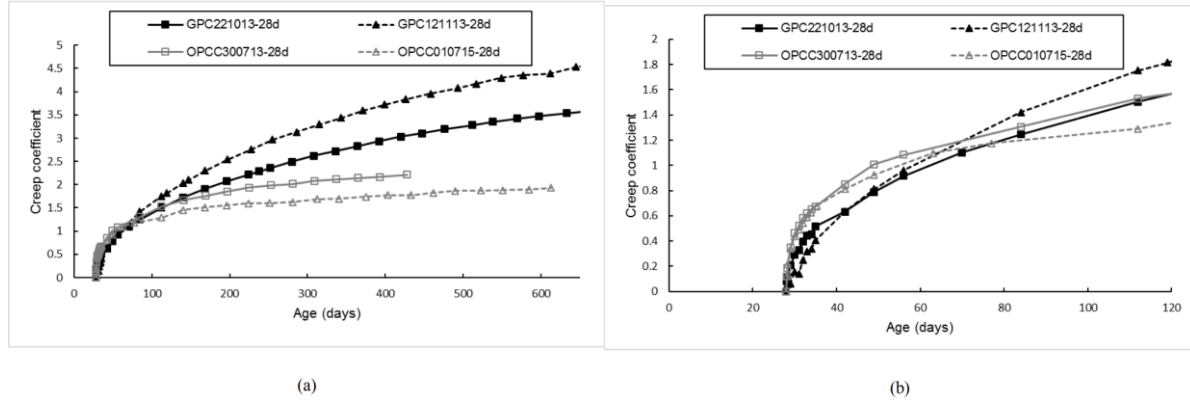
Figure 2.12 Creep coefficient of AAC and OPC concrete: (a) up to age of 500 days, (b) in first three months of loading. Captured from [18].

Islam et al. [246] investigated the impact of activator dosage on the creep of low calcium fly ash-based AAC. By altering the mass ratio of activator and fly ash while keeping the activator modulus and other material quantities constant, their findings indicate that as the quantity of alkali activator rises, the compressive strength and elastic modulus of the sample at the age of loading initiation. Utilizing an excess of alkali activator can be likened to introducing surplus water into the matrix, elevating the water-binder ratio of the entire system. This leads to a reduction in compressive strength and elastic modulus of the sample, as well as an increase in creep. Concurrently, Islam explored the correlation between specimen creep and compressive strength. The specimen's creep diminishes with higher compressive strength, aligning with the observations made by Gunasekera et al. [247] and Wallah et al. [248].

2.7.4.2 Curing and loading conditions

Concrete creep has been observed to rely on various external factors, such as curing conditions and the level of loading. Multiple studies have indicated that curing conditions greatly affect the creep characteristics of alkali activated cementitious materials.

Castel [139] comprehensively studied the effect of curing temperature and humidity on the creep of fly ash and slag-based AAC (85.2% fly ash and 14.8% slag). The batch of specimens was sealed and stored at 40 ℃ in an oven for 3 days and then stored in a controlled room at 23 ℃ and 60 % RH. The second batch was sealed and stored at 40 ℃ in an oven for 1 day and then cured in 80 ℃ water bath for further 7 days. After curing the specimens during the 90-day loading period (see Figure 2.13). The loading conditions did not allow to compare the creep test results quantitatively. However the results indicated that after 90 days of loading the total and creep strain of the first type specimens
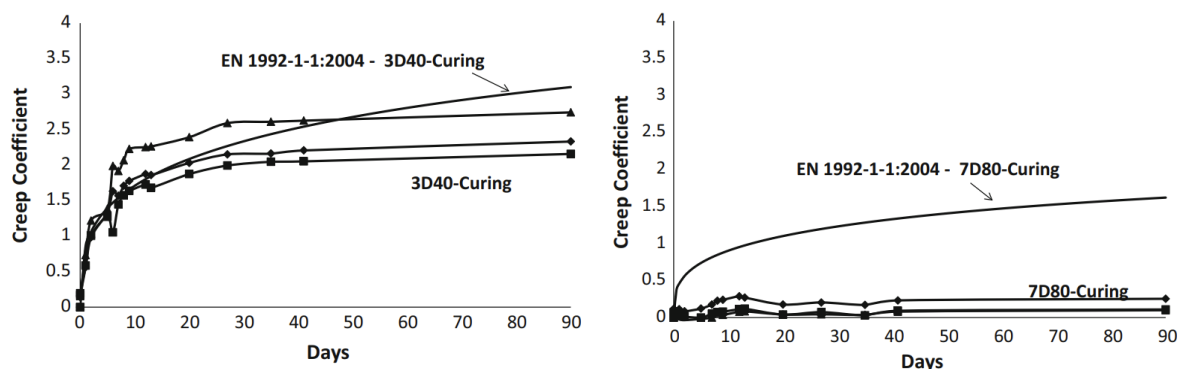
Figure 2.13 Creep coefficients experimentally measured and predicted by model of EN 1992-1-1:2004. Captured from [139].

was much higher than that of the second type of specimens. This follows the observation that the higher the compressive strength leads to the smaller the creep.

Wallah [248] studied the creep properties of fly ash-based AAC under two curing conditions: dry and steam. His findings indicate that after 7 days of curing, the compressive strength of the specimens subjected to steam curing is approximately 15% weaker than those in dry curing, while the elastic modulus is roughly 8% lower compared to the dry-cured specimens. Then the specimens underwent loading for a duration of one year. The specific creep value of fly ash-based AAC, following one year of loading, displayed an inverse relationship with compressive strength. Higher compressive strength correlated with lower specific creep values, affirming the previously mentioned conclusion. The outcomes highlight that the application of steam curing diminishes concrete strength and augments the creep factor. However, a more detailed investigation and explanation of this phenomenon are necessary.

The study of Zhou et al. [249] focused on the comparison of creep of slag-based AAC under a stress–strength ratios from 0.15 up to 0.75. Within this range, the creep of AAC concrete displays a convergent nonlinear phase and a non-convergent phase, but lacks a distinct linear phase. This observed phenomenon is believed to differ from that observed in OPC concrete, which exhibits a linear creep phase typically occurring at a stress–strength ratio of 0.4. The transition points between the convergent nonlinear creep and non-convergent creep of slag-based AAC lie above 0.6 and around 0.75, similar to those observed in OPC concrete. AAC generally maintains a consistent creep coefficient within the stress–strength ratio range of 0.15–0.6, offering a straightforward method for predicting creep. Ma and Dehn [135] also delved into AAC creep under different stress–strength ratios (0.35 and 0.5) and varying relative humidity conditions (65% and sealed) for approximately 180 days (see Figure 2.14). They compared their test outcomes with the results from the creep model of CEB-FIP 2010 [140, 141] and noted that the experimentally determined creep coefficient of AAC is higher than what the related model predicts.
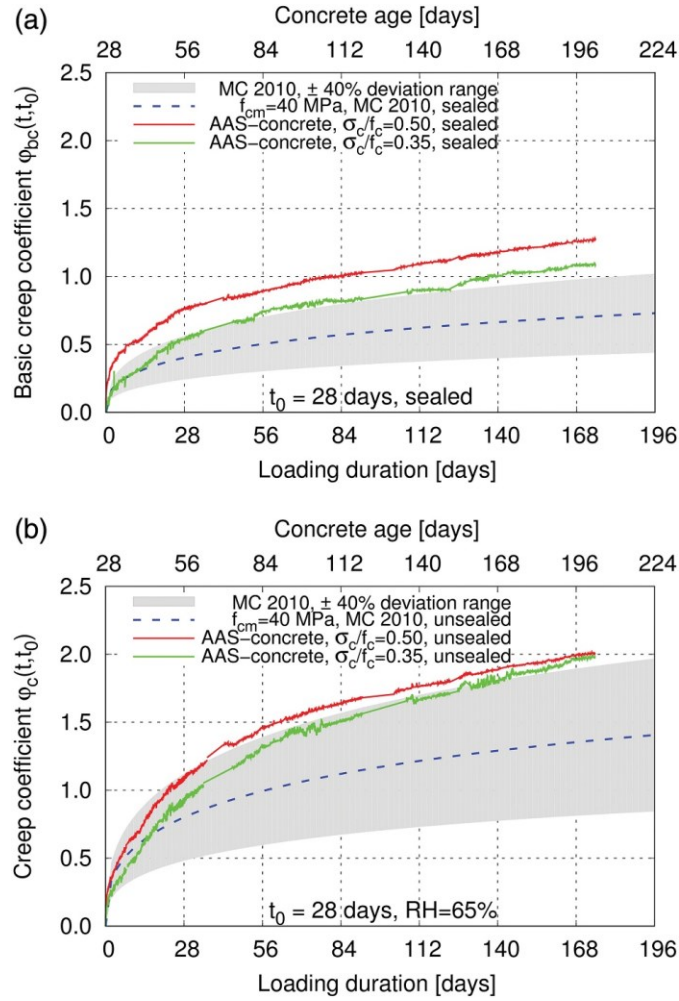
Figure 2.14 Creep coefficient of sealed (a) and unsealed (b) slag-based AAC. Captured from [135].

2.7.4.3 Creep mechanisms in AAC

The primary creep mechanisms observed in OPC concrete are likely to be present in AAC as well. However, the distinct microstructure and mechanical properties of AAC suggest particular aspects in the physics of creep. In a study by Un [18], it was noted that prolonged loading on alkali-activated binders results in increased phase slippage and alters the microstructure towards denser phases, leading to amplified creep deformation. Additionally, significant drying creep is induced by the movement of water within the pore network. Moreover, AAC exhibits higher sensitivity to changes in temperature compared to OPC, owing to its increased visco-flow behaviour and additional polymerization at elevated temperatures, as previously mentioned.

According to [133], the noticeable viscous deformation observed in slag-based AAC origins from the rearrangement of C-A-S-H gel microstructure. The higher viscoelasticity of C-A-S-H gel, compared to C-S-H gel, is attributed to the structural integration of alkali cations in C-A-S-H. This integration reduces the orderly arrangement of C-A-S-H layers, interpreting the gel more susceptible to break and rearrangement [133].

The significant creep in slag-based AAC systems also contributes substantially to their shrinkage, involving both elastic and non-elastic deformations [162] (see Figure 2.15). Li et al. [162] using experimentally determined Relative Humidity (RH), elastic modulus, and saturation degree as parameters, calculated the elastic deformation of alkali-activated slag-based paste under capillary pressure. Their findings suggested that this constituted less than 25% of the total autogenous shrinkage. The author also conducted computational simulations to validate their understanding of the creep mechanism in slag-based AAC. Li et al. [162] employed an empirical equation to estimate the creep coefficient based on Degree of Reaction (DoR) and water/binder ratio, aggregating the increments of creep formed during each time interval. This approach yielded accurate forecasts of autogenous shrinkage in alkali-activated slag-based pastes, suggesting that this model effectively captures the genuine creep mechanism occurring within these systems.
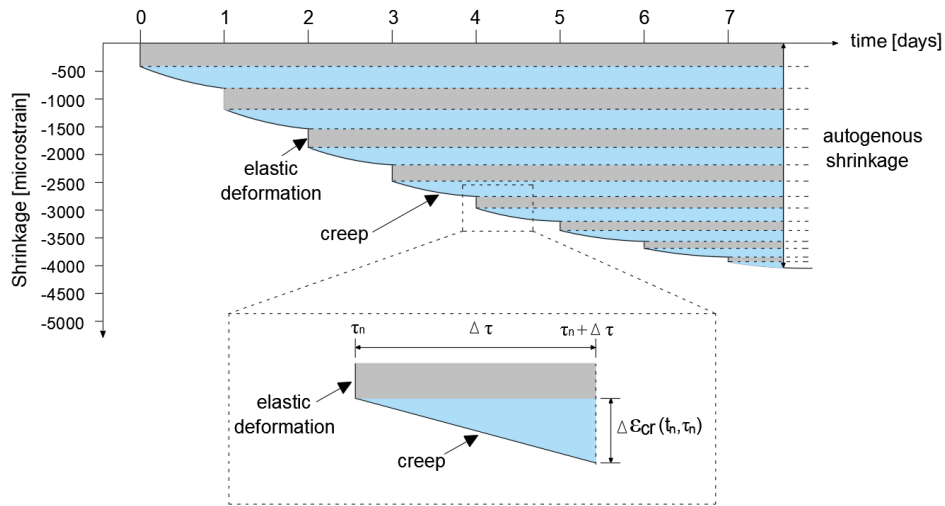
Figure 2.15 Schematic representation of the model used in [162] to simulate the creep compliance of AAS paste. Captured from [162].

To conclude, over the last three decades, many experimental studies have explored the creep behaviour of AAC, taking into account various influencing factors such as material compositions, curing conditions and loading level. Due to the distinct nano- and microstructures of AAC compared to OPC concrete, the creep behaviour in AAC differs from that in OPC, however, the particular origin of the difference remains unexplored. Considering the current outcomes of the research, more research on creep of AAC for multiple scales is needed.

2.8   Code-type creep models

The complexity of creep mechanisms in concrete and the large number of parameters that affect the evolution of creep make it difficult to predict the overall time-dependent behaviour of concrete. However, code-based models have been developed to provide

guidance for general design purposes. These models do not explicitly describe creep mechanisms, but instead are calibrated based on the specific concrete strength class and other key parameters. In this section, two code-type models are presented, namely EuroCode 2 [8] and fib Model Code 2010 [137].

2.8.1 EuroCode 2

EuroCode 2 (EC2) (EN 1995-1-1) gives formulas for estimating creep evolution. These formulas can be used when high accuracy in the estimation of time-dependent deformations is not required. The EC2 standard [8] presents basic equations for determining creep coefficient evolution over time based on creep strain data for different strength classes of concrete, different humidity, nominal dimensions of concrete elements and types of cements. The creep coefficient $\varphi(t,t')$ is calculated by multiplying the notional creep coefficient, φ_0, with a factor that describes the development of creep with time, $\beta_c(t,t')$:

$$\varphi(t,t') = \varphi_0 \beta_c(t,t') \tag{2.6}$$

with

$$\varphi_0 = \varphi_{RH} \beta(f_{cm}) \beta(t') \tag{2.7}$$

and

$$\beta_c(t,t') = ((t - t')/(\beta_{RH} + t - t'))^{0.3} \tag{2.8}$$

where φ_{RH} is the factor for the effect of relative humidity, $\beta(f_{cm})$ is the factor based on the compressive strength of concrete, f_{cm}, $\beta(t')$ is the factor for the age of concrete at time of loading and β_{RH} is the factor depending on the relative humidity.

Direct comparison of EC2 for creep and shrinkage in OPC concrete and AAC is hard because of the large number of input parameters (ambient humidity, the dimensions of the element, the composition of the concrete, the maturity of the concrete when the load is first applied, and the duration and magnitude of the loading). However, estimations of parameter values for typical concrete mixtures are presented in several studies [138, 139]. For instance, Castel et al. [139] studied the time-dependent strains of an AAC mixture cured at 40 °C and at 80 °C with a binder composed of 85.2 % low calcium FA and 14.8 % BFS. The experimental results were compared to predictions made using EC2, Eq. (2.6)-(2.8). Creep strains were similar or less than those predicted by EC2 for OPC concrete when the AAC was cured for 3 days at 40 °C. However, creep strains of the specimens cured at 80 °C during 7 days were almost negligible.

Negahban et al. [137] published a one-year study of restrained shrinkage and creep behaviours of ambient temperature-cured OPC and slag/fly ash AAC. An assessment of

the suitability of existing prediction models, including EC2 and Model Code 2010, by the authors showed that the existing models under/overestimated the short- and long-term creep coefficient. Based on the findings, the creep development of OPC concrete slowed down after 4 months, while AAC did not show similar behaviour.

2.8.2 Model Code 2010

The fib Model Code 2010 (MC2010) treats the creep coefficient, $\varphi(t,t')$, as a sum of two components: $\varphi_{bc}(t,t')$ for the basic creep coefficient and $\varphi_{dc}(t,t')$ for the drying creep coefficient. The MC2010 also uses compressive strength as an input parameter. The detailed explanation of the model can be found in [140, 141]. Briefly, the components are calculated as follows:

$$\varphi(t, t') = \varphi_{bc}(t,t') + \varphi_{dc}(t,t') \tag{2.9}$$

with

$$\varphi_{bc}(t, t') = \beta_{bc}(f_{cm}) \cdot \beta_{bc}(t,t') \tag{2.10}$$

and

$$\varphi_{dc}(t, t') = \varphi_{dc}(f_{cm}) \cdot \beta(RH) \cdot \beta(t') \cdot \beta_{dc}(t,t') \tag{2.11}$$

where factors $\beta_{bc}(f_{cm})$ and $\beta_{dc}(f_{cm})$ are functions of the compressive strength of concrete at an age of 28 days, $\beta_{bc}(t,t')$ and $\beta_{dc}(t,t')$ are time-dependent factors, $\beta(RH)$ is a factor related to the relative humidity and size of concrete element and $\beta(t')$ is a factor for the age of loading.

The MC2010 was initially developed for describing the behaviour of OPC concrete. Du et al. [142] made a study on creep of a column made of AAC and made a comparison of the creep strain and the approximation according MC2010. The authors found that MC2010 overestimates the creep deformations of the column made of AAC. They concluded that the inability of MC2010 to predict the creep of AAC elements is most likely due to the different reaction process and microstructure of alkali activated paste compared to cement paste.

2.9 Discussion

The use of AAC as a building material requires reliable predictions of long-term mechanical properties, such as creep and relaxation. This is crucial for ensuring the required levels of serviceability and durability of structures made of AAC. In other words, the ability of AAC to withstand long-term sustained loads and resist prestress losses in concrete members has to be known. However, current findings on the creep behaviour of

AAC still have some gaps that need to be addressed.

From the literature survey on creep of AAC we learn that two main questions have to be addressed:

1. What is the magnitude of creep in AAC, and how do internal and external factors, such as binder mixture design and curing conditions, affect the evolution of creep in AAC?

2. What is the mechanism of creep in AAC, and how does the specific microstructure of alkali-activated binders, including porosity and pore geometry, nanoscale mechanical properties, and molecular bonding of reaction products, influence the differences between creep evolutions in AAC and in OPC concrete?

While existing literature provides some relationships between creep values of AAC and the main influencing factors, experimental research on this topic is rather scattered and a comprehensive explanation of creep behaviour of AAC is still lacking. To gain a better understanding of creep behaviour in AAC, tests of characteristic mechanical properties, including creep and shrinkage, should be conducted.

The research on creep mechanisms in AAC is limited due to the complexity of conducting experiments on paste at small scales. Analysing creep mechanisms in AAC in relation to the microstructure and nanoscale properties of alkali-activated pastes can help to identify similarities and differences between the creep mechanisms observed in OPC concrete and AAC.

Finally, while the code-type models can reproduce the general trend of creep deformations of elements and structures made of OPC-based materials, they fail to do so for structures and elements in AAC-based concrete.

2.10 Concluding remarks

This chapter provides a literature survey on the current findings related to concrete creep. It starts with a brief overview of AAM suitable for construction, followed by a discussion of the mechanical properties of AAC, and a description of the main creep theories. Finally, the chapter describes engineering models for predicting long-term concrete creep.

The survey indicates that a significant amount of data has been accumulated over the past few decades about mechanical properties of AAM, but little is known about creep. AAM's show many similarities with cementitious materials in terms of microstructure and short-term mechanical properties. As said, however, there is a relatively low number of reported studies on long-term mechanical properties and creep tests of AAC, and a deep understanding of the microstructure evolution and multi-scale physics of creep mechanisms in AAC has not yet been reached. Currently used formula for predicting long-term creep deformations of AAM-based elements overestimate or underestimate the actual creep strain, indicating a lack of knowledge about the important governing parameters.

Based on the presented review the following concluding remarks can be made:

1. Creep of concrete is affected by a range of extrinsic and intrinsic factors, including mixture design and curing conditions. The correlations between external parameters, mechanical properties, and creep evolution in AAC are not yet clearly defined. Consequently, it is necessary to conduct creep tests and mechanical properties tests, such as compressive strength, elastic modulus and splitting tensile strength, to investigate and understand these relationships.

2. Many similarities between the microstructure of AAM and cement paste suggest that the creep mechanisms proposed for OPC concrete may also be applicable for AAC. However, the specific chemical composition and pore structure of AAM, as well as its effect on the macroscale mechanical properties, should be considered to provide a complete description of creep mechanisms in AAC. Further multiscale research on mechanical properties and creep is needed to take another step towards a better understanding and complete description of multiscale physics of creep behaviour.

3. A reliable engineering creep prediction model for AAC is not yet available. The existing models for OPC concretes, i.e. EuroCode 2 and ModelCode 2010, do not correctly predict the creep of AAC. The correlation between creep and mechanical properties, as assumed for OPC concrete, should be adjusted for AAC. A modified model should be developed based on the results of creep tests on AAC.

Chapter 3

Mechanical properties of alkali-activated concrete

3.1 Introduction

As discussed in Chapter 2, it appears to be possible to correlate the creep of OPC-based concrete with its mechanical properties, such as compressive strength, splitting tensile strength and elastic modulus. It is assumed that this could also be the case for AAC-based concrete. For this reason, the investigation of concrete creep starts with an evaluation of the mechanical properties of alkali-activated concrete (AAC). Moreover, knowledge of the mechanical properties is necessary for conducting standard creep tests [143]: the compressive strength must be known to ensure that the sustained load during the creep test stays within a pre-defined range. To ensure a linear relationship between applied stress and creep strain, the stress should not exceed 40% of the compressive strength [10]. Besides the compressive strength the modulus of elasticity is needed for calculating the initial elastic strain, which is required for subsequent estimation of the creep coefficient and creep compliance functions. The tensile splitting strength is used to judge whether cracking is likely to occur or not.

The mechanical properties of alkali-activated concrete (AAC) greatly depend on the properties of the prime materials (precursors and activators) and the curing conditions [27, 48]. The precursor ratio (i.e. slag/fly ash ratio) and curing conditions affect the resulting material microstructure, changes in the state of water, including drying shrinkage and possible formation of microcracks. The long-term mechanical properties of concrete specimens are also influenced by the storage conditions. For industrial

ordinary Portland cement[1] (OPC) based concrete systems the development of mechanical properties, including the effect of curing conditions, are well-investigated [122, 144]. For AAC systems, however, such information is still scarce [145].

This chapter deals with the evolution of the compressive strength, splitting tensile strength and elastic modulus of AAC mixtures and discusses the influence of the precursor ratio, curing and storage conditions on this evolution. For the concrete mixtures blast furnace slag and fly ash, blended in different proportions, are used as precursors [146]. Tests were performed according to standard recommendations for testing OPC concrete [14]. For comparison also PC-based concrete mixtures will be considered. Finally, the results were evaluated qualitatively and quantitatively.

3.2   Materials and methods

3.2.1   Raw materials and mixture design

3.2.1.1   Precursors

Blast furnace slag (BFS) from Ecocem Benelux BV, and fly ash (FA) from Vliegasunie BV were used in this study as precursors. The chemical compositions of BFS and FA were determined by X-ray fluorescence (XRF) and shown in Table 3.1.

The hydraulic activity of BFS can be identified by the extended basicity coefficient (K_b = $(CaO+MgO)/(SiO_2)$) [147]. European Standard EN 197-1 [148] requires $K_b>1$. In general, glassy BFS with $0.5<CaO/SiO_2<2$ and $0.1<Al_2O_3/SiO_2<0.6$ is considered as suitable for alkali-activation [149, 150]. The BFS used in this research showed $K_b=1.6$, $CaO/SiO_2=1.3$ and $Al_2O/SiO_2=0.4$.

Table 3.1. XRF-test results for used raw materials, viz. slag and fly ash.

Oxide	SiO_2	Al_2O_3	CaO	MgO	Fe_2O_3	SO_3	K_2O	TiO_2	Other	LOI
					Weight [%]					
Slag	31.77	13.25	40.50	9.27	0.52 1	1.49	0.34	0.97	0.21	1.3
Fly ash	56.8	23.8	4.8	1.5	7.2	0.3	1.6	1.2	1.6	1.2

LOI = Loss on ignition.

The FA used in this research was low calcium fly ash, categorized as Class F according to the ASTM C618[151].

---

[1] In the most recent publications and latest standards the term ordinary Portland cement (OPC) was replaced with the term Portland cement (PC).

The mineralogical compositions of BFS and FA were studied with X-ray diffraction (XRD). The XRD results (see Figure 3.1) for BFS exhibit a broad hump around 31° 2-theta without pronounced peaks, indicating dominant microcrystalline and amorphous phases. The XRD pattern of FA revealed the presence of more mineralogical phases, namely quartz (Q) (SiO_2), mullite (M) ($3(Al_2O_3) \cdot 2(SiO_2)$) and hematite (Hm) ($\alpha$-$Fe_2O_3$). Analysis using the Rietveld method determined the amorphous content of FA to be 71%. By subtracting the crystalline phases of SiO_2 and Al_2O_3 from their total amounts, the reactive SiO_2 and Al_2O_3 were determined at 37% and 15%, respectively [152].
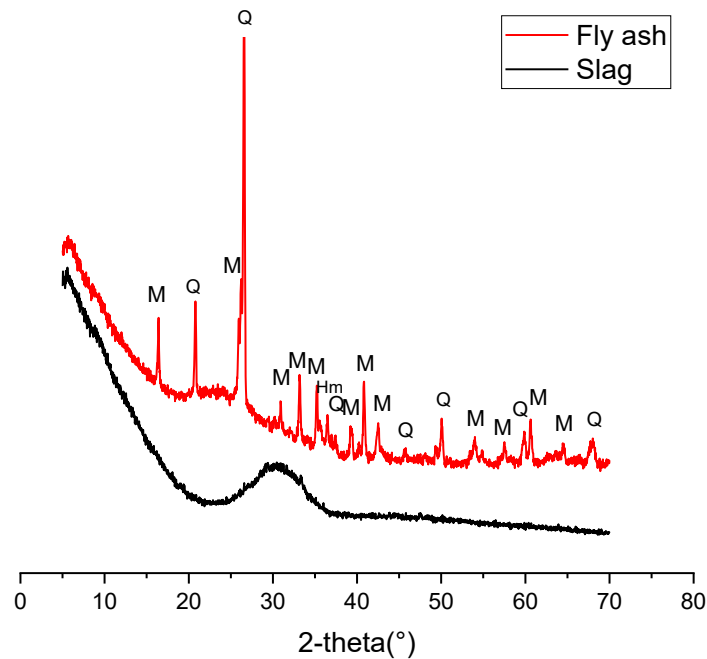
Figure 3.1 XRD results of BFS and the FA. The crystalline phases are marked as quartz (Q) (SiO_2), mullite (M) ($3(Al_2O_3) 2(SiO_2)$) and hematite (Hm) (Fe_2O_3).

Figure 3.2 shows the particle size distribution curves of BFS and FA, measured with EyeTech Laser diffraction analyser, Ankersmid. The d_{50} is the particle size in microns that divides the distribution with half above and half below this diameter. The particle size of BFS used in this research ranges from 0.1 to 50 μm, with a d_{50} equal to 18.3 μm. The particle size of the FA is between 0.14 and 138 μm, with a d_{50} of 48.1 μm.

Because of their low specific surface area, coarse powders appear to react more slowly than fine powders. Powders with particles larger than 20 μm show only little activity, whereas powders with many particles smaller than 2 μm react completely within 24 h because of the large specific surface of these small particles [153].

49
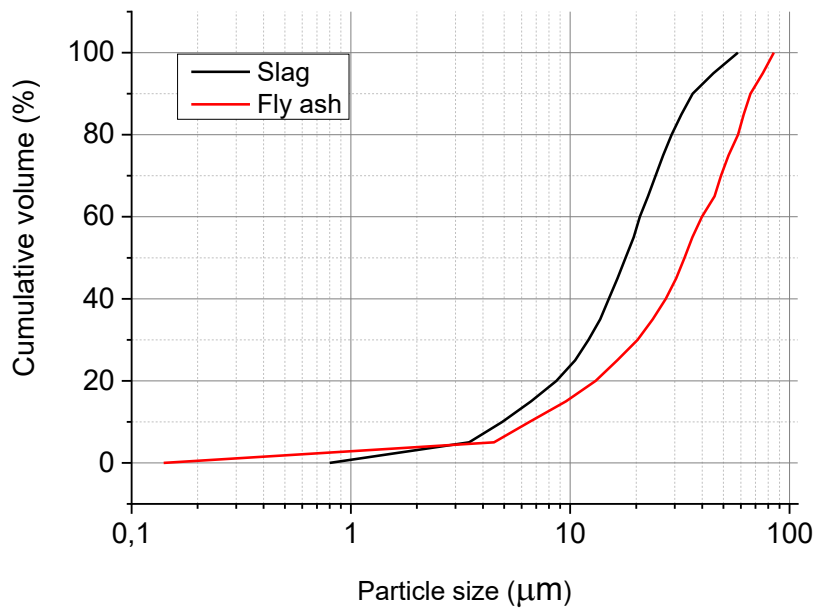
Figure 3.2 Particle size distributions of GGBFS and FA measured with laser diffraction analyser.

3.2.1.2 Alkali activator

The alkali activator was synthesized by mixing a NaOH solution and a sodium silicate (Na_2SiO_3) solution in 1:1 weight proportion. NaOH solution was prepared by mixing dry pellets of sodium hydroxide with distillate water to obtain a concentration of 4 moles per litre. The solution was then left at room temperature for 12 hours until it cooled down and the pellets dissolved completely. Sodium silicate solution from Brenntag was used in the ready-made form. The chemical composition of sodium silicate solution was: 27.5 wt. % SiO_2, 8.25 wt.% Na_2O, 64.25 wt.% H_2O.

3.2.1.3 Mixture design

The detailed mixture design of the AAC mixtures is given in Table 3.2. Three mixtures were investigated in this study: S100, S70 and S50. S100 is the BFS-based concrete. This S100 mixture showed high early-age strength, but short setting time and, in fact, insufficient workability [146]. To delay the setting time and strength development process, FA-blending was used. Blended BFS/FA mixtures, with the ratios 70:30 and 50:50 wt.%, were named S70 and S50, respectively. The sole alkali-activated FA mixture was not included in the research plan due to its low chemical reaction rate and, therefore, its relatively long setting time at ambient temperature [65]. For example, an initial setting time of 14 hours was reported for the alkali-activated FA paste with liquid-to-binder ratio (l/b)=0.5 [15]. To investigate the effect of the precursors' ratio, other influencing parameters were kept constant: the total amount of binder for all three mixtures was fixed on the same level - 400 kg/m³, and liquid/binder (l/b) ratio was equal 0.5.

Table 3.2. Mixture design of AAC .

Component	S100 [kg/m³]	S70 [kg/m³]	S50 [kg/m³]
Slag	400	280	200
Fly ash	0	120	200
Activator	200	200	200
Liquid/binder (l/b) ratio	0.5	0.5	0.5
Aggregate (0–4 mm)	789	789	789
Aggregate (4–8 mm)	440	440	440
Aggregate (8–16 mm)	525	525	525

The alkalinity (pH) of the activator was 14.4, measured with the 827 Metrohm pH meter [15]. The content of Na_2O and modulus of activator significantly affect the strength development, as it was discussed in Chapter 2. Optimal values of the alkali modulus (SiO_2/Na_2O mole ratio) of the activator are in the range of 0.75–1.5 [154]. The alkali modulus of the activation solution in this study was 1.5. More details about the choice of the activator can be found in the work [15].

Cement-based concrete C65, made with CEM I and CEM III, was chosen as a reference. This reference concrete had a similar strength as selected AAC mixtures and rapid strength gain. The mixture design of C65 is given in Table 3.3. Total amount of cement was 480 kg/m³. Note, that the volume ratio of paste to aggregate is 20% higher that of the AAC mixtures. However, assessing mixtures based on their compressive strength is more relevant. This is primarily due to the fact that the industrial models such as EC2 utilize compressive strength rather than l/b ratio or amount of binder as an input parameter.

Table 3.3. Mixture design of cement-based concrete C65.

Component	Mass [kg/m³]
CEM III	260
CEM I	220
Water *	183
Aggregate (0–4 mm)	772
Aggregate (4–8 mm)	882
Admixture	4.08

*) w/c ratio 0.381

3.2.2 Specimen preparation and curing conditions

Concrete prisms ($100 \times 100 \times 400$ mm³) for elastic modulus tests and cubes ($150 \times 150 \times 150$ mm³) for compressive and splitting tensile strength tests were cast in steel moulds.

Right after casting the specimen were covered with plastic films to prevent water evaporation and hardened at room temperature of approximately 20 °C for 24 hours. Then the specimens were demoulded and transferred to curing conditions.

3.2.2.1 Curing until 28 days

The specimens were moved into special conditions for curing: either sealed or moist until the age of 28 days. One batch of the samples was sealed with plastic film and stored at a temperature of 20±2 °C (denoted as sealed curing; see Figure 3.3). Another batch of specimens was kept in the fog room, where the relative humidity (RH) is 100% and temperature is also 20±2 °C (denoted as Fog room (moist) curing in Figure 3.3).

3.2.2.2 Storage after curing

After 28 days of curing, some specimens remain stored at the same conditions, some samples were unsealed or moved from the fog room, to be stored in a room with relative humidity of 55±5% and a temperature of 20±2 °C for testing the mechanical properties (indicated as RH 55% in Figure 3.3). The mechanical properties were determined at 28 days, 90 days, 180 days and 365 days. The curing regimes, storage conditions and timeline are shown schematically in Figure 3.3.
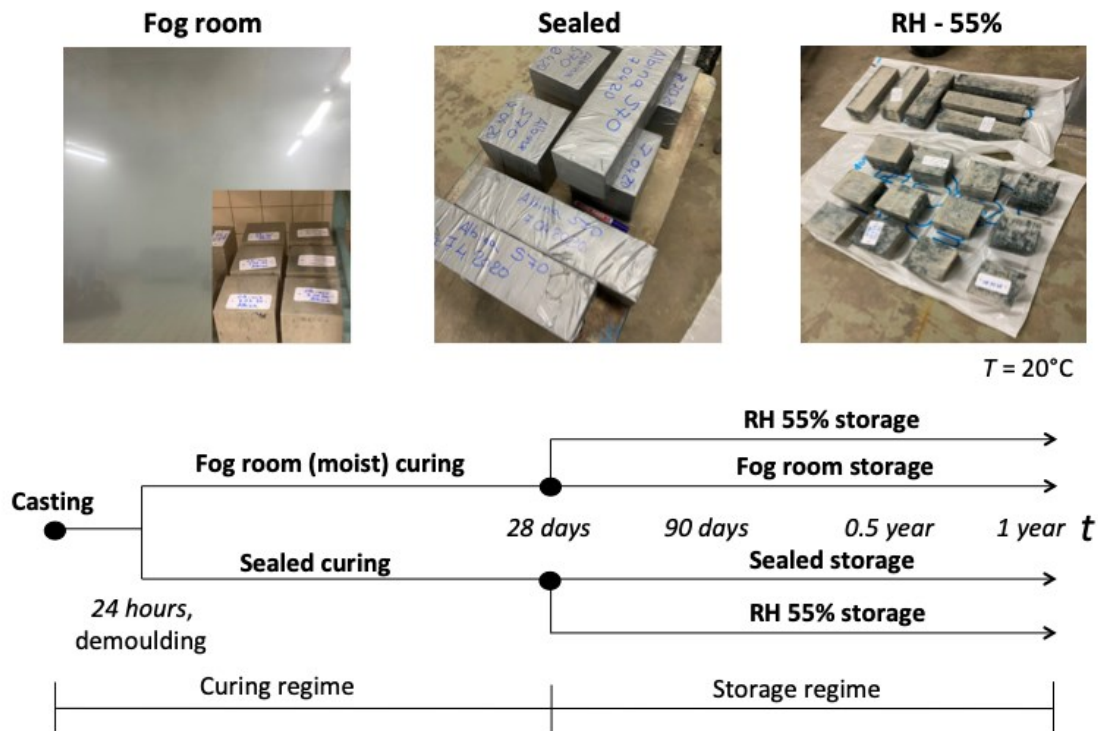
Figure 3.3 Curing regimes, storage conditions and the timeline of tests. Photos of the specimens show the real curing or storage conditions.

3.2.3   Test methods

3.2.3.1 Compressive and splitting tensile strength

The compressive and splitting tensile strength were tested on concrete cubes (150 ×150 × 150 mm^3) according to the standard recommendations NEN-EN 12390-3 and NEN-EN 12390-6 [155], respectively. The loading rate for the compressive strength test was 13.5 kN/s, and for the splitting tensile strength test 1.1 kN/s. The strength of the concrete at a specific age was determined by calculating the average value from three samples.

3.2.3.2 E-modulus

The elastic modulus of the concrete was tested according to ASTM C469 [156] by Tonibank hydraulic Instron. The strain evolution was measured by linear variable differential transducers (LVDTs) aligned vertically on the four sides of the concrete prism (100 × 100 × 400 mm^3) (Figure 3.4). The elastic modulus of each sample was determined from the stress-strain curve obtained after three loading-unloading cycles. The load varied from 10% to 30% of the compressive strength of the concrete. The loading rate was 1.1 kN/s.

Figure 3.4 Elastic modulus test. The changes of the specimen dimensions during the loading process were measured precisely. For this purpose the linear variable differential transducers (LVDTs) were aligned vertically on the four sides of the concrete prism.

3.3   Results and discussion

3.3.1   Compressive strength

3.3.1.1 Compressive strength of moist and sealed cured concrete

The evolution of compressive strength of the samples cured and stored under either moist or sealed conditions up to 1 year after casting is shown in Figure 3.5. For all the mixtures it holds that sealed curing resulted in a higher compressive strength than moist curing. Obviously AAC concrete does not behave differently from OPC-concrete: many researchers have also confirmed that moist-cured (wet) concrete exhibits lower strength than sealed-cured (normal) concrete[157-159]. Hordijk [158] and Ross [159] offered a possible explanation based on the Munich Model proposed by Wittmann [160, 161]. According to Wittmann's theory, the presence of water in the small pores of saturated concrete increases the distances between the CSH-molecules, thereby reducing the internal Van-der-Waals forces responsible for the structural integrity. Consequently, a lower force is required to fracture the structure, resulting in reduced static strength.

Noteworthy is the slight decrease of the strength of S100 mixture in the particular time range: between 90 days and 180 days for moistly cured specimens, and from 180 days and 365 days for sealed cured specimens. The possible reason for this may be the higher amount of microcracks [60] induced by autogenous shrinkage, which are not visible to the naked eye. Note, that this effect is related to the specimen properties, but not to the material itself.

(a) moist curing (fog room)   *(b)* sealed conditions
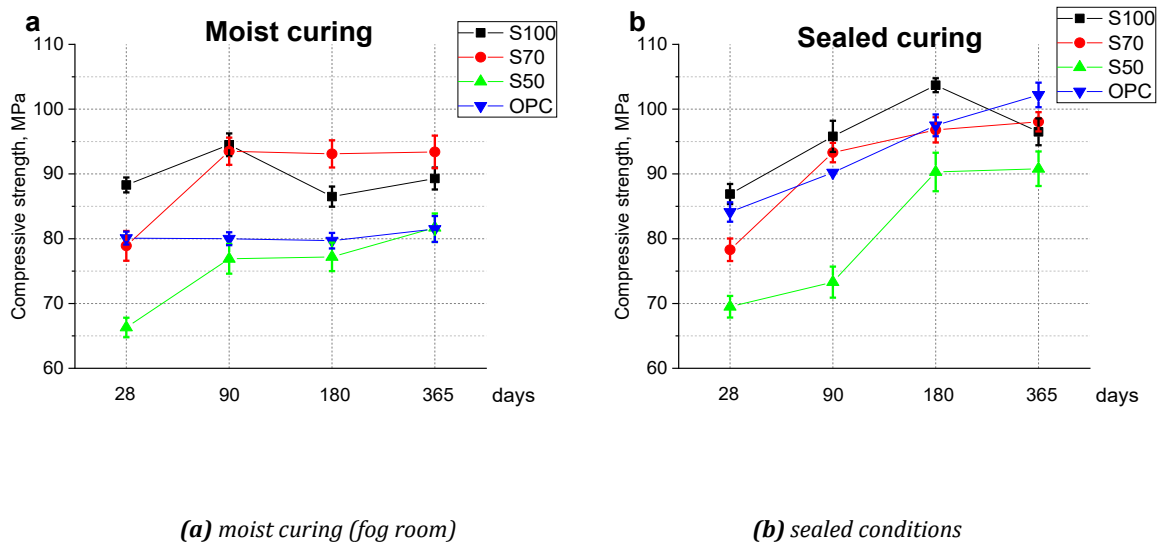
*Figure 3.5 Evolution of compressive strength of the samples stored at **(a)** moist (fog room) and **(b)** sealed conditions.*

3.3.1.2   Effect of precursor composition on compressive strength

From Figures 3.5 and 3.6 it can be inferred that the compressive strength of AAC mixtures strongly depends on the slag-to-fly ash ratio. This is convincingly shown in Figure 3.6. The 28 days compressive strength of S50 mixture is 20-25% lower than that of S100. These results agree with studies of Nedeljković et al. [146] and Prinsse et al. [77].

(a) *moist curing (fog room)*   **(b)** *sealed conditions*
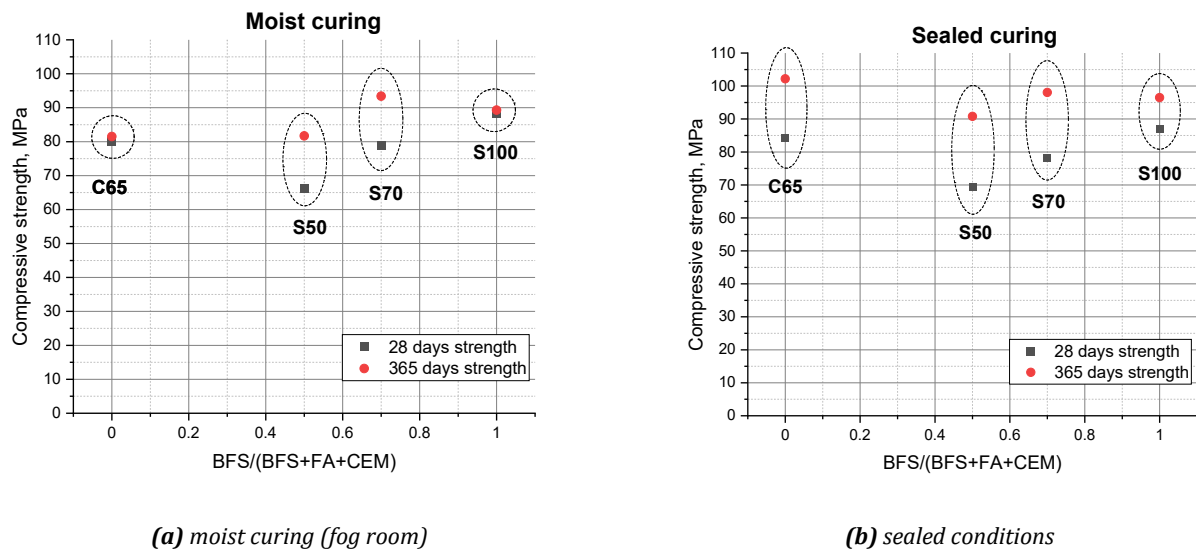
*Figure 3.6 Evolution of compressive strength as function of precursor composition **(a)** moist (fog room) and **(b)** sealed conditions.*

The lower compressive strength of the S50 mixture was explained by the different microstructure of the paste. The amount of solid gel formed during the first weeks is generally lower when slag is replaced by fly ash [162], since fly ash is less reactive than slag. At a later stage, typically in the period between 28 and 90 days, FA particles gradually dissolve and more solid gel is formed over time, accompanied by an increase in compressive strength [163].

Second possible reason can be, as was discussed in Chapter 2, a higher FA percentage in the mixture is associated with a decrease of Ca in the reactive system, which leads to formation of less C-A-S-H and more C-N-A-S-H gel. Then, according [164], there is less dense microstructure.

3.3.1.3   Effect of drying at 55% RH after 28 days on compressive strength

The evolution of compressive strength of samples stored at 55% relative humidity after initial fog room and sealed curing is shown in the Figure 3.7. The results showed slightly lower compressive strength compared to the samples cured continuously (Figure 3.5). Like in case of cured specimens, one possible reason for this may be the appearance of microcracks [60]. Additionally, the influence of eigenstresses probably contribute to this effect: the absence of hygral equilibrium leads to moisture gradients across the cross-section, resulting in internal stresses [255].

Minor reason could be more intensive leaching, although this leaching happens only in the surface zone [165]. Moreover, drying out of the concrete slowed down the reaction process, particularly in the drying outer zone of the specimens. Concretes containing the slower reacting slag and fly ash suffer more from drying than OPC-based concretes. Hence, the S70 and S50 concrete specimens did not reach the same strength as the samples stored in moist and sealed conditions.

(a) *moist curing up to 28 days (fog room)*   (b) *sealed curing up to 28 days*
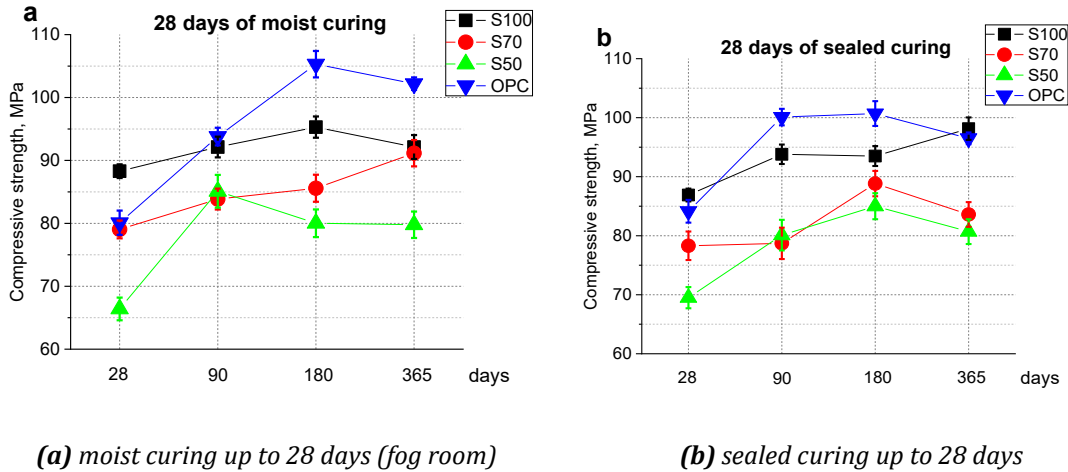
Figure 3.7 Evolution of compressive strength of the samples stored at 55% RH after 28 days different initial curing. Before 28 days: (a) moist (fog room) and (b) sealed curing.

The curing regime during the initial 28 days did not impact the long-term compressive strength stored at 55% relative humidity. The variation in compressive strength between AAC specimens following the initial sealed and moist curing at 180 and 365 days was less than 10%. These results align with the results reported by Lee et al. [26].

3.3.2   Elastic modules

3.3.2.1   Evolution of elastic modulus of moist and sealed cured specimens

The evolution of the elastic modulus of the samples stored under moist and sealed conditions until the age of 365 days is shown in Figure 3.8. The figure shows that the elastic modulus of PC concrete increases with time. This happens due to hydration process [10, 71, 122].
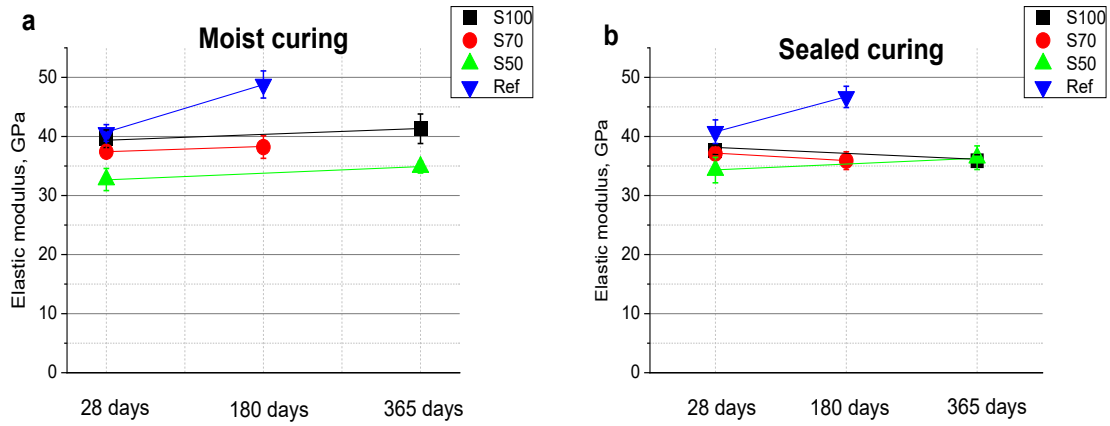
(a) 28 days moist curing (fog room)

(b) 28 days sealed curing

*Figure 3.8. The elastic modulus after 28 days, 0.5 and 1 year of storage at **(a)** moist (fog room) and **(b)** sealed conditions.*

Figure 3.8 also indicates minor (a few percent of the average) increase of the E-modulus of AAC specimens stored in moist conditions and minor decrease of the E-modulus of S70 and S100 specimens stored in sealed conditions for 180 or 365 days. From this it can be inferred that the long-term (180 or 365 days) storage of the concrete specimens at ambient moisture marginally affects their elastic modulus. The leaching of the concrete in the moist environment seems to affect only the outer layer of the samples and does not significantly affect the elastic modulus of AAC.

3.3.2.2   Evolution of elastic modulus of specimen exposed to 55% RH after 28 days

The evolution of the elastic modulus of the samples stored at 55% relative humidity after initial 28 days moist or sealed curing is shown in Figure 3.9. The figure shows that, also when exposed to 55% RH, the elastic modulus of the reference PC concrete increases with time. For AAC-specimens, however, a decrease of the E-modulus after exposure of the specimens to 55% RH was found for both moist and sealed initial curing conditions. Similar results have been reported by Prinsse [77], who also measured the elastic modulus of AAC after 28 days of curing and storage at 55% RH.
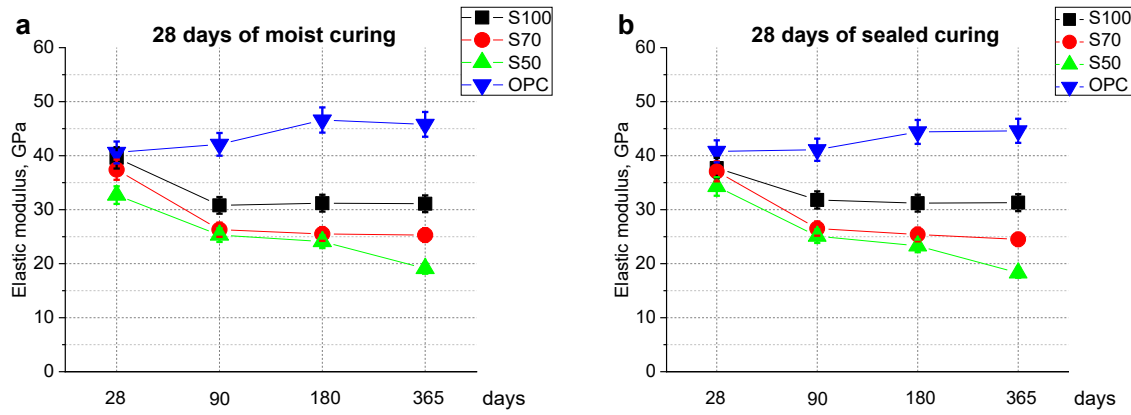
(a) *28 days moist curing (fog room)*   **(b)** *28 days sealed conditions*

*Figure 3.9 The evolution of elastic modulus of the samples stored at 55% RH after 28 days. Before 28 days: **(a)** moist (fog room) and **(b)** sealed curing.*

The severe drop of the ambient relative humidity from above 95% to 55% most probably induced substantial drying shrinkage and microcracking, thus damaging the concrete samples. This is in line with the conclusions drawn by Collins et al. [60]. Moreover, microcracks might have been induced also caused by high autogenous shrinkage [26, 162].

Figure 3.9 shows that the evolution of the elastic modulus of AAC specimen exposed to 55% RH (after 28 days) is significantly different from the behaviour of AAC samples stored under moist and sealed conditions (as shown in Figure 3.8). The E-modulus of AAC decreased by at least 20% during the first 90 days. This effect was observed for all slag-fly ash ratios and both types of initial curing conditions.

A notable decrease of the elastic modulus of AAC falls on the period from 28 to 90 days. This trend appears independent of the initial curing conditions. Similar results were reported by Lee et al. [26], who concluded that significant shrinkage led to the development of micro-cracks in the fly ash/slag AAC. As a consequence, both the elastic modulus and the long-term compressive strength were observed to decrease.

3.3.3   Splitting tensile strength

The evolution of splitting tensile strength of the samples exposed to 55% relative humidity after initial moist or sealed curing during 28 days are shown in the Figure 3.10. The evolution of the splitting tensile strength of AAC was, like that of the elastic modulus, substantially different from that of the reference concrete. The reference C65 samples showed an almost constant splitting tensile strength with time for initially moist cured specimen and a slight decrease for initially sealed cured specimens. It can be assumed that the decreasing trend of the tensile strength of AAC mixtures is caused by microcracks in the outer zone of the specimens. Additionally, the influence of eigenstresses may contribute to this effect [255].

(a) 28 days fog room (moist) curing   *(b) 28 days sealed curing*
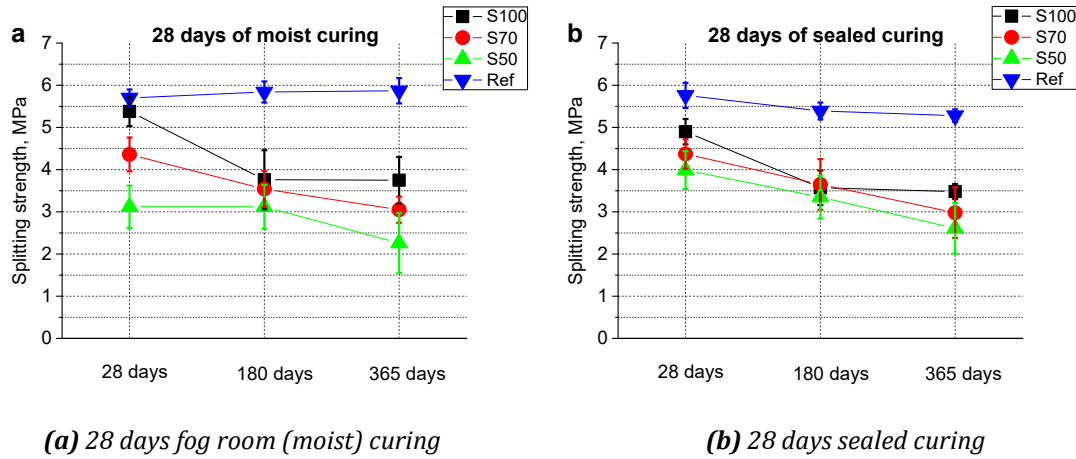
Figure 3.10. The evolution of splitting tensile strength of the samples stored at 55% RH after 28 days. Before 28 days: (a) moist (fog room) and (b) sealed curing.

The 28 days and 365 days splitting tensile strength strongly depend on the slag-fly ash ratio in the mixture (Figure 3.11). This correlates with the results of the compressive strength tests. The trend was the same for both initially sealed and moist cured samples.

(a) 28 days moist curing (fog room)   *(b) 28 days sealed conditions*
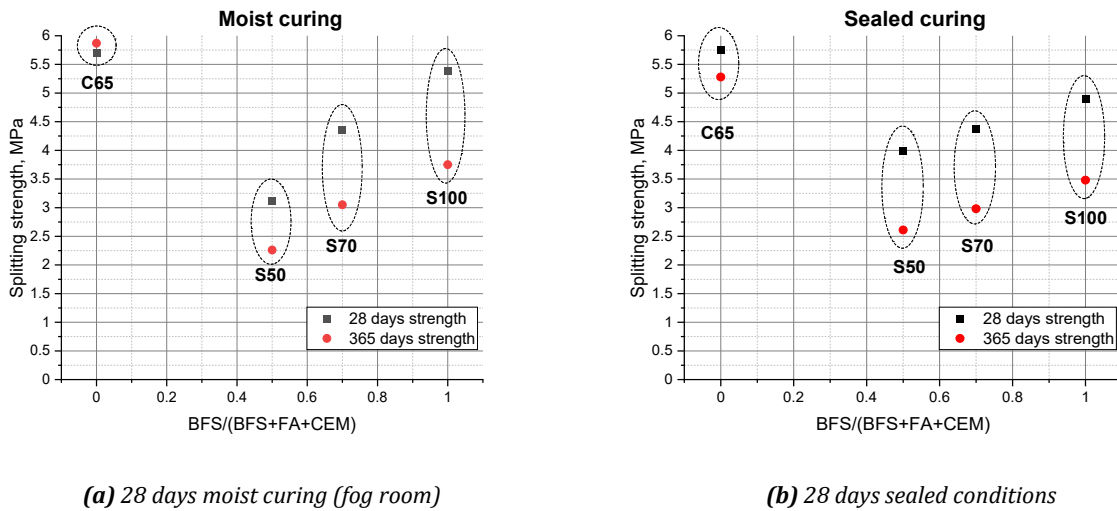
Figure 3.11 Evolution of splitting strength as function of precursor composition. Exposure condition RH 55% after 28 days. Before 28 days: (a) moist (fog room) and (b) sealed curing.

The data show a pronounced decrease in the splitting tensile strength with time for all AAC mixtures when exposed to 55% RH after both initial curing regimes (moist and sealed). This decrease was probably caused by internal microcracking caused by autogenous shrinkage of the cement paste. Stiff aggregates particles can act as local restraints to this type of shrinkage of the surrounding paste [166], resulting in microcracking in the concrete [162]. Moreover, some visual cracks were observed on the surface of the samples.

3.4 Observations and conclusions

This chapter dealt with the effect of type of precursor and curing conditions on the mechanical properties of AAC. The selected AAC mixtures for this study consisted of blast furnace slag and coal fly ash, mixed in various proportions. Ordinary C65 concrete, made of CEMI and CEMIII, was taken as reference. Moist and sealed curing conditions, followed by moist, sealed and 55% RH storage conditions were chosen to study the effect of exposure conditions (see Figure 3.3). Based on the experimental results the following conclusions were drawn:

1. The AAC mixtures showed to reach the same strength as a reference ordinary (OPC) concrete, but lower values of the elastic modulus and splitting tensile strength.

2. Mixing slag with fly ash decreased the overall compressive strength, splitting tensile strength and elastic modulus of concrete samples cured under both moist and sealed curing conditions during first 28 days after casting.

3. The AAC specimens cured in sealed conditions during the 28 days showed higher compressive strength, elastic modulus and splitting strength compared to the same specimens cured in the fog room. However, relatively slow-reacting AAC mixtures (S70 and S50) continued to react after 28 days forming their final microstructure. Therefore the effect of the initial curing regime was not pronounced for the specimens stored at 55% RH for the long-term.

4. The evolution of compressive strength was different from the evolution of the elastic modulus and splitting tensile strength of the AAC. The compressive strength increased with time up to the maximum value, then it remained stable with a slight tendency to decrease. The elastic modulus and splitting tensile strength of AAC specimens showed maximum values at the age of 28 days. Then the values of these mechanical properties decreased by 20-30% by the age of 90 days if stored at 55% RH. In contrast, the elastic modulus and the splitting tensile strength of the reference concrete C65 were stable with time while stored at 55% RH.

Chapter 4

Experimental study on creep and free shrinkage of AAC

4.1 Introduction

Time-dependent properties of concrete elements and concrete structures, such as creep and shrinkage, depend on many external factors and intrinsic properties [10]. External factors are the curing regime and exposure conditions, such as the ambient temperature, relative humidity, load level, duration of the loading, etc. The intrinsic properties concern the material characteristics, which are dictated by the concrete mixture (See Chapter 2).

The correlations between external factors and intrinsic properties on the one hand and the time-dependent behaviour of Portland Cement (PC) concrete on the other have been investigated for decades [10, 167, 168]. However, the time-dependent behaviour of alkali-activated concrete (AAC) has not been sufficiently studied yet. Only a few more or less comprehensive studies about the time-dependent properties of AAC have been published in past few decades [18, 133, 139, 169], as reviewed in Chapter 2.

Because of limited knowledge, accurate prediction models of time dependent behaviour in AACs have not yet been developed. The fib ModelCode 2010 [137] and EuroCode 2020 [8] provide formulas for the creep coefficient of PC concrete of any strength class, but fail to deliver accurate predictions for creep of AAC. Discrepancies are caused by the fact that the specific correlations between the input parameters (28-day compressive strength, elastic modulus) and creep coefficient of AAC are not the same as for PC concrete.

The aim of this chapter is to investigate the long-term creep and free shrinkage strain evolution of AAC experimentally and evaluate possible correlations between the obtained creep coefficient and the mechanical properties determined in Chapter 3.

Creep and shrinkage tests will be performed to measure the strain evolution and examine the influence of the main affecting factors, i.e. precursor ratio and curing conditions. With the measured total deformation, free shrinkage and elastic modulus of the AAC concretes, the creep coefficients will be calculated and compared with those of a reference PC-based concrete. The correlations between the creep coefficient, compressive strength and elastic modulus of the concrete mixtures will be analysed and discussed.

4.2 Materials and Methods

4.2.1 Materials and specimen preparation

The precursors used for studying time-dependent properties of AAMs were blast furnace slag (BFS) and fly ash (FA), the same as those used for the mechanical property tests described in Chapter 3. The properties of the raw materials were shown earlier in Table 3.1, while the mixture designs were shown in Tables 3.2 and 3.3. The AAM mixtures S100, S70 and S50 were studied. Concrete mixture C65 was taken as a reference. Note, that the volume ratio of paste to aggregate of the reference mixture differs from that of the AAC mixtures. The compositions of the four mixtures are summarized in Table 4.1(a).

Table 4.1(a) Summary of mixture compositions

Components	unit	C65 (Ref)	S100	S70	S50
			Mixtures		
CEM III	kg/m^3	260	--	--	--
CEM I	kg/m^3	220	--	--	--
Water	kg/m^3	183	--	--	--
Admixture	kg/m^3	4.08	--	--	--
Slag (BFS)	kg/m^3	--	400	280	200
Fly ash (FA)	kg/m^3	--	--	120	200
Activator	kg/m^3	--	200	200	200
Liquid/binder (l/b) ratio	--	0.381	0.5	0.5	0.5
Aggregate (0–4 mm)	kg/m^3	772	789	789	789
Aggregate (4–8 mm)	kg/m^3	882	440	440	440
Aggregate (8–16 mm)	kg/m^3	--	525	525	525

Table 4.1(b) Precursor ratio of mixtures used

Mass ratio of components	unit	C65 (Ref)	S50	S70	S100
			Mixtures		
BFS/(FA+BFS+CEM)	-	0	0.5	0.7	1

For the tests, concrete prisms ($100 \times 100 \times 400$ mm³) were cast in steel moulds. The samples were demoulded 24 hours after casting and then cured for 28 days under sealed and moist curing regimes. These regimes were chosen to evaluate the effect of ambient humidity on the evolution of the properties of the concrete specimens. After demoulding, one series of specimens was sealed with plastic film and was kept in a room with temperature of 20±2 °C (sealed curing). Another series was cured in the fog room, where a relative humidity of 100% was maintained (moist curing). After 28 days curing, some specimens were left under the curing conditions, while other specimens were moved and stored in a room with a relative humidity of 55±5% and a temperature of 23±2 °C for testing the creep, shrinkage and mechanical properties. The curing conditions and the timeline, discussed already in Chapter 3, are illustrated in Figure 4.1.
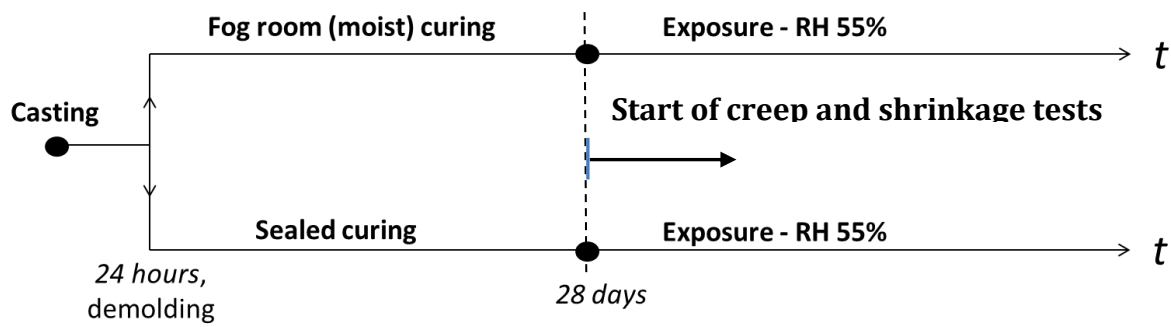
Figure 4.1 Schematic illustration of timeline for creep (and shrinkage) tests (including curing regimes).

4.2.2   Test methods – Shrinkage and creep

4.2.2.1   Free shrinkage tests

Standard drying shrinkage tests were conducted using concrete prisms according to AS1012.13-2015 recommendations [143] (Figure 4.2, right). It should be mentioned that in case relatively young concrete is exposed to drying, the concrete may still experience some autogenous shrinkage [170]. Although it remains a topic of debate for slow-reacting AAC systems [171], it is expected that by 28 days most of the autogenous shrinkage has already occurred [170]. It is assumed, therefore, that shrinkage of the drying specimens, starting after 28 days, is hardly affected by autogenous shrinkage. And as long as autogenous shrinkage continues to occur, its contribution to the measured drying shrinkage is considered negligible.

The shrinkage strain was calculated from the measured length changes of test prisms using the following formula:

$$\varepsilon_{\text{sh}}(\text{t}, \text{t}') \ = \ \frac{L(t) - L(t\prime)}{L(t\prime)}, \qquad L(t') = L_0 \tag{4.1}$$

where $\varepsilon_{sh}(t, t')$ is the free shrinkage strain of a concrete specimen, $L(t)$ is the length of the concrete specimen (prism), L_0 is the length of the concrete specimen at the start of the test. In our tests $L_0 = 200$ mm.

Figure 4.2 Photos of the ongoing creep test (left) and shrinkage test (right).

The measurements were performed using dial gauge. Dial gauge/indicator is a measuring instrument with which small displacements of a spindle are magnified by suitable mechanical means to a pointer rotating in front of a circular dial with a graduated scale with an accuracy of 0.01±0.005 mm (Figure 4.2, right). The first measurement was taken right after exposure of the specimens to the test conditions. Then, the measurements were taken every day until 28 days, then every week until 12 weeks, and then once a month.

The tests were performed under controlled laboratory conditions: relative humidity of 55±5% and temperature 20±2 °C.

4.2.2.2   Creep tests

The creep tests are executed according to the Australian Standard AS 1012.16— 1996 2, a standard that is used worldwide for AAC testing [14]. The test set up is shown in Figure 4.2 (left). During the test the samples were not sealed, therefore shrinkage also took place. Free shrinkage was measured separately on drying prisms, as described in 4.2.2.1.

The applied loading regime and typical total strain, basic creep and shrinkage strain curves are shown in Figure 4.3. The applied stress did not exceed 40% of the 28 days compressive strength.

The creep tests were used to determine the evolution of basic creep strain $\varepsilon_{cc}(t,t')$ and creep coefficient function $\phi(t, t')$ of the loaded concrete specimens. The basic creep of concrete is the time-dependent deformation that occurs when concrete is subjected to loading *without* drying.
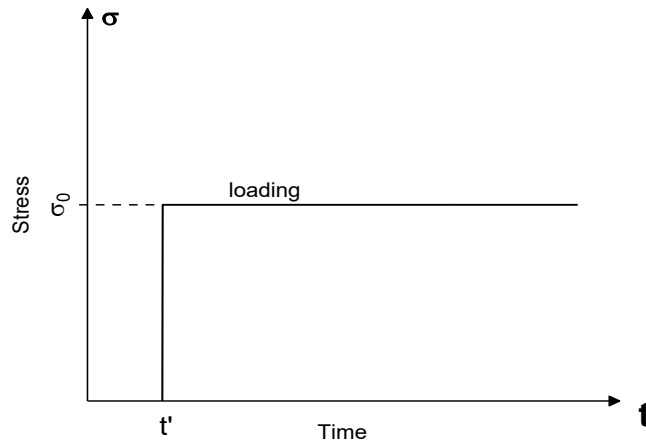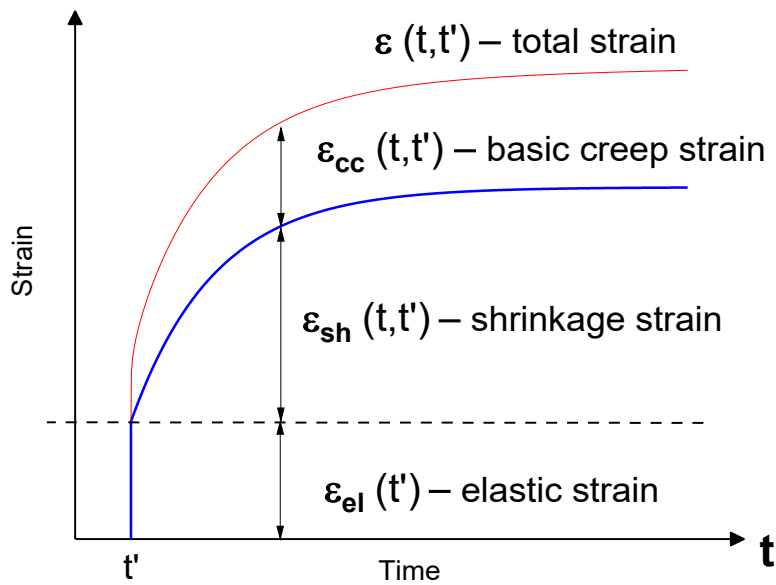
Figure 4.3 Load during the creep test (top) and strain response (bottom). σ_0 is applied load, total strain $\varepsilon(t,t')$ consists of: $\varepsilon_{cc}(t,t')$ is the basic creep, $\varepsilon_{sh}(t,t')$ is the free shrinkage strain, $\varepsilon_{el}(t')$ is the elastic strain measured on loading of a specimen at time t'.

4.2.2.3   Creep coefficient

Creep coefficient function $\phi(t, t')$ is defined as the basic creep $\varepsilon_{cc}(t,t')$ normalized to the elastic strain $\varepsilon_{el}(t')$ measured on loading of a specimen at time t'. For the creep function $\phi(t, t')$ it holds:

$$\phi(t, t') = \frac{\varepsilon_{cc}(t,t')}{\varepsilon_{el}(t')}$$
(4.2)

The elastic modulus $E_{ci}(t')$ at the moment of loading is obtained from:

$$E_{ci}(t') = \frac{\sigma_0}{\varepsilon_{el}(t')} \qquad - \qquad (4.3)$$

where σ_0 is the applied stress and $\varepsilon_{el}(t')$ the measured elastic strain.

4.2.2.4 Non-sealed creep tests

Creep tests were conducted under the same conditions as the free shrinkage tests: relative humidity of 55±5% and temperature 23±2 °C. This test procedure implies that the total measured strain includes direct elastic strain, basic creep, drying shrinkage and drying creep. In this study basic creep and drying creep are taken together, while drying shrinkage is measured on unloaded shrinkage specimens. Thus, the basic creep strain can be obtained from the total measured strain using the formula (see also Figure 4.3, bottom):

$$\varepsilon_{cc}(t,t') = \varepsilon(t,t') - \varepsilon_{el}(t') - \varepsilon_{sh}(t,t') \qquad (4.4)$$

where $\varepsilon_{cc}(t,t')$ is the basic creep strain (here including drying creep), $\varepsilon(t,t')$ the total measured strain, $\varepsilon_{el}(t')$ the elastic strain at the moment of application of the load and $\varepsilon_{sh}(t,t')$ the free shrinkage strain, t' the time of loading and t the time of executing the measurements.

4.2.2.5 Executing creep and shrinkage tests

The compressive load for the tests was provided by an electric pump. The test device consisted of a system of valves and an oil-and-gas element. The load was transferred onto the specimen using a fixing plate, hydraulic jack and a loading plate (Figures 4.4 and 4.5). The stress level was controlled through sensors with an accuracy of ±0.05 kN, which were installed in the test set-up. Before executing the test, several identical specimens were preloaded three times up to 100 kN to calibrate the set-up.

An automatic control system (Figure 4.4) was used for in-situ strain measurements. Potentiometers were used to measure longitudinal strains on each specimen. A special monitoring and data acquisition system was developed to collect and store the test data. The data from each sensor was transmitted simultaneously through a multiplexer for all potentiometers. An analogue-to-digital converters (A/D) transmitted the data to a personal computer, which recorded it in the data storage.

As indicated in the previous section, the creep samples were not sealed. Hence, the measured strain was not only creep strain, but the joint effect of creep and (free) shrinkage. To determine free drying shrinkage, shrinkage tests were performed on prisms identical to the loaded prims and made from the same casting batch. The creep strain was then calculated with Eq. 4.4.
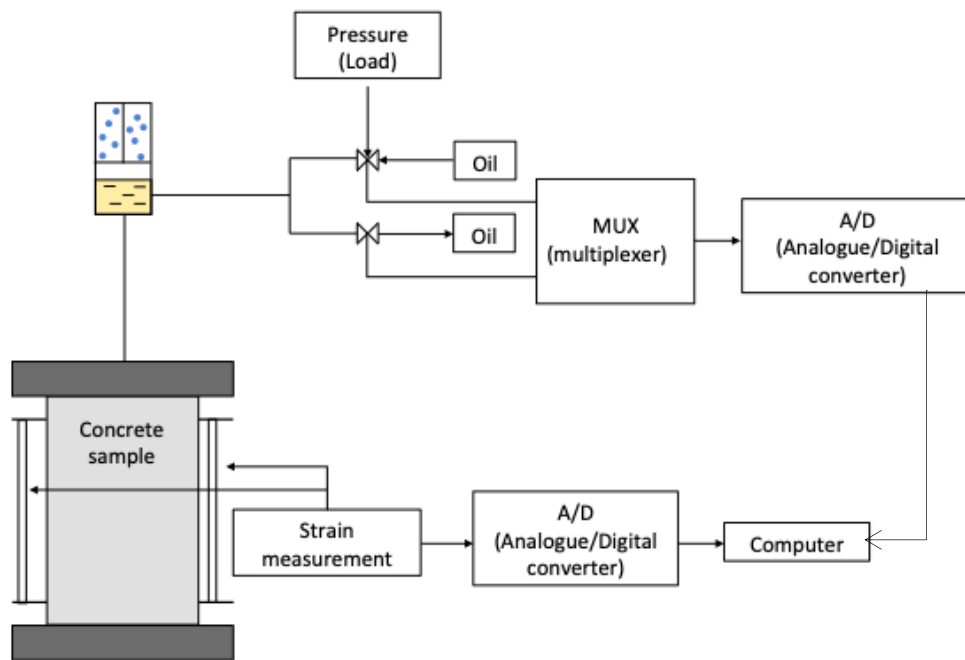
Figure 4.4 Schematic arrangement of the creep testing setup with an *automatic control system.*
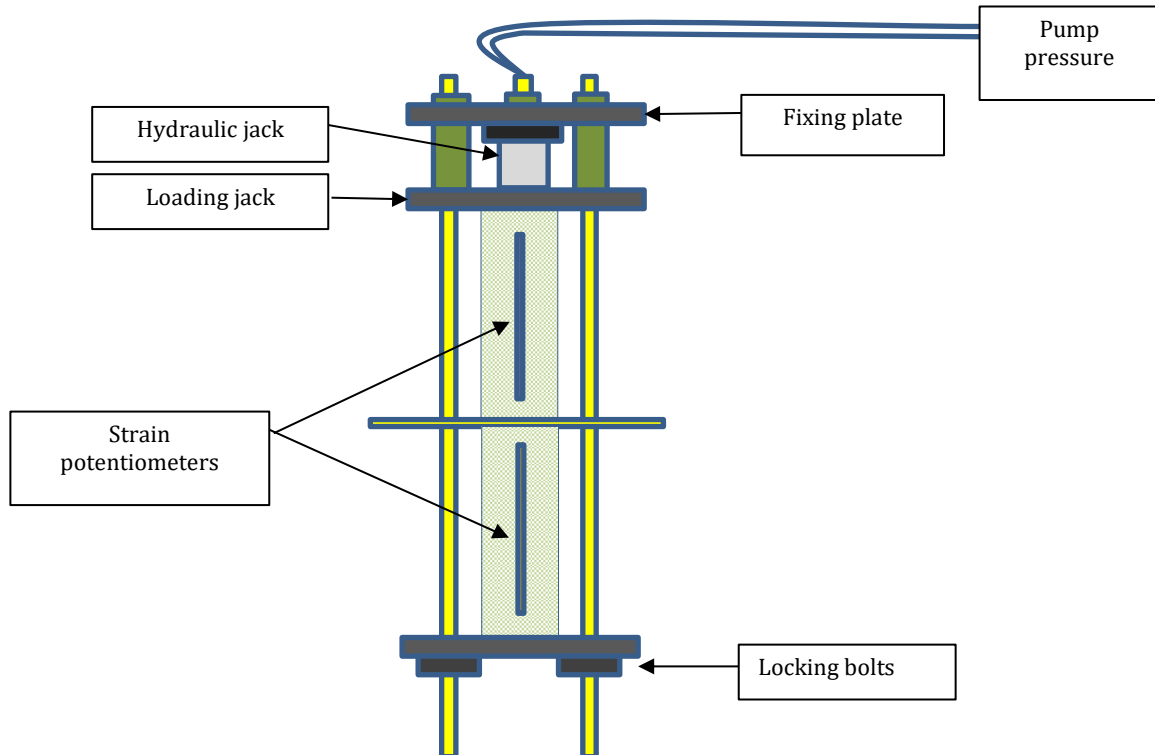
Figure 4.5 Compressive loading frame (set-up, see also Figure 4.2).

4.3 Results and discussion

4.3.1 Drying shrinkage

4.3.1.1 Overview of measured shrinkage curves

The results of free shrinkage tests during 365 days of the four mixtures presented in Table 4.1 are shown in Figure 4.6. For the mixtures S100 and S50, Figure 4.7 shows the results of free shrinkage during 900 days. The results are in good agreement with those presented by Humad [172, 173], who also measured drying shrinkage of AAM concrete mixtures based on FA and BFS.

The strain data was approximated with an exponential function, i.e. Eq. 4.5:

$$\varepsilon\,(t) = \varepsilon_0\,(1 - \exp(-t/t_0)) \tag{4.5}$$

where ε_0 is the ultimate value of shrinkage strain and t_0 is characteristic time of the approximation function. The parameters of the approximation function (4.5) are summarized in Table 4.2. The larger the characteristic time t_0, the slower the shrinkage deformation will reach its ultimate value. Note, that t_0 is not a material property, but a parameter that determines the shape of the shrinkage curve of the drying specimen.

Table 4.2. Free shrinkage test results. Values of ε_0 and t_0.

Tested mixture	Precursors' composition (see Table 4.1(b)) BFS/ (FA+BFS+CEM(I+III))	Ultimate shrinkage strain ε_0 [%]		Characteristic time t_0 [days]	
		moist curing	sealed curing	moist curing	sealed curing
C65	0	0.039	0.031	67.5	81.9
S50	0.5	0.056	0.045	25.0	37.6
S70	0.7	0.058	0.043	37.9	77.7
S100	1.0	0.054	0.047	65.0	88.3

Shrinkage data have shown some variations and irregularities (see Figure 4.7). Plausible reasons for these irregularities are the changes in temperature and relative humidity during the test, which were in-situ monitored. Most likely, a sudden drop of temperature caused rapid contraction and resulted in a sudden drop in shrinkage, while a sudden rise of temperature or humidity caused expansion and leaded to a spike in shrinkage.

In general, the shrinkage strains in AAC were significantly higher than those of the reference PC concrete, even when accounting for the lower amount of paste in C65 mixture. Mixing slag with fly ash in an AAC mixture increased shrinkage, but the difference was not dramatic. Both AAC and PC concrete specimens cured under moist condition during the first 28 days showed larger drying shrinkage than specimens cured under sealed condition due to larger amount of accumulated internal moisture.
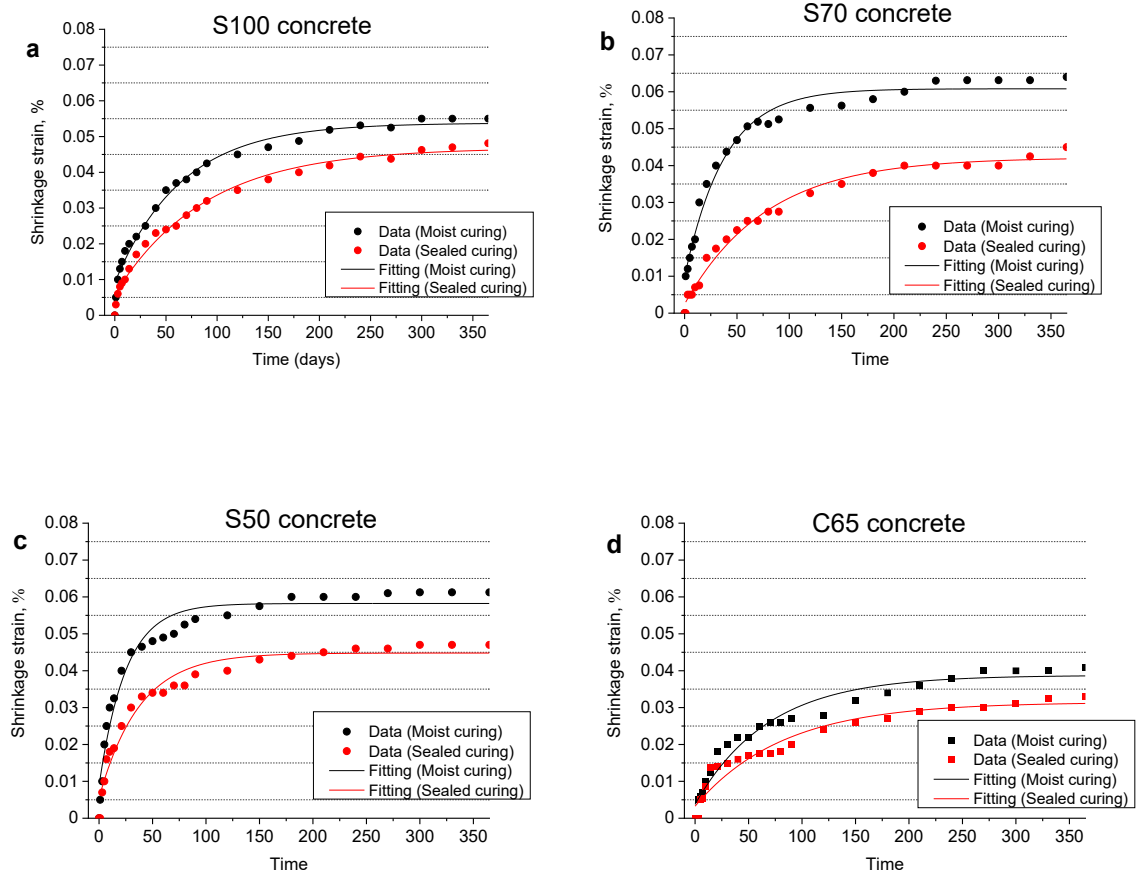
*Figure 4.6 Evolution of free shrinkage deformation during 365 days after curing for **(a)** S100 **(b)** S70 **(c)** S50 **(d)** C65 concrete mixtures. The data was approximated with the exponential law (Eq. 4.5).*
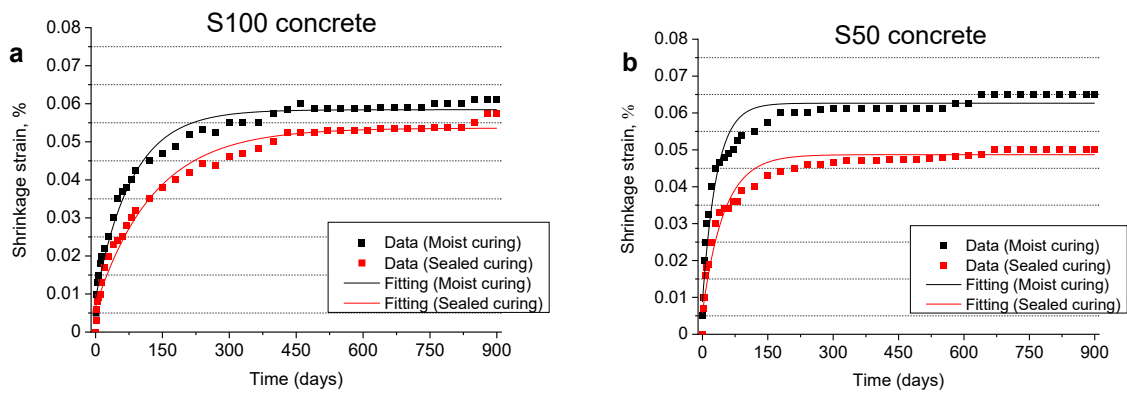
*Figure 4.7 Evolution of free shrinkage deformation during 1000 days after curing for **(a)** S100 and **(b)** S50 concrete mixtures. The data was approximated with the exponential law (Eq. 4.5).*

4.3.1.2 Influence of precursor ratio on drying shrinkage

The maximum or ultimate strain ε_0 and characteristic time t_0 of the shrinkage curves are summarized in Table 4.2. The ultimate free shrinkage ε_0 of AAC did not significantly vary with changing precursor ratio, i.e. the ratio between BFS and FA. However, the characteristic time t_0 of the shrinkage curves decreased with increasing FA content in the mixture, which implies rapid shrinkage development. The characteristic time of the shrinkage curves of S50 specimens was about 60% lower than that of S100 specimens. This was found for specimens cured under both sealed or moist conditions.

The ultimate shrinkage ε_0 of the AAC mixtures was higher than that of the reference C65 concrete. The characteristic time t_0 of the shrinkage curve of the C65 specimen was very close to that of the S100 specimens. Similar observations have been presented in literature [171, 174, 175].

Shrinkage of AAC is known to be correlated with the pore size distribution. Collins et al. [129] have shown that the higher shrinkage strain in slag-based AAC, compared with that of PC concrete, can be related to the pore size distribution of the alkali-activated binder. For alkali-activated slag pastes, the percentage of pores within the mesoscale range (1.25–25 nm) is 74.0–82.0%, while the percentage of mesopores in OPC pastes is only 24.7–36.4% [128].

4.3.1.3 Influence of curing conditions on shrinkage

The ultimate shrinkage strain ε_0 of moist cured specimens is higher than that of sealed cured specimens (Table 4.2). The difference was about 15% for the S100 mixture and about 29% for the S50 mixture.

The characteristic time t_0 was shorter for specimens cured under moist conditions (the shrinkage strain reached ultimate value more rapidly): 26% higher for the S100 mixture and 34% higher for the S50 mixture (Table 4.2).

This gap relates to the smaller volume of capillary pores in sealed cured samples, which contain evaporable water. Therefore, the weight loss (the loss of evaporable water) in sealed-cured specimens is much lower than in moist-cured specimens [176]. For the same reason, the weight loss is higher for blended AAC mixtures, like S50, than in pure slag-based mixtures, like S100 [177], as shown in Figure 4.8.
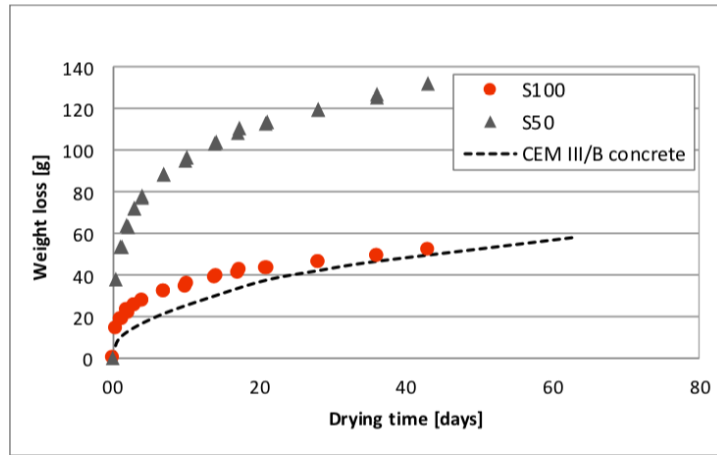
Figure 4.8 Weight loss for one S50 and one S100 AAC sample that have been wet-cured (20 ℃ and 95% RH) for 92 days. After this, the samples were exposed to laboratory conditions (20 ℃ and 55% RH). Also plotted is weight loss for a CEM III/B concrete sample (with the same dimensions), wet-cured for 28 days and then exposed to drying, data from Mors (2011). Captured from [177].

4.3.1.4 Drying shrinkage versus mechanical properties

Curing conditions *prior* to drying affected the evolution of both drying shrinkage and the mechanical properties. It is not surprising, therefore, that in the past correlations were assumed between shrinkage and mechanical properties like strength and modulus of elasticity. The ultimate values of shrinkage strain were reached much later than at 28 days; nevertheless, we use the 28 days strength as a reference mechanical characteristic of the concrete mixture.

Figures 4.9 and 4.10 show the ultimate shrinkage strains of specimens that were either moist or sealed cured prior to drying (Table 4.2) as a function of the 28 days compressive strength and elastic modulus, respectively. The 28 days compressive strength and elastic modulus of the mixtures have already been presented and discussed in Chapter 3.

In the strength range of about 65 MPa to over 85 MPa no clear correlation between 28 days strength and ultimate shrinkage was observed, either for initially sealed or the moist cured specimen. That correlation would be anticipated in the case of conventional concrete. The ultimate shrinkage of the reference mixture C65 was significantly lower than that of the AAC mixtures with the same 28 days compressive strength (Figure 4.9). A similar picture holds for the correlation between the 28 days elastic modulus and the ultimate shrinkage (Figure 4.10). Also here the reference mixture C65 behaves differently from the AAC mixtures. This observation confirms the previously mentioned fact that some correlations between drying shrinkage and mechanical properties, which were found to be valid in case of Portland cement concretes, do not apply to AAC mixtures due to the differences of the characteristic times.

71
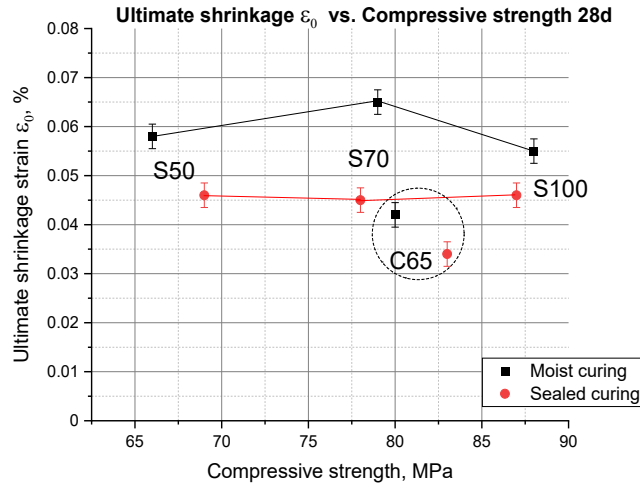
Figure 4.9 Ultimate shrinkage strain ε₀ obtained after shrinkage data approximation versus the 28 days compressive strength of the tested concrete.
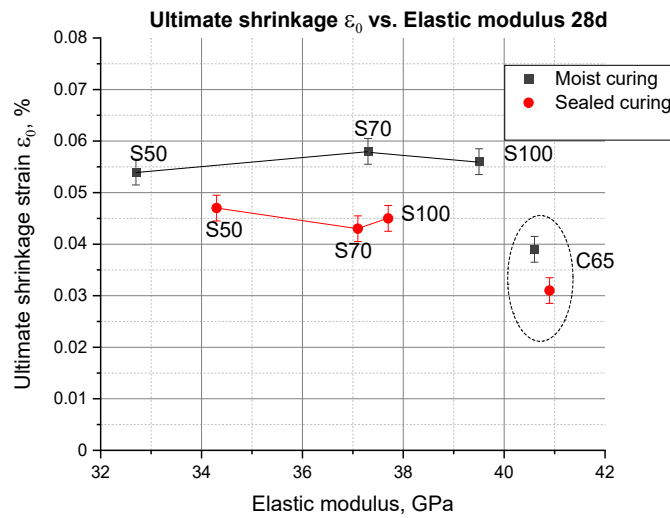
Figure 4.10 Ultimate shrinkage strain ε₀ obtained after shrinkage data approximation versus the 28 days elastic modulus of the tested concrete.

4.3.2   Creep test results

4.3.2.1   Load stress level and instantaneous elastic strain

A compressive creep test is the standard test for determining the creep properties of a concrete mixture [10, 14, 168]. A typical creep curve was previously shown in Figure 4.3. As already mentioned, the load (stress) level for the creep tests should not exceed 40% of the 28 days compressive strength, to avoid a non-linear stress-strain relationship.

The creep strain of a loaded specimen is determined by subtracting the instantaneous elastic strain and the free shrinkage strain from the total measured strain, according Eq. 4.4. This procedure implies that creep and free shrinkage strains are considered independent values for which the principle of superposition holds. The applied stress σ_0, the instantaneous elastic strain ε_{ci} observed in the creep tests and the elastic modulus E_{ci}, measured during the creep tests, and the 28 days elastic modulus E_{28d}, measured in Chapter 3 for the four mixtures C65, S100, S70 and S50, are all summarized in Table 4.3.

The difference between the instantaneous elastic modulus E_{ci} and the measured 28 days elastic modulus E_{28d} (as shown in Chapter 3) is less than 10%. This is in agreement with results of Un [18].

Table 4.3. Initial loading level σ_0 and elastic strain ε_{ci}

	28 days strength		Loading stress		Instantaneous elastic strain		Instantaneous elastic modulus		Measured elastic modulus	
	f_0		σ_0		ε_{el}		Eci		E_{28d}[*]	
Tested mixture	MPa		MPa		%		GPa		GPa	
	moist curing	sealed curing	moist curing	sealed curing	moist curing	sealed curing	moist curing	sealed curing	moist curing	sealed curing
C65	80.1	84.1	23.9	25.2	0.062	0.060	38.5	42.0	40.6	40.8
S100	88.3	86.9	35.3	34.7	0.096	0.099	36.8	35.0	39.6	37.7
S70	78.9	78.3	23.7	23.4	0.065	0.068	36.5	34.4	37.4	37.1
S50	66.3	69.5	22.1	23.2	0.070	0.071	33.1	32.5	32.7	34.3

[*] Measurement data presented in section 3.3.2

4.3.2.2   Measured creep curves

The total strain of the creep specimens was measured as the average strain of two tested specimens of each mixture. The creep tests lasted for 365 days. The measured total strain curves are presented in Figure 4.11.

4.3.2.3   Creep coefficient

From the measured total strain and shrinkage curves, the basic creep curves were obtained using Eq. 4.4. From the thus obtained basic creep the creep coefficient ϕ(t,t') has been calculated with Eq. 4.2. The evolution of the creep coefficients over a period of 28 days and 365 days after application of the load is shown in Figures 4.12 and 4.13, respectively. Note that in this study the obtained basic creep is in fact the sum of *(real) basic* and *drying creep* (see also section 2.4 and [10]). This approach is considered acceptable here, since the focus of this study is on the difference between the overall performance of AAC-mixtures and the reference OPC-concrete.
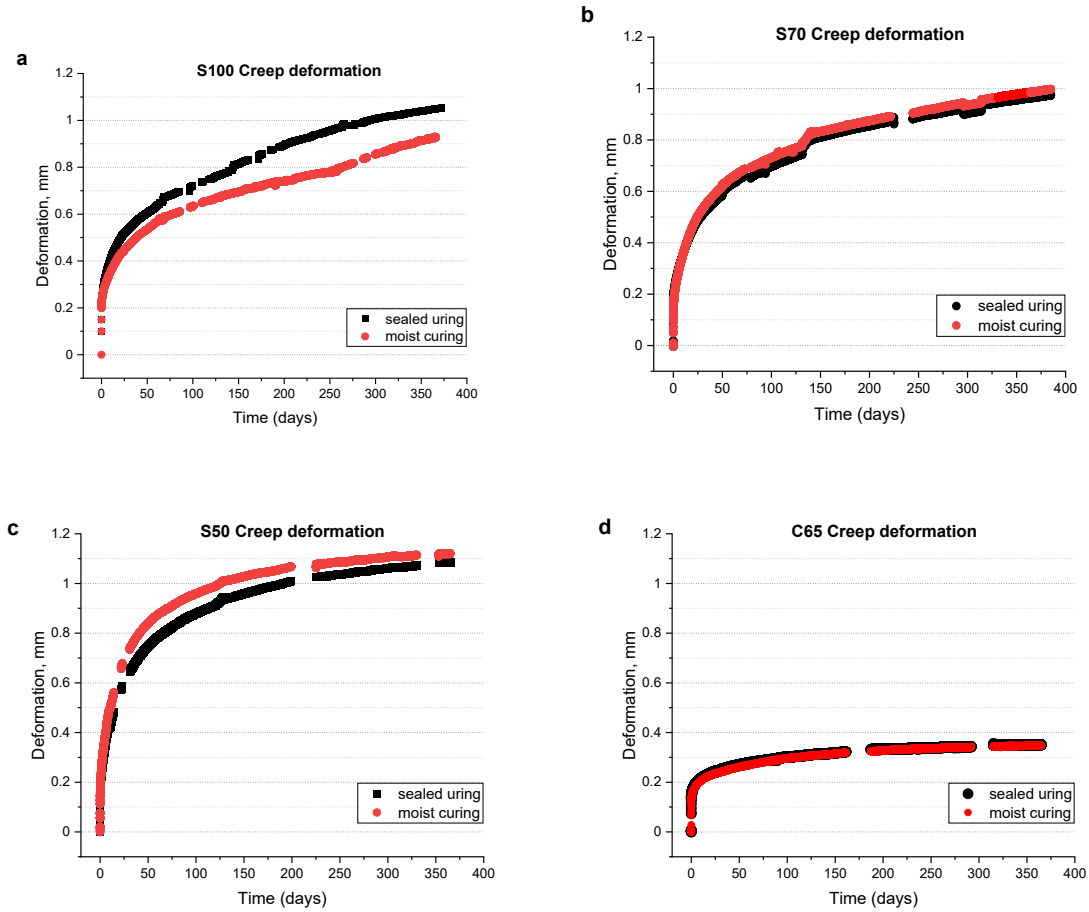
*Figure 4.11 Evolution of measured total strain during 365 days after curing for **(a)** S100 **(b)** S70 **(c)** S50 **(d)** C65 concrete mixtures.*

a. *Moist curing until 28 days*   b. *Sealed conditions until 28 days*
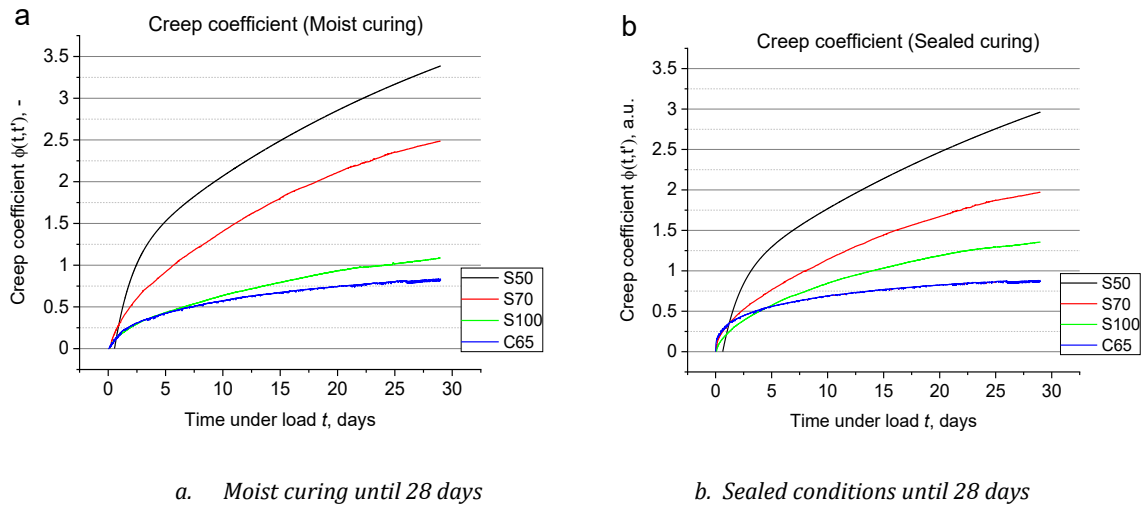
*Figure 4.12 Evolution of the creep coefficient during 28 days after 28 days of **(a)** moist and **(b)** sealed curing and loading initiation.*

| | a. Moist curing until 28 days | b. Sealed curing until 28 days |
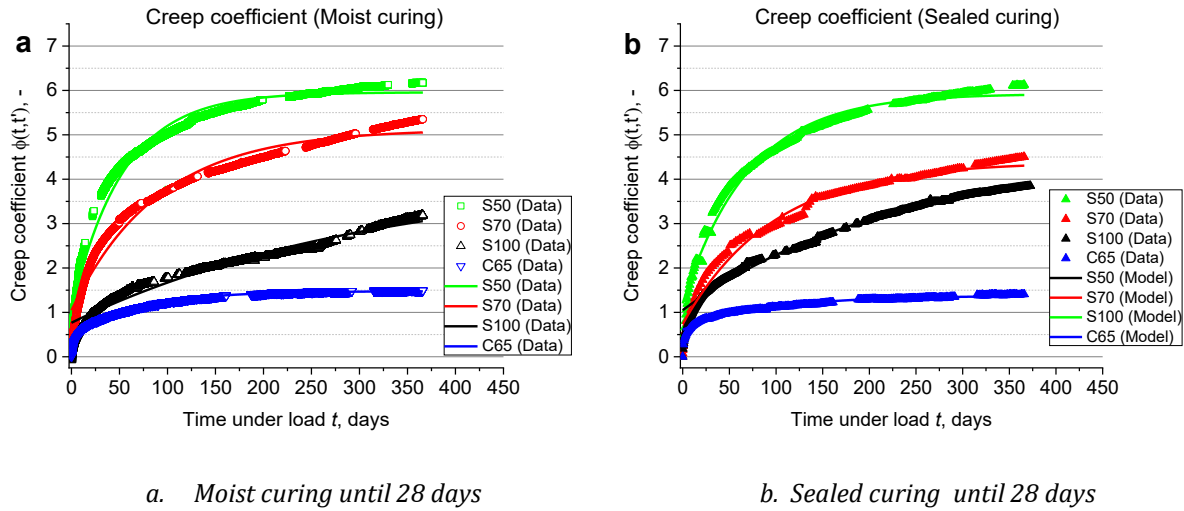
Figure 4.13 Evolution of the creep coefficient during 365 days after 28 days of **(a)** moist and **(b)** sealed curing and loading initiation.

The Figures 4.12 and 4.13 show that the creep coefficients of AAC specimens are significantly higher than those of the reference concrete C65. In contrast to the reference PC concrete, the creep coefficients of the AAC mixtures continue to increase even after one year under load (Figure 4.13).

The curves for the creep coefficients were approximated with the exponential function:

$$\phi(t) = \phi_0 \, (1 - B' * \exp(-t/t_0')) \tag{4.6}$$

where ϕ_0 is an ultimate creep coefficient, B' is a fitting parameter close to 1, and t_0' is the characteristic time which determines the shape of the creep curve. For long creep times, the creep coefficient tends to ϕ_0. Table 4.4 summarizes the results of the ultimate creep coefficient ϕ_0 and the characteristic time t_0'. Note, that these parameters are the result of approximation, therefore the maximum value of measured creep coefficient can be slightly larger than the value of ϕ_0.

Table 4.4 Ultimate creep coefficient ϕ_0 and characteristic time t_0 of four tested mixtures

Tested mixture	Precursor composition BFS/ (FA+BFS+CEM(I+III))	Ultimate creep coefficient ϕ_0 [-]		Characteristic time t_0' [days]	
		moist curing	sealed curing	moist curing	sealed curing
C65	0	1.48	1.37	65.76	87.9
S50	0.5	5.96	5.92	53.53	70.64
S70	0.7	5.12	4.38	90.35	96.64
S100	1.0	4.1	4.48	317.03	222.3

75

As said, the creep of AAC mixtures was much higher than that of the reference mixture C65. S50 specimens demonstrated ultimate creep coefficients ϕ_0 4.3 and 4.0 times higher than C65 specimens cured under sealed and moist conditions, respectively. The characteristic times of the creep curves of the C65 specimens cured under sealed and moist conditions were 2.5 and 4.8 times shorter than those of the S100 specimens, respectively. In other words, the creep strain develops more rapidly in C65 compared to S100. These results are in agreement with the findings of Un [18]. The possible reason for this is the difference in microstructure and resulting difference in creep mechanisms. The difference of creep mechanisms in PC and AAC will be discussed in Chapter 5.

4.3.2.4 Effect of precursor ratio on ultimate creep coefficient ϕ_0 and characteristic time t_0

The effect of the precursor ratio on the ultimate creep coefficient ϕ_0 and the characteristic time t_0 is shown in the Figures 4.14 and 4.15, respectively. The figures for mixtures of slag with fly ash, i.e. the mixtures S50 and S70, show a higher ϕ_0 and a lower t_0' of the creep coefficient function than the mixture with only slag, i.e. S100. For AAC mixtures the parameters ϕ_0 and t_0' can be approximated with linear functions of the BFS/(BFS+FA+CEM) ratio, viz.:

$$\phi_0 = -3.15 + 7.3*(BFS/(BFS+FA+CEM)) \qquad 0.5 \leq BFS/(BFS+FA+CEM) \leq 1.0 \qquad (4.7)$$

$$t_0' = -170 + 430*(BFS/(BFS+FA+CEM)) \qquad 0.5 \leq BFS/(BFS+FA+CEM) \leq 1.0 \qquad (4.8)$$

Figure 4.14 also clearly shows that the ultimate creep coefficient ϕ_0 of AAC mixtures is significantly higher than that of the reference mixture C65. Furthermore, the ultimate creep coefficient ϕ_0 of S50 specimens of sealed cured specimens was 5.92, which is 32.1% higher than the value of 4.48 of S100. For moist cured specimens the ultimate creep coefficient ϕ_0 of S50 specimens was 5.96, which is 45.4% higher than 4.1 of S100.

The characteristic time t_0' of AAC specimens decreased when blending slag with fly ash, similar to the shrinkage evolution (Table 4.4). For sealed cured specimens the t_0' of S50 mixtures was 70 days, which is 68.2% lower than 222 days of S100 specimens. For moist cured specimens the t_0' of S50 specimens was 53 days, 83.1% lower than 317 days of S100 specimens.
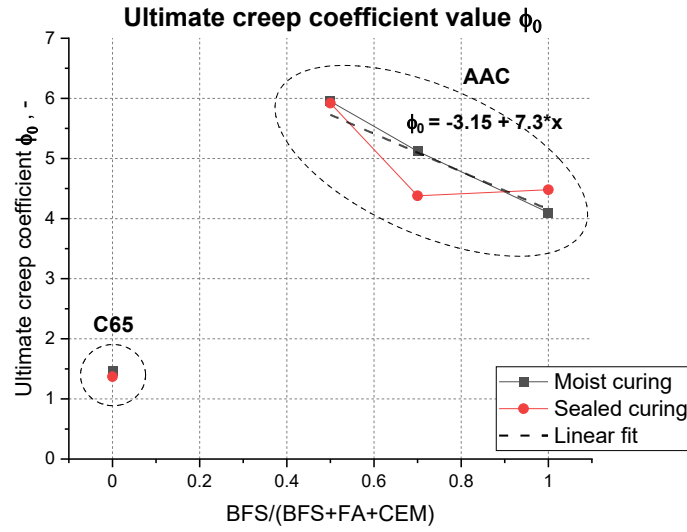
Figure 4.14 Ultimate creep coefficient ϕ_0 obtained after creep test data approximation versus BFS/(BFS+FA+CEM) ratio.
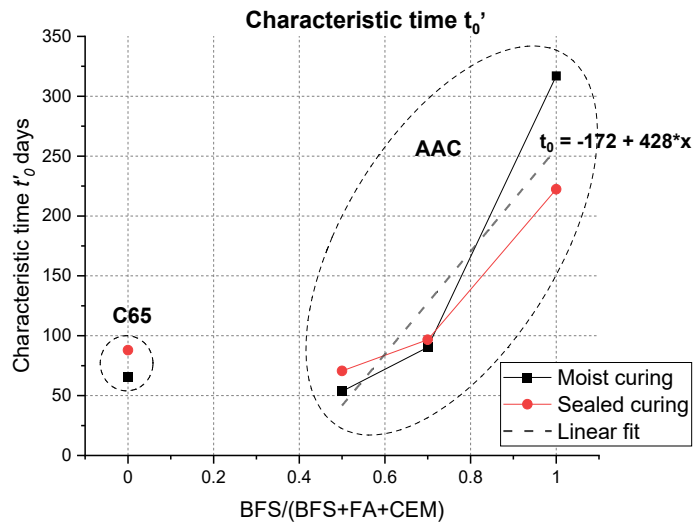
Figure 4.15 Characteristic time of creep coefficient t_0' obtained after creep test data approximation versus BFS/(BFS+FA+CEM) ratio.

The exact reason for the observed influence of the precursor ratio on the rate of creep, and maybe on the creep mechanism of AAC mixtures, is not clear yet. The creep mechanism of AAC will be considered in the next chapters. What we do know, however, is that by mixing slag with fly ash mixtures are obtained with lower 28-days compressive strength. The 28 days compressive strength of S50 mixture were 20-25% lower than that of S100 mixtures (Figures 3.5, 3.6). The increase of the creep coefficient with the decrease of the 28 days compressive strength in AAC was also mentioned in the study of Hojati [178].

4.3.2.5 Creep coefficient and creep compliance vs. mechanical properties

For creep analysis of real concrete structures, one can use the single material characteristic – the compliance function $J(t, t') = [1 + \phi(t, t')]/E(t')$ (1/MPa), where t' is the age of concrete when the constant stress (load) is applied [1]. In this study t' is 28 days. Figures 4.16 and 4.17 show the ultimate creep coefficient ϕ_0 and the ultimate creep compliance $J(\phi_0)$ of the specimens cured in moist and sealed conditions versus the 28 days compressive strength and elastic modulus, respectively. The details of the mechanical properties tests and test results were described in Chapter 3, namely in paragraphs 3.2.3, 3.3.1, 3.3.2.
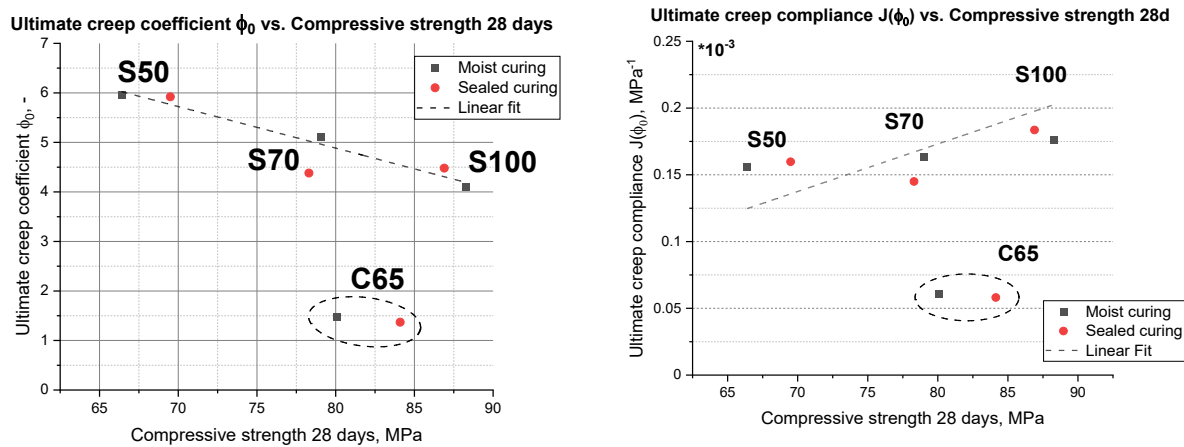
Figure 4.16 Ultimate creep coefficient (left) and ultimate creep compliance (right) versus the 28 days compressive strength of the tested concrete.
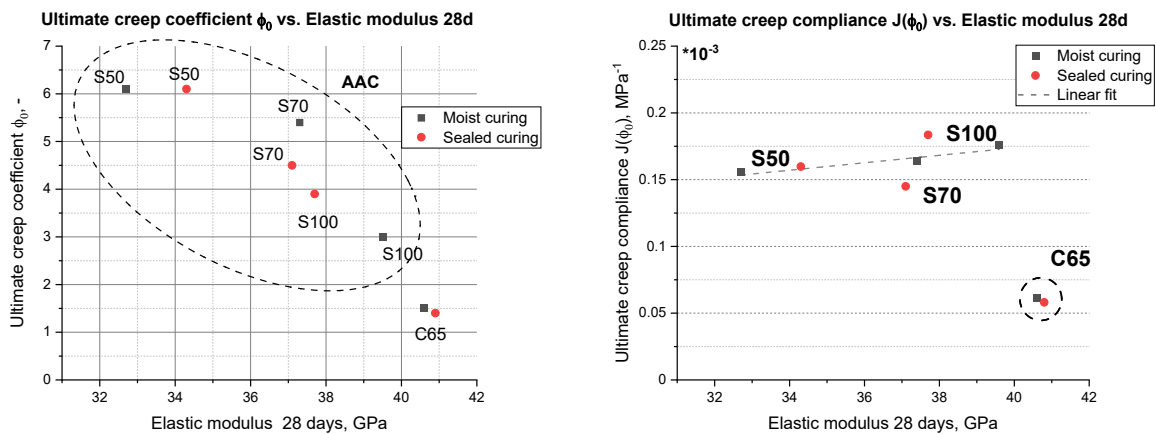
Figure 4.17 Ultimate creep coefficient (left) and ultimate creep compliance (right) versus the 28 days elastic modulus of the tested concrete.

The diagrams of ϕ_0 and $J(\phi_0)$ versus 28-day compressive strength and elastic modulus of the AAC and OPC C65 concrete did not show a clear correlation between the mechanical

78

properties and the creep coefficient. In general, the increase of the 28 days compressive strength and elastic modulus went along with the increase of the creep compliance and the decrease of the ultimate creep coefficient. All AAC mixtures showed significantly higher creep coefficients than C65, despite their similar 28-day compressive strength and elastic modulus. In order to understand the underlying reasons for this behaviour, the mechanisms of creep and the governing parameters of the creep coefficient function in AAC need more attention. This will be done in Chapter 5.

4.4   Observations and conclusions

The aim of this chapter was to experimentally investigate the evolution of long-term creep of AAC mixtures and to evaluate the correlations between the obtained creep coefficients and mechanical properties. The creep tests were executed according to standard recommendations. The effect of raw materials and curing conditions on creep and shrinkage strain of AAC were investigated. AAC mixtures selected for this study were made of blast furnace slag (BFS) and coal fly ash (FA), mixed in different proportions. An ordinary Portland-cement C65 concrete mixture was taken as a reference. The specimens were cured under moist or sealed conditions until loading. The results were analysed qualitatively and quantitatively. Based on the observations, the following remarks can be made:

1. The free shrinkage of AAC specimens, subjected to 55% RH at an age of 28 days, was, in general, higher than that of the reference C65 concrete. The shrinkage strain developed rapidly up to the ultimate value and further evolved with low strain rate. Short-term shrinkage in AAC was larger for the mixtures with a higher percentage of fly ash. However, the final value of the deformation did not show significant dependence on the precursor ratio. The curing conditions during the first 28 days, prior to exposure to the 55% RH, affected the shrinkage evolution. The specimens cured under moist conditions showed larger shrinkage and shorter characteristic time than the specimens cured under sealed conditions up to an age of 28 days.

2. An analysis of the diagrams of the ultimate shrinkage strain versus 28-day compressive strength and elastic modulus of the AAC and OPC concrete was made. The ultimate shrinkage of the AAC mixtures did not vary significantly with the 28-day compressive strength or elastic modulus (Figures 5.9 and 5.10), but was higher than that of the reference OPC concrete.

3. The AAC mixtures showed significantly higher creep than the reference PC concrete C65. Moreover, unlike C65, the creep curves of the AAC mixtures showed continuous growth, even after one year under load.

4. The evolution of the creep coefficient in AAC showed clear dependence on the precursor composition. Blending slag with fly ash resulted in mixtures with higher ultimate creep ϕ_0 and faster creep deformation (i.e. shorter characteristic time t_0'). The

ultimate creep coefficient and characteristic time were plotted as a function of the precursor mass ratio, showing linear trends.

5. The diagrams of the ultimate creep coefficient and ultimate creep compliance versus 28-day compressive strength and elastic modulus did not reveal a clear correlation between mechanical properties and the creep coefficient. Despite similar 28-day compressive strength and elastic modulus, all AAC mixtures showed significantly higher creep coefficients than the reference PC concrete. Further investigation is required to understand the underlying reasons for this behaviour, and a subsequent chapter will focus on the mechanisms of creep and the governing parameters of the creep coefficient function in AAC.

Chapter 5

Creep mechanisms of alkali-activated pastes

5.1 Introduction

Over the past few decades, numerous studies have focused on the origin of creep in concrete (see Chapter 2). A previously proposed creep theory, namely the microprestress-solidification (MPS) theory, suggests that creep behaviour in ordinary Portland cement (OPC) concrete is due to the viscoelastic properties of the paste. Creep deformation itself occurs through several mechanisms. Among suggested creep mechanisms, the dominant ones are sliding of the C-S-H layers over each other and reduction of microprestress over time through breakage of atomic bonds, impacting the viscoelasticity of the material [92, 179, 180]. These mechanisms work in parallel. According to the solidification theory, the decrease of the creep rate over time [181] is attributed to the evolution of the material's microstructure, namely, filling of the pores by an increasing volume fraction of solid reaction products [182, 183], which is accompanied by an evolution of the material properties.

In general, the creep behaviour in AAC can be explained in the same way as that of OPC concrete. However, a straightforward application of the MPS theory to AAC does not seem justified, since the reaction products and microstructure of PC and alkali-activated pastes differ. The reaction products in alkali-activated pastes largely depend on the type and ratio of precursors. As discussed in previous chapters, the creep and mechanical properties of AAC are affected by the slag-to-fly ash ratio in the concrete mixture. This was found for AAC samples cured under both sealed and moist conditions. However, the exact reason for the dependency of the mechanical properties on the precursor ratio requires further investigation.

Understanding the evolution of material structure and mechanical properties at the paste level is essential for understanding the mechanism of concrete creep. Therefore, evaluation of the material nanostructure and nanoscale mechanical properties of the pastes, such as modulus of elasticity, of different ages is needed.

The aim of this chapter is to conduct exploratory research of the evolution of material structure and nanoscale elastic modulus of the paste specimens with various FA/BFS ratios, in order to trace specific creep mechanisms in the alkali-activated pastes. To this end, nanoindentation, N_2 adsorption and XRD tests were conducted to study the nanostructure and nanoscale elastic modulus of alkali activated pastes.

5.2 Materials and methods

5.2.1 Materials

The materials and mixture composition of AAC paste samples considered in this study have been mentioned in the Chapter 3. Additionally, XRD tests were performed on mixture S30 with a slag-to-fly ash ratio of 30:70. The chemical compositions of BFS and FA were already shown in Chapter 3 (Table 3.1). A summary of all the mixture compositions is shown in Table 5.1. Note that no aggregates were added to the mixtures.

Table 5.1 Mixture compositions of AAM pastes for nanoindentation and XRD tests

Components	unit	Mixtures			
		S100	S70	S50	S30
Slag	kg/m^3	400	280	200	120
Fly ash	kg/m^3	--	120	200	280
Activator (Na$_2$SiO$_3$+NaOH)	kg/m^3	200	200	200	200
Liquid/binder (l/b) ratio	kg/m^3	0.5	0.5	0.5	0.5

Paste samples for the tests were cast in plastic moulds. The samples were kept sealed at temperature of 21±2 °C for at least 28 days until the tests were performed. After 28 days the specimens were demoulded. The storage conditions and the timeline are illustrated in Figure 5.1.
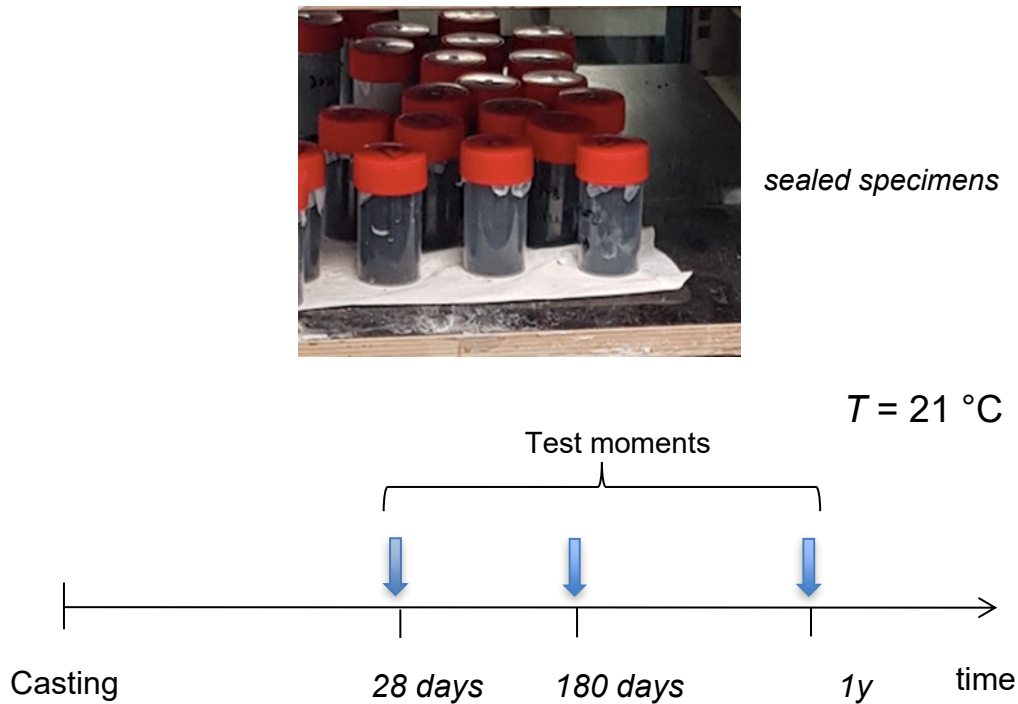
Figure 5.1. The photo of the alkali-activated paste samples casted in plastic moulds and kept sealed at temperature of 21±2 °C (top) and the timeline of the tests (bottom).

5.2.2 Methods

5.2.2.1 X-ray diffraction (XRD)

XRD tests were conducted to study the nanostructure of alkali activated pastes with the aim to trace possible correlations between creep phenomena and nanoscale properties. The crystalline phases in the pastes were identified by X-ray diffraction (XRD) measurements using a Bruker D8 Advanced diffractometer of Bragg-Brentano geometry and Lynxeye position sensitive detector with Cu Kα radiation, scatter screen height 5 mm, tube setting 45 kV and 40 mA. The diffractometer employed coupled θ-2θ scan technique in the range 6° - 110° and step size 0.030 ° 2θ.

The paste samples for XRD tests were prepared in the similar way as for N_2 adsorption tests, which will be described in Section 5.2.2.3. Additionally, the pieces were finely ground and dried before testing.

5.2.2.2 Nanoindentation

Nanoindentation is a widely used technique to test the micromechanical properties of cementitious and alkali-activated materials [184-187]. The nanoindentation technique enables characterization of intrinsic mechanical properties on the micro- and nanoscale. Nanoindentation tests were conducted using Agilent Nano Indenter G200, equipped with a Berkovich indenter. The goal of the tests was to determine the elastic modulus (E) of

different phases of AAM pastes, i.e. C-S-H, C-A-S-H and C-N-A-S-H gels and un-reacted particles.

Nanoindentation testing involves indenting a specimen surface with a solid diamond indenter while recording the penetration depth. Typical load-time and load-penetration diagrams are shown in Figure 5.2. In this study nanoindentation was employed to examine the distribution of the elastic modulus over the specimen surface. In order to get a good picture of this distribution, tests were carried out in a series of grids of $15 \times 15 = 225$ imprints, each covering an area of 300 μm × 300 μm.
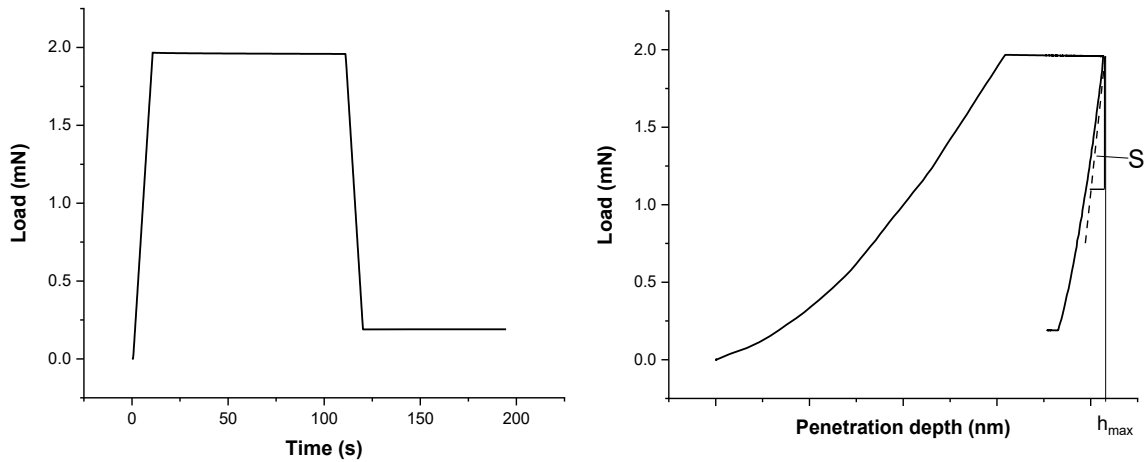
Figure 5.2. The load-time (left) and load-penetration (right) diagrams for a single penetration during the nanoindentations test.

Prior to nanoindentation, the samples were cut into slices of about 20×20×10 mm^3, grinded and polished to achieve an absolutely smooth surface. For the grinding, sandpapers of 180, 240, 400, 600 and 800 and 1200 grit were used in series during 5-10 minutes each. Instead of water, ethanol was used as a cooling lubrication liquid to prevent further reaction of the paste components. After grinding, the samples were polished on a lapping table with diamond paste (6 μm, 3 μm, 1 μm, and 0.25 μm). Sample preparation was performed just prior to testing to avoid carbonation of the surface to be tested.

The tests were conducted under load-controlled mode. During the tests the load was linearly increased until it reached a specified maximum value 2mN. When the maximum level was reached, the load level was held constant for 180 seconds to reach related maximum penetration depth h_{max}, and then the sample was linearly unloaded (see Figure 5.2, left).

A standard procedure to analyse the nanoindentation data was proposed by Oliver and Pharr [188]. It uses the specimen's response during unloading, - assumed to be purely elastic -, to calculate the tip–sample contact size at the onset of unloading. This method is based on Hertz' theory for elastic contact, which states that the stiffness S_c of the contact

between two elastic spheres should be evaluated as the initial slope of the unloading curve (see Figure 5.2), and E_r is the effective elastic modulus of the two spheres.

S and E_r are given by Eq. 5.1 and Eq. 5.2, where P_c is contact force, h is relative movement of the centres of the spheres, $h = h_{max}$ is the maximum penetration depth, and A_c is the contact area at the maximum depth h_{max}.

$$S_c = \frac{dP_c}{dh} = \frac{2}{\sqrt{\pi}} = E_r\sqrt{A_c} \tag{5.1}$$

$$E_r = \frac{2}{\sqrt{\pi A_c}} \tag{5.2}$$

The effect of non-rigidity of the indenter can be accounted for by the equation:

$$\frac{1}{E_r} = \frac{(1-v)^2}{E} + \frac{(1-v_i)^2}{E_i} \tag{5.3}$$

where E and v are the elastic modulus and Poisson's ratio of the tested material, respectively. In this study, the Poisson's ratio v of the tested material was assumed to be 0.2. E_i and v_i are the elastic properties of the diamond indenter: $E_i = 1141$ GPa, $v_i = 0.07$.

5.2.2.3 N_2 adsorption

The pore structure plays an important role in water transport and dramatically affects shrinkage and creep properties of a concrete binder [88, 96, 181]. Capillary pores (10 nm – 10 μm) contain adsorbed water that plays an important role in drying shrinkage and creep, as mentioned in Chapter 2 (Section 2.4.2.2) [189]. The micropores (< 2 nm) are specifically associated with the gel phase, which are the reaction products of cementitious materials. With the nitrogen (N_2) adsorption method the pore size distribution in the paste is determined, considering a wide range of pore sizes, reaching as low as 2 nm.

Inspired by the research of Brunauer, Emmett and Teller [190] on the interaction between gases and the surface of solids, nitrogen adsorption-desorption isotherms are widely used to determine the specific surface area of pastes and its pore sizes distribution. The schematic illustration of the nitrogen (N_2) adsorption/desorption procedure is shown in the Figure 5.3. The interpretation of the N_2 isotherms is based on Brunauer-Emmet-Teller (BET) [190] and Barret–Joyner–Halenda (BJH) models [190].
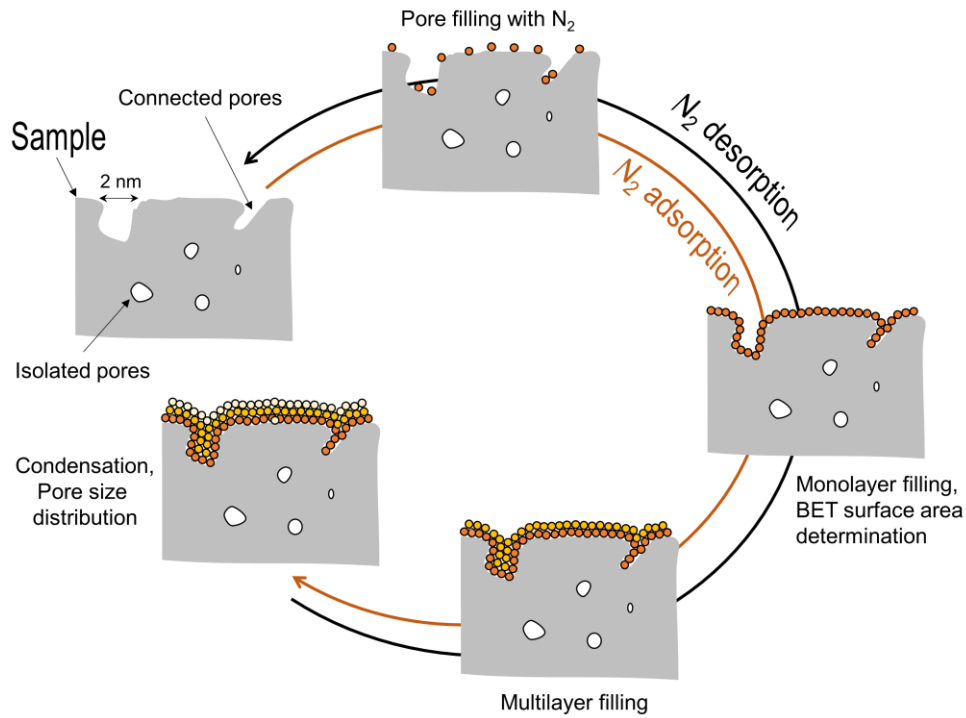
Figure 5.3 Illustration of the interaction between gases and the surface of solids during the N_2 adsorption tests. The scheme demonstrate the adsorption and desorption processes during the test. Captured from [15].

Based on the BET theory the following equation hold (its derivation is explained in [190, 191]):

$$\frac{P}{V_a(P_0-P)} = \frac{1}{V_m C} + \frac{M-1}{V_m C}\left(\frac{P}{P_0}\right) \tag{5.4}$$

where P is the equilibrium gas (N_2) pressure, P_o is the saturation pressure of the gas (N_2), V_a is the amount of gas (N_2) adsorbed at pressure P, M is a constant and V_m is the amount of gas (N_2) needed to cover the surface with a monolayer of gas (N_2) molecules.

Then the specific surface area can be determined by:

$$S_{BET} = \frac{N_A V_m A_N}{V_0} \tag{5.5}$$

where N_A is the Avogadro constant, A_N is the surface area occupied by a single adsorbed gas molecule and V_o is the molar volume of gas. A_N of nitrogen is assumed equal 16.2×10^{-20} m^2.

The BJH model provides information about the pore size distribution of porous materials. The distribution can be calculated using a desorption isotherm according to the modified Kelvin equation (5.6), which provides a correlation between pore diameter and pore condensation pressure, assuming the cylindrical pore shape.

$$ln\left(\frac{P}{P_0}\right) = \frac{-2YV_0\cos\theta}{RT(r_p - t_c)} \tag{5.6}$$

where P/P_0 is the relative gas pressure, Y is the surface tension of liquid nitrogen, V_o is the molar volume of the liquid, θ is the contact angle between liquid and pore wall (θ=0 for completely filled pore), R is the gas constant, r_p is the pore radius of the largest filled pore and t_c is the thickness of the water layer adsorbed at the surface of the solid.

The porosity of pores in the mesopore range measured by nitrogen adsorption gives similar results to those measured by often used mercury intrusion porosimetry (MIP) tests [191, 192].

To perform the adsorption test, the paste samples were gently crushed into pieces of 1 mm³ and bathed in isopropanol for one week, to replace the water in the pores by alcohol. Then, the samples were placed under vacuum at 25 °C for at least four weeks. Afterwards, about 1-1.5 gram of material was used for the analysis.

The N_2 adsorption tests were conducted using Gemini VII 2390 with a relative gas pressure(P/P_0) ranging from 0.05 to 0.99 and a constant temperature of 77K. The relative pressure is defined as equilibrium vapour pressure normalized by the saturation vapour pressure. The temperature was set by cooling using liquid nitrogen.

5.3   Results and discussion

5.3.1 XRD of AAM pastes

The crystalline phases and chemical bonding of the paste samples were evaluated using XRD technique. The results of the tests are shown in the Figures 5.4.

A large portion of the material was amorphous or microcrystalline. Therefore, not all small peaks of the XRD analysis could be identified. The identified peaks for the tests of different ages were identical; therefore, we conclude that the crystalline phases did not change with time. Additionally, it can be assumed that the microstructure of the reaction products formed after 28 days was amorphous and could, therefore, be observed by growing halo in the XRD test curves for specimens tested in mature age.

The main compound in S100 was C-S-H (calcium silicate hydrate $Ca_{1.5}SiO_{3.5}\cdot xH_2O$). Note, that C-S-H is not commonly accepted as a crystalline phase. However, we can identify several distinct peaks in the curves, which are characteristic of crystallites. Blending slag with FA changed the reaction products and, therefore, the amount of the peaks. The replacement of slag with FA in mixtures S70, S50, S30 led to an observable increase of Quartz (SiO_2) and Mullite ($3Al_2O_3\cdot 2SiO_2$) phases alongside the C-S-H ($Ca_{1.5}SiO_{3.5}\cdot xH_2O$). The presence of these additional phases might contribute to densification or altered pore structure within the paste, impacting the paste's mechanical properties and long-term durability due to the distinct characteristics of Quartz and Mullite compared to the C-S-H compound.
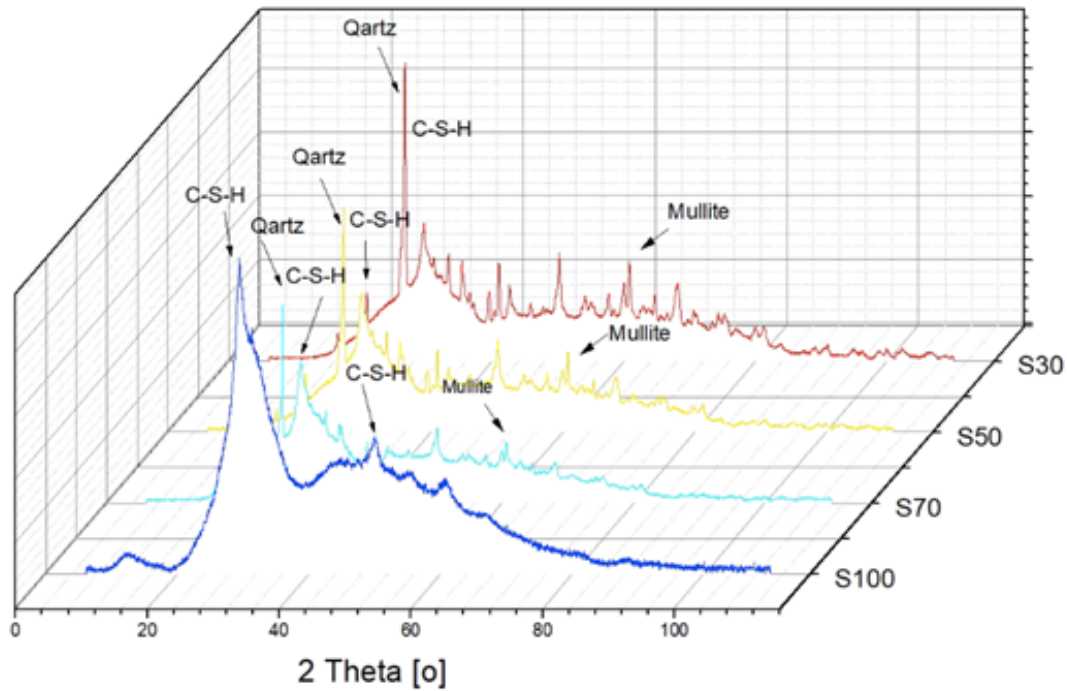
Figure 5.4 XRD results for S100, S70, S50 and S30 mixtures at age 28 days (the curves of different ages turned out to be identical peaks).

5.3.2 Nanoindentation

Many studies have shown the importance of microscale mechanisms on the long-term creep behaviour of concrete. Nanoindentation is a promising technique to examine the nanoscale elastic properties of the paste and their correlation with the viscoelastic properties of concrete at the macroscale.

The ESEM (environmental scanning electron microscope) photos (Figure 5.5) of the surfaces show the locations of nanoindentation tests. The maps of the elastic moduli of mixtures S100 and S50 at the age of 28 and 365 days are given in Figure 5.7. From these maps, the effect of the precursor ratio and age of the samples on the elastic modulus of alkali-activated pastes can be read directly.

The E-modulus of the tested pastes after 365 days of curing varied between 5 and 85 GPa. Based on nanoindentation results we can identify components with different stiffness (Figure 5.6). However, for our research, it is easier to disregard the inhomogeneous structure and work with an average (from 400 imprints) E-modulus of the paste. Note, that the points related to the unreacted products were excluded from the data set (Figure 5.7).

The mean value of the elastic modulus of 28 days old S50 paste was 22.7 GPa, which is 8% lower than that of S100 paste (24.7 GPa). The average value of the elastic modulus for

both mixtures increased with time. At the age of 365 days the difference of the values was 16.8%, viz. 23.2 GPa and 27.9 GPa for S50 and S100 pastes, respectively.
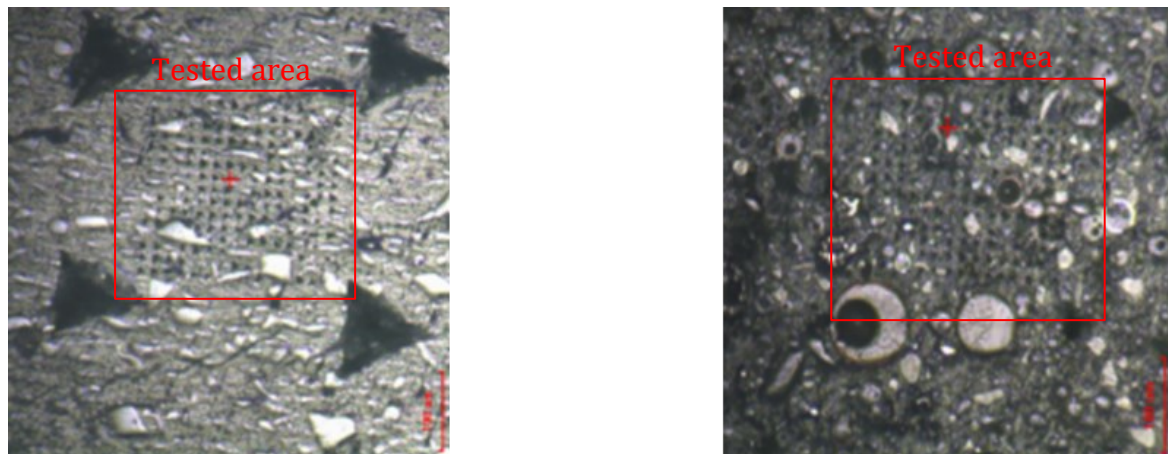
Figure 5.5. Environmental scanning electron microscope (ESEM) picture of indented paste surface of 28 days old samples of alkali-activated pastes.
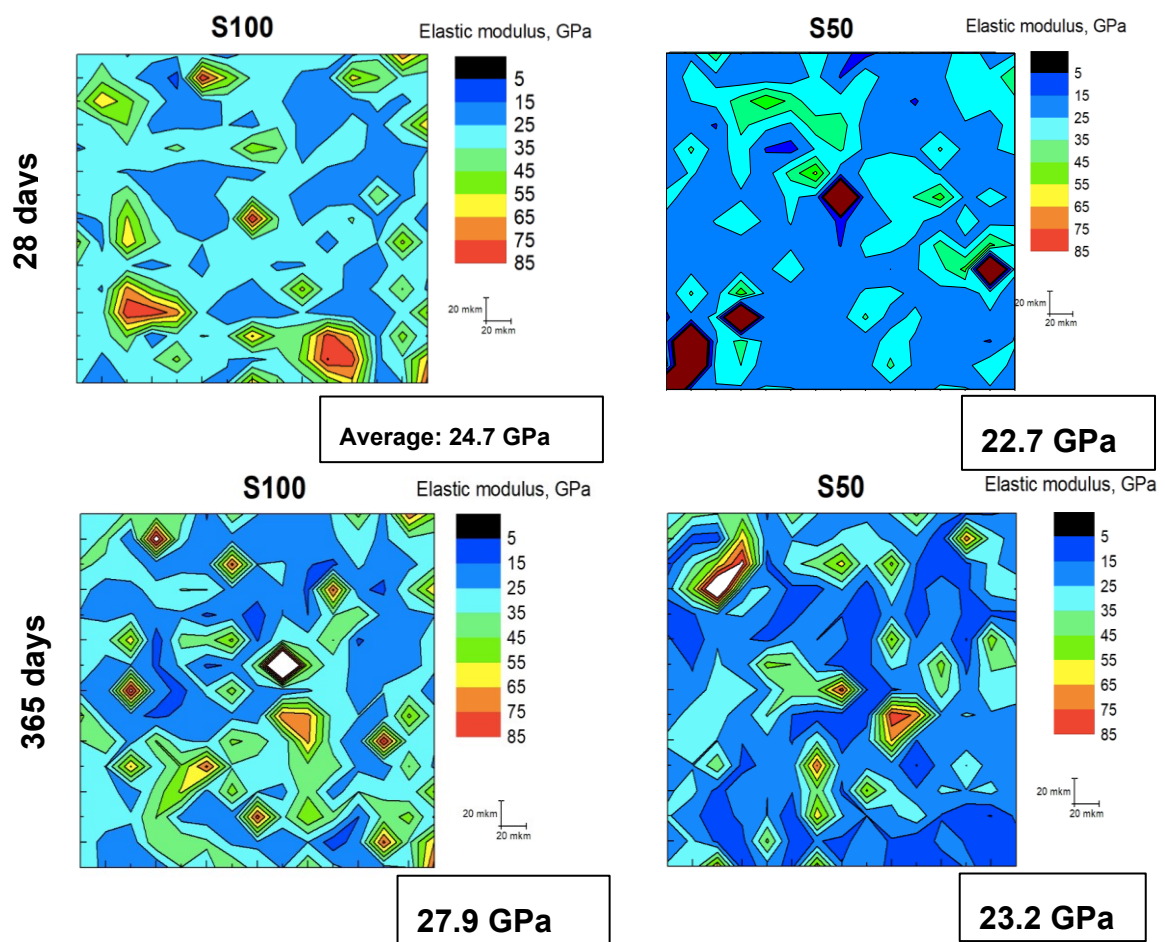
Figure 5.6 Nanoindentation results (elastic modulus) for S100 and S50 pastes in the ages 28 days and 1 year.

The values of the modulus of elasticity of 28 days old alkali-activated GGBFS and FA were in agreement with those reported by Nedeljkovic [15] and Ma [186]. Those authors found an E-modulus of about 30 GPa for slag-based material [15], and in the range between ~11 and ~23 GPa for FA-based pastes [186]. Constantinides and Ulm [193, 194] measured the elastic modulus of the pastes based on Type I [193] and white Portland cement with a low aluminates concentration [194], and liquid-binder ratio 0.5. Typical values for the elastic modulus of the main hydration reaction product of cement, i.e. C-S-H, are ~18.2-21.7 GPa for low-density (LD) and ~29.1-29.4 GPa for high-density (HD) gel, respectively.
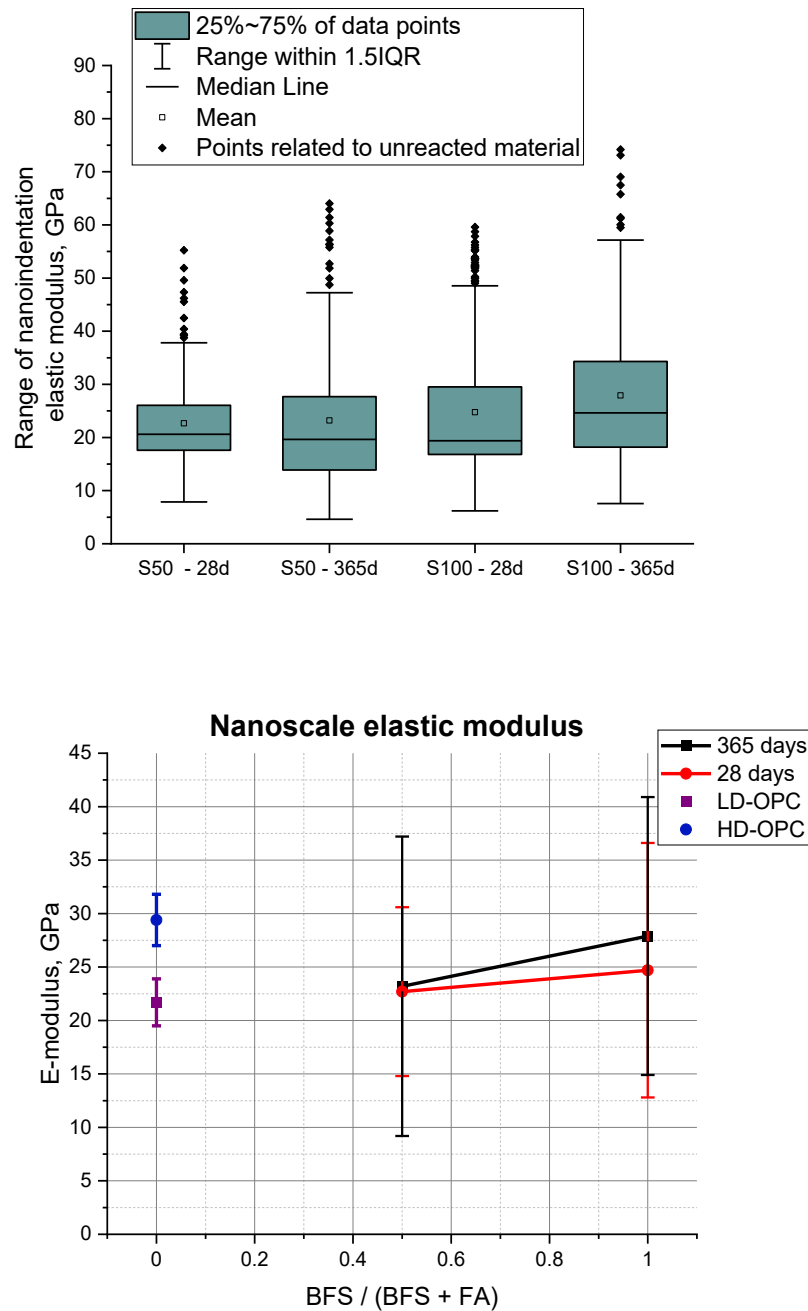
Figure 5.7 Nanoscale elastic modulus of S100, S50 pastes and HD- and LD- C-S-H gels [193, 194] in the ages 28 days and 1 year.

5.3.2 Nitrogen adsorption test

5.3.2.1 BET surface area

The N_2 gas adsorption test was performed to characterize the pore structure and specific surface area of the paste. The BET specific surface area of the mixtures was calculated using to equation (5.5) [190]. Table 5.2 shows the specific surface area of 28 and 365 days

Table 5.2. BET specific surface area of AAM pastes (m²/g)

Time of testing	Specific surface area [m² /g] of AAM pastes			
	S100	S70	S50	S30
28 days	5.1	19.4	25.7	33.7
365 days	0.78	0.89	1.6	2.6
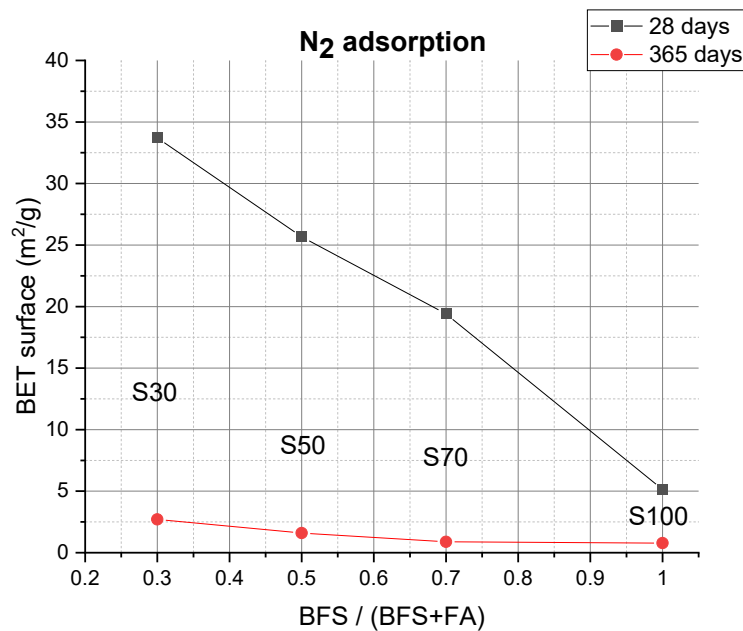
Figure 5.8 Measured BET specific surface area of AAM pastes (m²/g) vs. the precursors'
composition at 28 days and 365 days.

old pastes. The measured BET surface areas presented as function of the BFS/FA ratio of the precursor are shown in Figure 5.8.

To put the data of Table 5.2 in perspective: typical BET specific surface area of the cement paste after 28 days is 56.7 to 139.6 m²/g, depending on the water-to-cement ratio (97.7 m²/g for w/c=0.5) [195, 196]. The specific surface area of alkali-activated pastes, with l/b ratio 0.5, depends on the precursor composition, i.e. (BFS-FA)/BFS. Mixing slag with fly

ash at 50% increased the specific surface area of 28 days old paste by a factor five, from 5.13 m²/g for S100 to 25.67 m²/g for S50.

In general, increase of the amount of gel during the reaction process leads to an increase of the BET surface of the gel pores. In our study a dramatic decrease of the BET surface area for alkali-activated pastes with time was observed. For S100 the decrease was more than ~650% (i.e. from 5.1 to 0.78 m²/g), for S50 it was ~1600% (i.e. from 25.7 to 1.6 m²/g) (Table 5.2). This decrease of the BET surface area with time indicates that this decrease is due to capillary pores (gel pores are disregarded).

5.3.2.2 Pore size distribution

The (cumulative) pore size distributions of 28 and 365 days old pastes are shown in Figure 5.9, while the critical pore sizes are listed in Table 5.3. It should be noted that nitrogen adsorption can only provide information about the pore structure of capillary pores (2–100 nm in this study). The pore volume of AAM pastes decreases with time, while the amount of pores smaller than 150 nm increases. Refinement of the nanostructure is the result of alkali activation reaction and increase of product volume, which affects the viscoelastic properties of the paste.

Table 5.3. Critical pore size (nm) of AAM pastes, measured at age of the paste of 28 and 365 days.

Time of	Critical pore size [nm] of AAM pastes			
testing	S100	S70	S50	S30
28 days	6.03	6.84	7.19	9.19
365 days	2.34	2.5	2.56	4.1
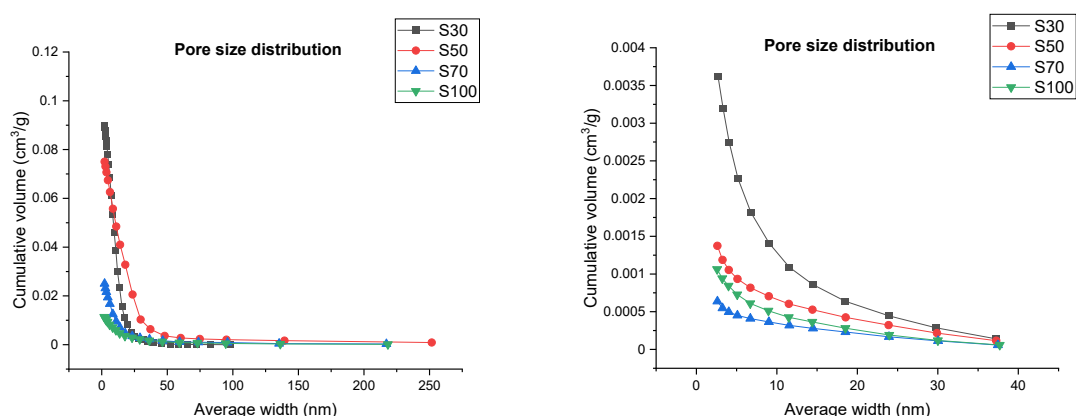
Figure 5.9 Pore size distributions at the age of 28 days(left) and 365 days(right). (Note: horizontal axis have different scales)

5.3.3 Mechanical strength vs. porosity

The strength of a cementitious material is determined by the 'intrinsic' strength of the reaction products and the porosity of the sample [197]. According to this concept, a cement paste reveals its 'intrinsic' strength [198] when there is no porosity at all.

The relationship between strength and porosity of a cementitious material can be presented by both exponential and logarithmic expressions. An empirical exponential relationship was originally proposed by Ryshkewitch [199], and later further developed by Soroka and Sereda [200]. Schiller [201] has presented a fundamental study and proved that within the practical range of capillary porosity, these expressions lead to almost the same results.

The aforementioned exponential and logarithmic expressions are:

$$f = f_{01} \cdot e^{-bp} \tag{5.8}$$

$$f = B \cdot \ln\left(\frac{p_0}{p}\right) \tag{5.9}$$

where f and p are strength and porosity of the material, respectively, f_{01} is the strength of the theoretical (intrinsic) non-porous material. b and B are constants, and p_0 is the hypothetical value of capillary porosity (without considering gel pores <2 nm) at which the strength practically vanishes.

Figure 5.10 shows a plot of compressive strength vs. porosity of the alkali-activated pastes [15]. The results were approximated with expressions (5.8) and (5.9). Rössler et al. [202] performed experiments with a single industrial Portland cement and found the intrinsic strength f_0 and the value of porosity p_0 for OPC paste are 636 MPa and 31%, respectively. It is emphasized again that only capillary porosity is considered, while the gel pores are not taken into account. The value of f_{01} for alkali-activated pastes, irrespective of the precursor composition, was 123.5 MPa, which is much lower than the 636 MPa found for OPC paste (Figure 5.10). According to the curve fit procedure the value of p_0 would be 159.2% (legend in the Figure 5.10). A porosity p_0 exceeding 100% is not possible and without physical meaning. Actually, the analytical curve-fitted strength-porosity equations give reasonable strength predictions for a capillary porosity up to 30%.
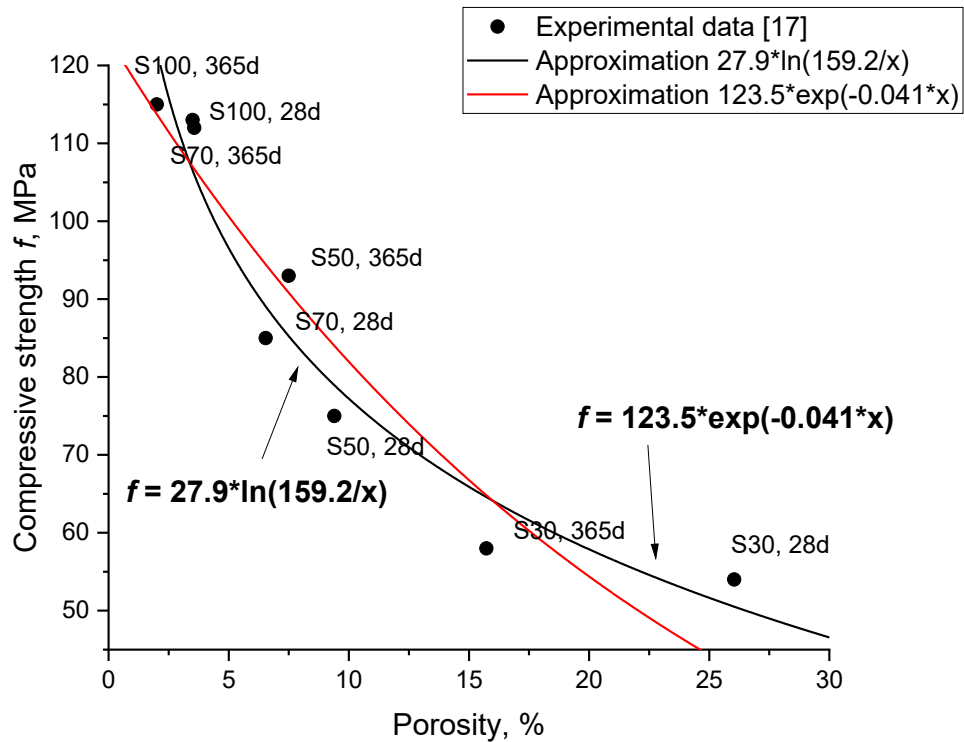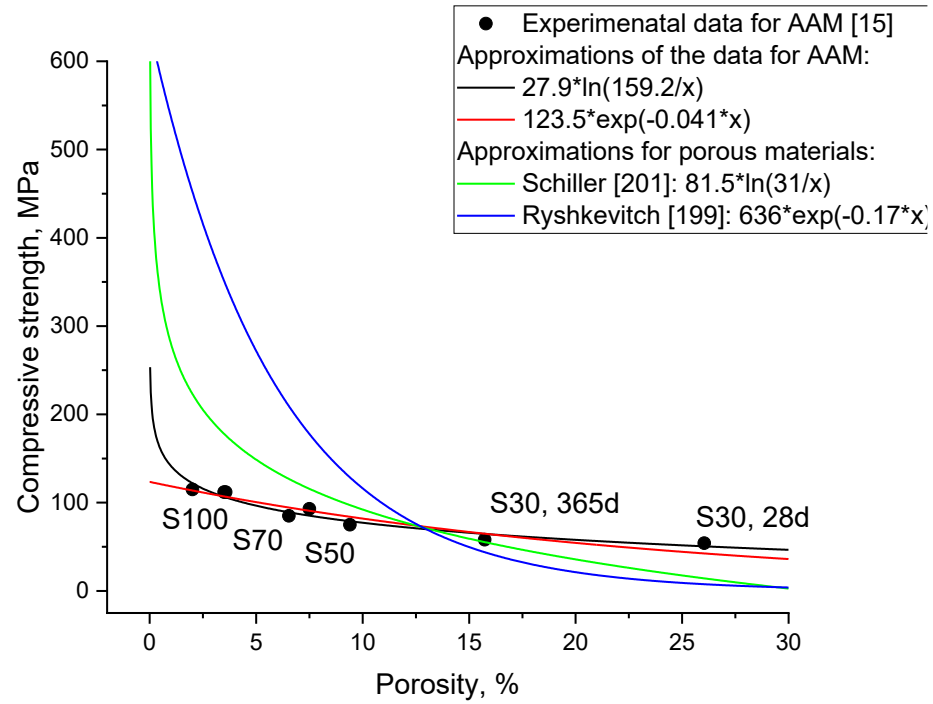
Figure 5.10 Compressive strength vs capillary porosity of the alkali-activated and hydrated cement pastes. Experimental results were approximated with expressions (5.8) and (5.9) from [199, 201].

5.3.4 Discussion

XRD test results suggested that the nature of alkali-activated pastes was microcrystalline and amorphous up to the age of 365 days. Therefore, alkali-activated pastes can be classified as 'colloidal gels'. The microstructure of these gels results from the attraction of colloidal particles dispersed in a liquid, forming a loose network. Creep mechanisms in amorphous solids, and in particular colloidal gels, have been extensively discussed in scientific publications [114, 203-208]. However, the description remains controversial because of the high sensitivity to the volume fraction of colloidal particles and to the interparticle interactions [114]. If the volume fraction of particles is low, the creep response of the paste can be described by its linear viscoelastic properties [114, 205]. However, in granular materials with a high particle volume fraction, creep is often attributed to plastic rearrangements that disrupt the interactions and forces between particles [209, 210]. The specific mechanisms of creep in systems with high packing density with insufficient available space for local reorganization of the grain network are not fully understood. In such systems, creep is often associated with slow, gradual and time-dependent deformation due to the inability of particles to readily rearrange and redistribute stress within the densely packed network [211, 212].

Assuming that the creep behaviour of AAC is a consequence of the viscoelastic properties of the binder [10, 18], the evolution of creep coefficient of AAC correlate with the viscoelastic properties and packing density of the alkali-activated binder. The characterization of the pore structure of binder provides valuable insights into the mechanical properties of the material. The curve-fitted relationships of compressive strength and total porosity of the alkali-activated pastes suggest a much lower 'intrinsic' strength (f_{01}) of AAC than of OPC paste. Manipulating the parameters of mixture design has the potential to significantly influence f_{01} of the material. However, further comprehensive research is warranted to elucidate the precise mechanisms underlying these effects.

The creep behaviour of AAC can also be attributed to rearrangements of particles within the microstructure. Creep then becomes a complex process of stress-induced local shear transformation (including gel layers sliding) and atomic diffusion [213, 214]. When these processes are considered together, the experimentally observed evolution of strain and properties at the nanoscale can be assumed as the ultimate result of solid particle diffusion and collective atomic rearrangements (Figure 5.11). The dominant mechanism of that deformation may vary depending on the magnitude of the load and specific properties of the molecular interactions [114].

a. Shear mode deformation   *b. evolution of defect*
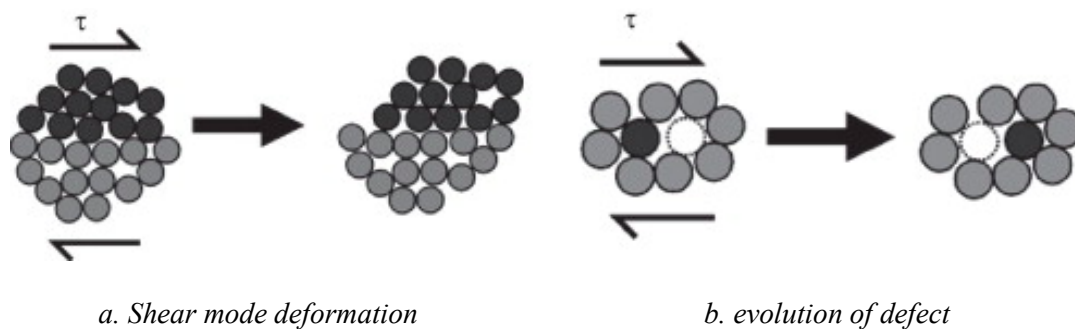
Figure 5.11 Two-dimensional representation of shear transformation (a) and local defect diffusion (b). The circles can represent colloidal particles at the microscale or individual atoms at the molecular scale [47].

In our alkali-activated systems the replacement of BFS by FA changed the solution chemistry during the activation reaction, resulting in a highly connected depolymerized tobermorite-like structure of the gel [215, 216]. This can potentially result in a distinct redistribution of stress within the molecular structure of the gel, leading to noticeable differences in strain.

In a tobermorite-like structure not only molecular forces, but also electrostatic forces and van der Waals forces bind the layers of the gel. The combined effects of the different forces stabilise the layered structure, increasing the bridging distance between building blocks. In this case, although the cohesive intralayer binding is strong, the colloidal interactions are significantly lower, making sliding easier. In addition, the higher amount of free water in the structure of alkali-activated products also affects the evolution of the creep strain [211, 217]. Consequently, the deformation capacity of the interparticle bridges may increase.

These hypotheses about the contribution of molecular-scale mechanisms to creep are hard to validate experimentally. In-situ monitoring of atomic movements during creep using experimental methods is hard to perform. However, molecular dynamic (MD) simulations can be used for molecular-scale simulations of creep mechanisms. MD simulations of creep in C-S-H and C(-A)-S-H gels will be dealt in Chapter 6.

5.4 Observations and conclusions

1. XRD analysis showed that the crystalline phases of the tested alkali-activated materials were stable over time. Meanwhile, the results of nanoindentation and N_2 adsorption tests indicated the evolution of the microstructure and the presence of new material filling the pores. Based on these findings, it can be inferred that the new material has an amorphous structure.

2. The nanoindentation tests have shown that the nanoscale elastic modulus of alkali-activated pastes depends on the precursor composition. The average values of the elastic modulus of slag-based S100 and 50% fly ash-blended S50 paste after 28

days were 24.7 GPa and 22.7 GPa, respectively. For both mixtures, the average magnitude of the elastic modulus increased with time. After 365 days the elastic modulus of S100 and S50 were 27.9 GPa and 23.2 GPa, respectively.

3. Nitrogen adsorption tests have shown that blending slag with fly ash resulted in a material with higher porosity. It also affected the pore size distribution and maximum pore size. The overall pore volume decreased with time and an increase of pores smaller than 150 Å was observed. Nonetheless, the typical approximation, accepted for porous materials, of the relationship between compressive strength and total porosity (excluding gel pores) [199, 201], has demonstrated a noticeably lower intrinsic strength f_{01} compared to that of the OPC paste. Hence, further research is imperative to understand the underlying factors contributing to the disparities in viscoelastic properties between AAC and OPC concrete.

4. The creep mechanisms in alkali-activated pastes can be considered as a complex process of stress-induced local shear transformation and atomic diffusion. The replacement of BFS with FA in the mixture alters the nanoscale material structure and molecular-scale interactions, which affect the viscoelastic properties of the alkali-activated paste. The molecular-scale effects are hard to investigate experimentally; therefore, in the next chapter, computational tools will be used to perform simulations of molecular-scale creep of the gel (reaction products).

Chapter 6

Molecular dynamic simulations of creep of C(-A)-S-H gel.

6.1 Introduction

The mechanism of creep in concrete is still subject of many debates, as we discussed in previous chapters. It is generally agreed that on the nanoscale concrete creep originates from the complex viscoelastic behaviour of reaction products in the binder: calcium–silicate–hydrate (C-S-H) gel for hydrated OPC and calcium aluminium silicate hydrates (C-A-S-H) gel for alkali activated slag [133, 210, 211]. However, the precise molecular-scale mechanism of creep remains not completely understood yet. At this time, hypotheses about the reconfiguration of fundamental building blocks in the reaction products need to be further substantiated and validated. Certainly, molecular-scale creep mechanisms in C-S-H and C-A-S-H gels exhibit different visco-elastic properties due to their distinctive chemical compositions and molecular structures. The C-S-H gel has a precisely studied crystalline tobermorite structure, in contrast to the aluminium-containing, relatively amorphous, polymeric arrangement of the C-A-S-H gel. These differences significantly influence the mechanical characteristics and dynamic response under external loads.

Molecular dynamics (MD) serve as a widely used computational tool for investigating processes at the molecular scale [218]. MD simulations are a computational methodology used to mimic the actions of atoms and molecules over time by numerically solving the equations of motion of the particles in the system. These simulations provide deep insights into the dynamic behaviour, thermodynamics and properties of molecular systems. In essence, atomistic simulations aim to numerically unravel and replicate the trajectory of each individual atom within the material's framework. Consequently, MD

bridges the gap between molecular-scale motions and the collective behaviour of atoms - essentially, the evolution of nanostructure and, thereby, nanoscale mechanical properties. In particular, a sequence of loading-unloading shear stress cycles – via an incremental stress-marching technique - can effectively mimic time-dependent material responses, i.e. creep [211].

In this chapter MD simulations will be performed using the incremental stress-marching technique to investigate creep behaviour of C-S-H and C-A-S-H gels on the nanoscale. This study aims to evaluate the influence of the parameters of a C-A-S-H gel structure on the creep strain development. Specifically, the variations of silicate chain length, the aluminium-to-silicon (Al/Si) ratio, and the amount of interlayer water on creep will be investigated to validate the hypothesis on nanoscale creep mechanisms formulated in Chapter 5.

6.2   Methods

6.2.1   Molecular structure

The first step of MD simulations is to create a realistic molecular structure with representative interatomic interactions that mimics the measured properties of the material [219]. The smallest volume of a molecular structure that shows the three-dimensional pattern of the entire system is called a unit cell. In the simulation process, periodic boundary conditions (PBC) were applied in order to approximate an infinite system.

The main reaction product of cement hydration is C-S-H gel. C-S-H exhibits some degree of crystallinity, as shown by X-ray diffraction methods [218]. The atomic arrangement of a C-S-H structure resembles the naturally existing tobermorite mineral [220]. This material has a layered structure, in which calcium silicate layers are separated by interlayer space. Tobermorite has a chemical formula $Ca_5Si_6O_{16}(OH)_2 \bullet 7H_2O$ and is characterized by a basal[2] space (Figure 6.1). Alkaline activation of BFS with sodium hydroxide (NaOH) and water glass results into modifications of the C-S-H and C(-A)-S-H gels, which also have the structure of tobermorite [117], but may show lower crystallinity and contain additional aluminium atoms.

The constructed C-(A-)-S-H systems are shown schematically in Figures 6.1 and 6.2. C-(A-)-S-H structures were created by modifying the structure of a model of tobermorite mineral with a basal spacing equal 1.4 nm (tobermorite-14Å) described by Bonaccorsi et al. [220], following the procedure described by Pellenq et al. [221] and refined by Qomi et al. [222] . The unit cell of this mineral was replicated to obtain a simulation box in defined symmetry group B11b, with dimensions in the x, y and z directions of $0.68 \times 0.15 \times 2.85$ nm^3, respectively, and the unit-cell angle γ = 123.25°. This model contains the material characteristics suggested on the basis of the data from nuclear magnetic resonance (NMR) spectroscopy and infrared (IR) analysis. The structure of tobermorite-14Å consists of long

---

[2] Basal spacing is defined as the interlayer distance including the thickness of a single layer.

layers of CaO polyhedra, with tetrahedral silicate chains on both sides of these layers. The repeating units of silicate tetrahedra form chains of different lengths.

The average number of aluminosilicate tetrahedral in a tobermorite-like chain is called mean chain length (MCL). Yan [223] has shown that the MCL of the C-S-H chains in cement paste significantly depends on the Ca/Si ratio. For the low Ca/Si ratio in C-S-H, i.e. Ca/Si = 0.75±0.05, the MCL is 76±15, for Ca/Si = 0.88±0.03 ratio the MCL is 27±7 and for the high Ca/Si = 1.44±0.02 ratio the MCL is 2.56±0.1. In contrast, C-S-H in the presence of alkali hydroxide with pH about 13, like in slag-based gel, shows MCL of 33.0, 7.44 and 2.64, respectively [223]. The molecular structures of tobermorite for this study were created with the MCL close to these values.

The structure with MCL=∞ (considering periodic boundary conditions) was adopted as a reference (Figure 6.1). Then, every third tetrahedron at the bridging site was removed to get the structure with MCL=5 (Figure 6.2a). Then, every second bridging tetrahedron of the structure with infinite MCL was deleted to get MCL=2 (Figure 6.2b).

The molecular structure of C-A-S-H gel is reminiscent of the structure of C-S-H gel where the Si atoms have been replaced by Al. The most probable positions for substitution Si with Al are the bridging sites (see Figure 6.1). Puertas et al. [117] created a molecular model of C-A-S-H gel. They have shown that the structure of C-A-S-H gel formed in slag-based alkali-activated materials depends on the type of used activator. For the mixture used in our experimental study in Chapters 3-5, the MCL would be about 5. Kapeluszna et al. [224] studied incorporation of Al in C-A-S-H gels with various Ca/Si. They found that low Ca/Si ratio promoted Al incorporation into C-(A)-S-H gel. Typical Al/Si was in the range from 0.05 to 0.2. Also they discovered that Al-bearing gels exhibited higher content of non-evaporable (interlayer) water.
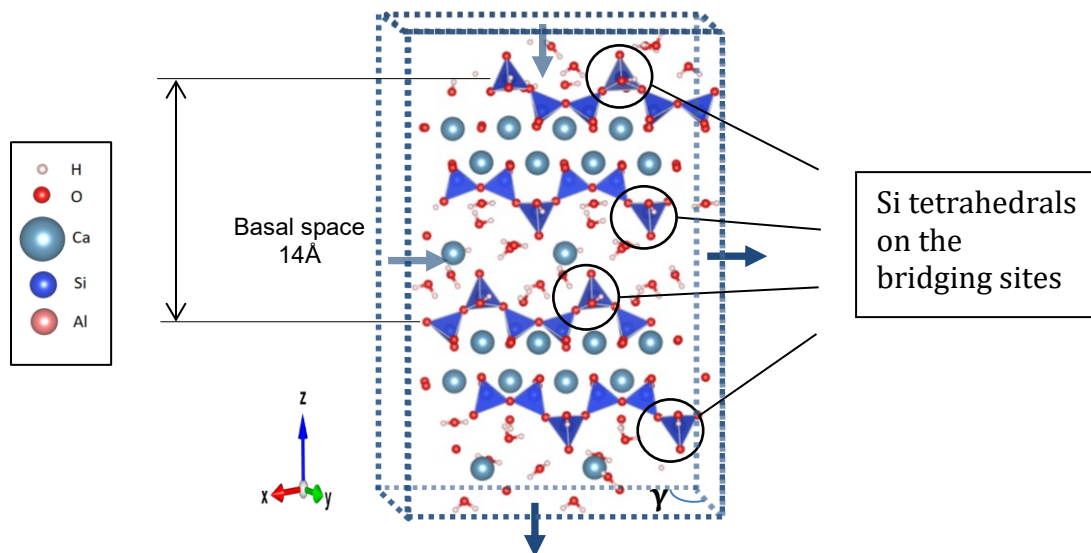
Figure 6.1 Schematic illustration of a C-S-H unit cell: Tobermorite-14Å molecular structure, where MCL=∞ and basal space = 1.4 nm. Periodic boundary conditions are applied.

a. MCL=5

b. MCL=2

c. MCL=5, Al/Si ratio=0.18
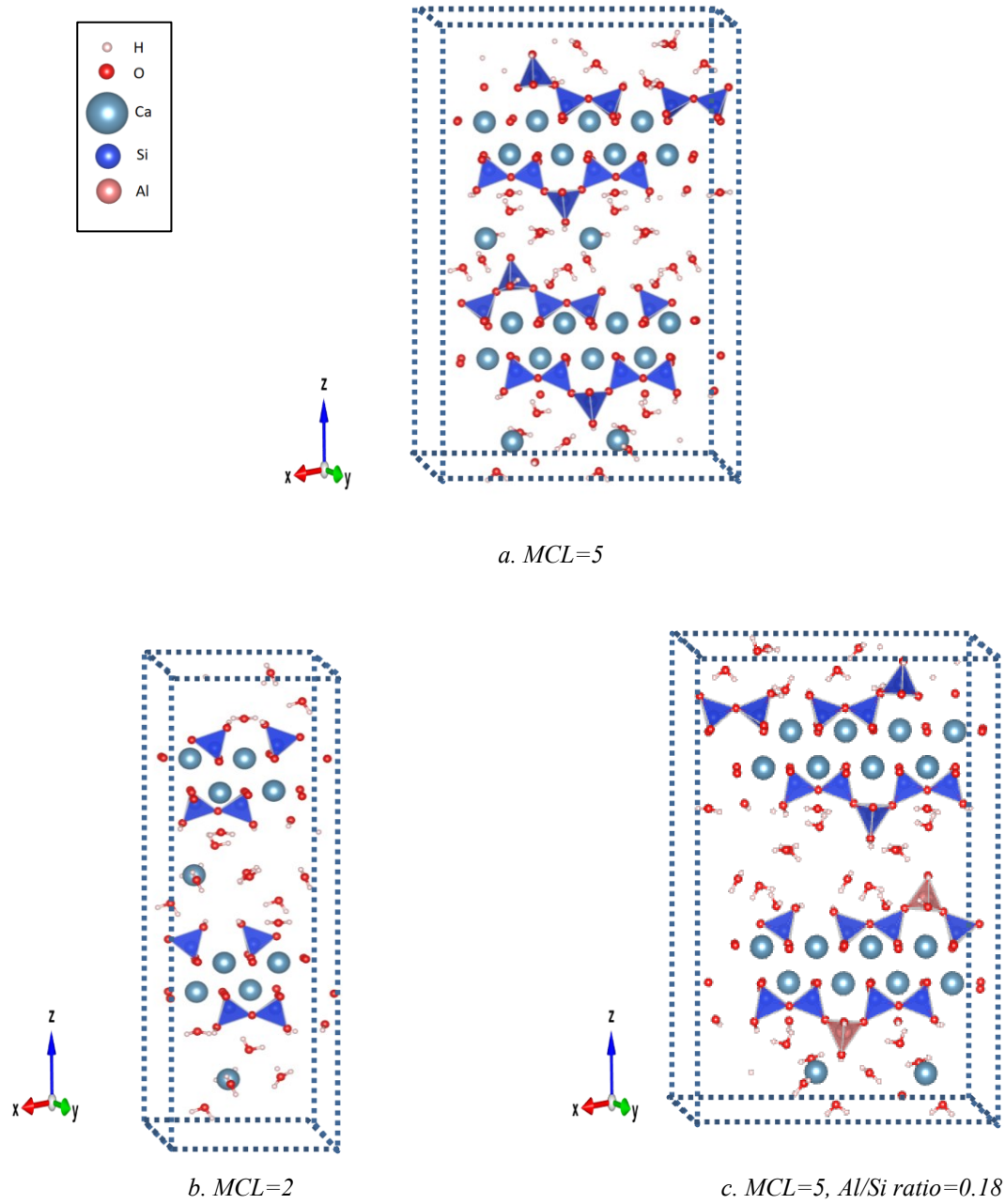
Figure 6.2 Schematic illustration of the unit cell structures of: a. Tobermorite-14Å molecular structure (MCL=5), b. Tobermorite-14Å molecular structure (MCL=2), c. Tobermorite-14Å molecular structure (MCL=5, Al/Si ratio=0.18).

To simulate creep in C-A-S-H gel as close as possible to the gels formed in the mixtures studied in Chapters 3-5 and aforementioned publications [117, 224], the Al/Si ratio of the structure with MCL=5 was varied from 0 to 0.2, replacing Si atoms with Al at the most likely position of the substitution – bridging site (Figure 6.2c). The resulting imbalance in charge was compensated by introducing additional hydrogens. The lattice parameters of the resulting molecular structures are summarized in Table 6.1.

Table 6.1. Calculated mechanical properties of the tested molecular structures.

	Elastic modulus E	Bulk modulus K	Shear modulus G
	GPa	GPa	GPa
MCL = ∞	84.0	56.2	23.4
MCL = 5	79.9	25.1	13.2
MCL = 5 (Al/Si = 0.11)	80.8	25.6	11.3
MCL = 5 (Al/Si = 0.18)	82.3	29.1	14.2
MCL = 5 (Al/Si = 0.25)	83.0	29.9	14.8
MCL=2	43.34	23.97	12.26

The effect of the mean chain length and Al/Si ratio on the creep evolution of C(-A)-S-H gel has not yet been extensively investigated. However, the results of this study are consistent with published results of simulations of the mechanical properties of C-S-H gel [117] and nuclear magnetic resonance (NMR) experiments [225]. The results of the mechanical properties of nanocrystalline calcium aluminosilicate hydrate (C-A-S-H gel) are consistent with the studied of Geng et al. [226] and Wang et al. [227].

The impact of the amount of interlayer water on creep strain development was investigated through modifications of the C(-A)-S-H structure with MCL of 5 and an Al/Si ratio of 0.18. Namely, the number of water molecules within the interlayer spacing of tobermorite structure was varied. Initially, the number of water molecules was doubled to 24 (as shown in Figure 6.3), allowing for comparative analysis. Then all interlayer water molecules were completely removed, resulting in a configuration with no water between the layers.
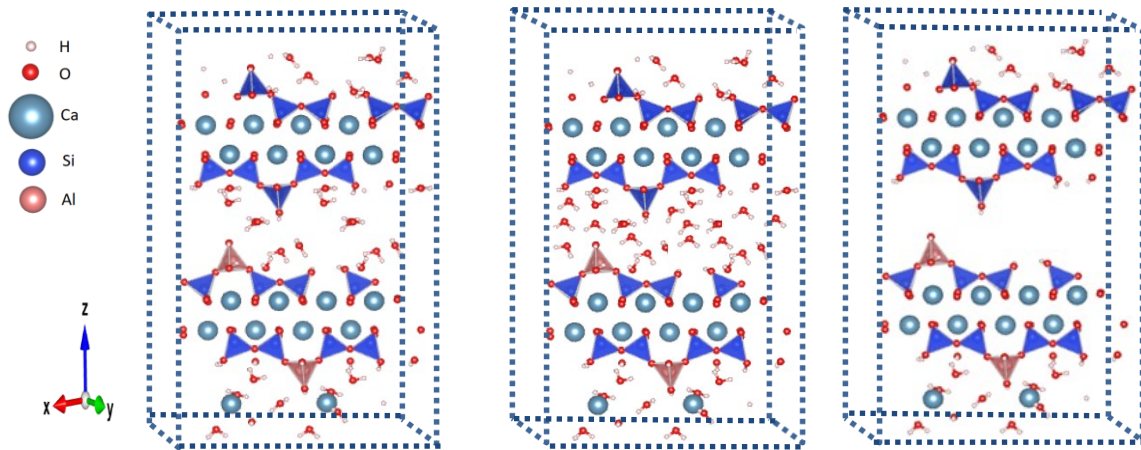
Figure 6.3 Schematic illustration of the unit cell of tobermorite-14Å structure (MCL=5, Al/Si ratio=0.18) with 12(left), 24 (middle), and zero (right) water molecules in the interlayer space.

Interactions inside the tobermorite molecule and intermolecular interactions were approximated by some empirical potentials using molecular mechanics, or so called force field (FF) methods. Such methods ignore motion of electrons inside the compounds, and describe a molecule structure as a series of charged spheres with constant weight and size (atomic nucleus) connected by springs (bonds). This approach is based on the Born-

Oppenheimer approximation, which allows for separating nuclear and electronic motions and, therefore, consider the energy of a system as a function of nuclear weights and coordinates only [228]. The force field parameters capture energy of each atom and allow calculation of the full potential energy of the system [219]. In our study, the reactive force field proposed by Van Duin et al. [229] ReaxFF was applied. This set of the parameters was further extended with Ca/O/H [230], Si/O/H [231] and Al [232] potentials to consider all interatomic interactions of the C(-A)-S-H gel structure.

6.2.2   Computational methods

The molecular structure, as a system, contains a certain amount of internal energy. The coordinates of the atoms in the unit cell should correspond to the minimum energy state for the given system. This is identified as a local minimum on the global potential energy surface, where the coordinates of each atom of the structure are closest. Therefore, the structure was optimized using the GULP code to achieve the local energy minimum [233]. The optimization was performed using the Newton–Raphson/Broyden–Fletcher–Goldfarb–Shanno (NR/BFGS) algorithm [234]. After optimization of the structure, the elastic matrix, elastic modulus (E), bulk modulus (K) and shear modulus (G), earlier presented in Table 6.1, were calculated to validate the model and demonstrate the potential of the model to simulate the response to the external load.

Let me note that from thermodynamic point of view, when a material is deformed under an applied stress within its elastic limit, it stores potential energy due to the internal stresses generated. This potential energy represents the work done on the material to deform it. The amount of potential energy stored is proportional to the degree of deformation, which is influenced by the elastic modulus of the material.

To simulate the creep deformation of a molecular structure, the LAMMPS code and the stress-marching technique [211, 235] were used. The stress-marching technique consists of a series of consecutive loading-unloading cycles of an isostatic shear stress $\tau_{zx} = \tau_0 \pm \Delta\tau$ in the xy-plane (see Figure 6.4). Such cyclic loading causes the system to deform in order to reduce the internal stress and minimize the potential energy. This behaviour mimics time-dependent material response of the material (volume change) caused by sustained loading, i.e. creep. The input parameters of the simulated molecular systems are summarized in Table 6.2. Note that these simulations do not relate directly to the creep tests discussed in Chapter 4.
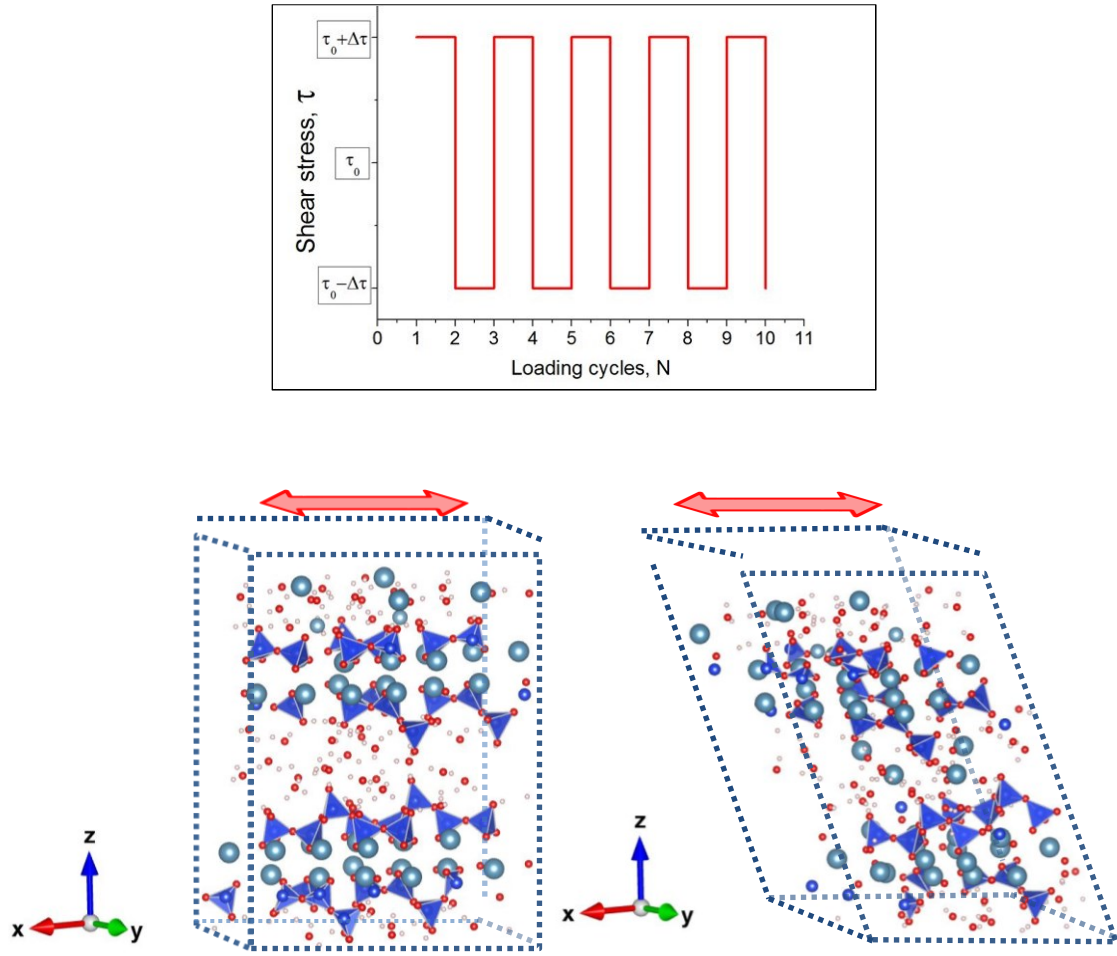
Figure 6.4 Schematic illustration of cyclic loading during simulations (top) and the model of C-S-H system, where MCL=5, with applied PBC and shear stress in the XY-plane before and after 1000 loading cycles (bottom).

Table 6.2. Input parameter of the simulated molecular systems.

Structure №	MCL	Shear modulus G GPa	Al/Si ratio	Applied load GPa
1	∞	23.4	0	0.75; 1; 1.5
2	5	13.2	0	0.75; 1; 1.5
3	5	11.3	0.11	1
4	5	14.2	0.18	1
5	5	14.8	0.25	1
6	2	12.26	0	0.75; 1; 1.5

6.3 Results and discussion

6.3.1 Role of mean chain length (MCL) on simulated creep

The strain evolution of tobermorite structures with different MCL under different load levels are shown in Figures 6.5 and 6.6. Figure 6.5 (right) shows the reduction of the potential energy of the structure, and thus deformation of the system to a lower energy state. The strain of the structure under the cyclic shear load was measured as an average change of the volume of the unit cell after each cycle. Please note that the outcomes of MD simulations capture the overall patterns of deformations in molecular structures, without reproducing the exact values of strain observed in cement paste.

The creep deformation ε can be approximated with logarithmic function Eq. 6.1:

$$\varepsilon(N) = \varepsilon_{el} + \frac{\tau_0}{C} ln\left(1 + \frac{N}{N_0}\right) \tag{6.1}$$

where ε_{el} is the initial elastic strain, $1/C$ stands for the simulated creep constant, N is the number loading cycles, N_0 is characteristic 'time' (number of loading cycles), and τ_0 is the shear stress. The parameters of the approximate strain curves according Eq. 6.1 are summarized in Table 6.3 (second row for MCL = ∞).
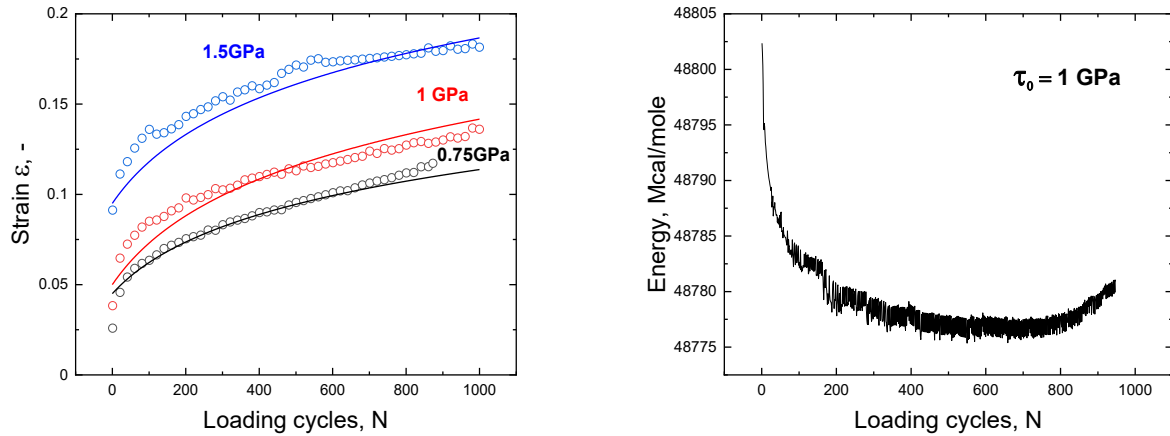
Figure 6.5 (left): Creep strain of tobermorite structure (MCL = ∞) as a function of number of the loading cycles for various values of the external shear stress. The simulation results were approximated with logarithmic function Eq.(6.1). (right): The evolution of molar energy of the system during the cycles for τ_0.=1 GPa.
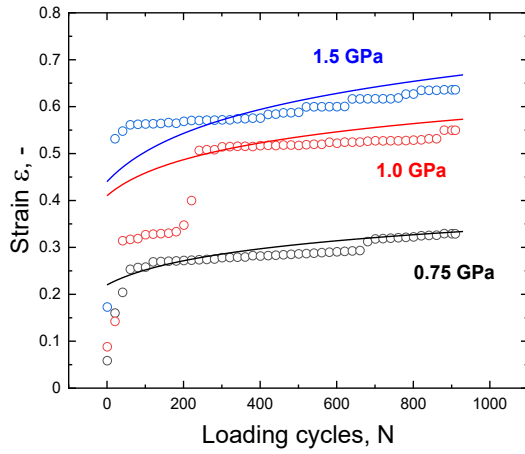
a. Chain length MCL = 5
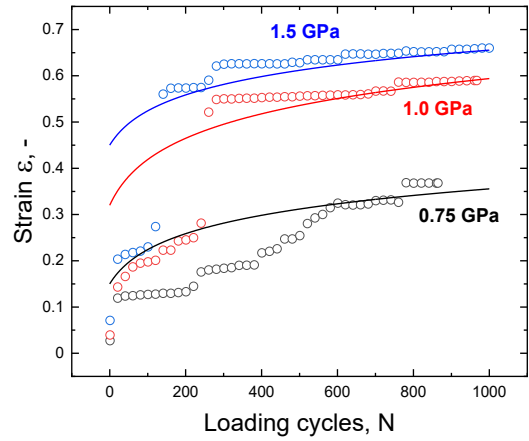
b. Chain length MCL = 2

Figure 6.6 Creep strain of tobermorite structure as a function of number of the loading cycles for various values of the external shear stress (a) The structure with mean chain length, MCL = 5. (b) The structure with mean chain length, MCL = 2. The simulation results were approximated with logarithmic function (6.1)

Table 6.3. Fitting parameters (1/C, N_0) for the creep curves approximation(Eq. 6.1)

Mean chain length MCL [--]	Creep constant $1/C$ [GPa^{-1}]	Applied shear stress τ_0 [GPa]	Characteristic 'time' N_0 [--]
∞	0.045	0.75 1 1.5	150
5	0.08	0.75 1.0 1.5	120
2	0.09	0.75 1.0 1.5	50

The strain curves of the reference structure with MCL=∞ (Figure 6.5) are in good agreement with creep simulations of a C-S-H structure performed by Morshedifard et al. [211] and Yan et al. [223], providing justification for moving forward with this model. Then the simulations were performed for the modified structures with MCL of 5 and 2. The results are shown in Figure 6.6 and in Table 6.3 (3rd and 4th row for MCL = 5 and 2).

The creep constant $1/C$ of the creep curves of the modelled structures increased as the MCL decreased. The evolutions of the strain of systems with MCL = ∞, MCL=5 and MCL = 2 were approximated with creep curves with values for the constant 1/C equal to 0.045 0.08 and 0.09, respectively.

The characteristic 'time' N_0 for strain curves decreased as the MCL decreased. The strain evolutions for systems with MCL ∞, 5 and 2 were satisfactorily fitted with N_0 values of 150, 120 and 50, respectively.

6.3.2   Role of aluminium-to-silicon (Al/Si) ratio on simulated creep

The strain evolution in a tobermorite structure with MCL=5 and different Al/Si ratio under a stress of 1 GPa is shown in Figure 6.7. The simulated strain curves were approximated with the logarithmic function Eq. 6.1. The parameters of the approximation function are summarized in Table 6.4. Insertion of Al atoms in the bridging sites resulted in higher values of the creep constant $1/C$ and the characteristic time N_0, which is in line with the results of Wang [227] for C(-A)-S-H mixes.
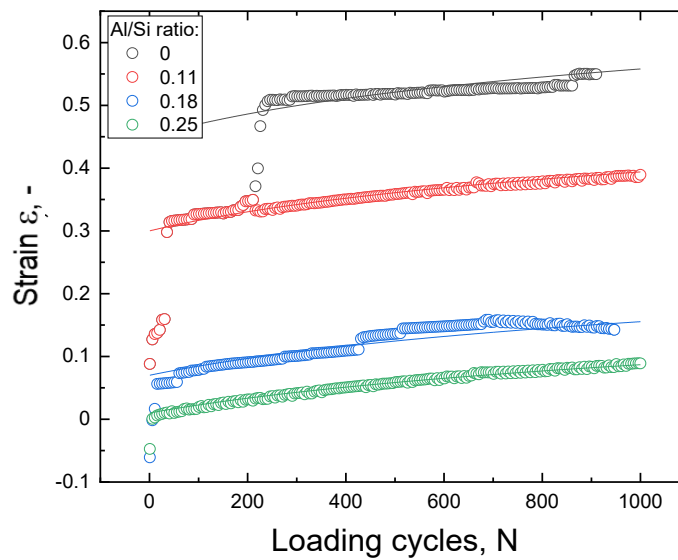
Figure 6.7 Creep strain of the tobermorite structure (mean chain length, MCL = 5) as a function of the number of loading cycles for various values of the Al/Si ratio. The simulation results were approximated with logarithmic function (6.1).

Table 6.4. Fitting parameters ($1/C$, N_0) for the creep curves approximation (Eq. 6.1) (MCL=5 and different Al/Si ratio)

Mean chain length MCL	Al/Si ratio	Creep constant $1/C$ [GPa⁻¹]	Loading value τ_0 [GPa]	Characteristic 'time' N_0
5	0	0.08	1	350
5	0.011	0.075	1	400
5	0.18	0.073	1	450
5	0.25	0.07	1	500

6.3.3 Role of interlayer water on simulated creep

The strain evolution curves of tobermorite structures with MCL=5, Al/Si ratio = 0.25 and different number of water molecules between the C(-A)-S-H layers under a stress of 1 GPa are shown in Figure 6.8. The data was approximated by the logarithmic function Eq. 6.1. The values of the parameters of the approximation function are summarized in Table 6.5.

Table 6.5. Fitting parameters (1/C, N_0) for the creep curves approximation (Eq. 6.1) (MCL=5; Al/Si ratio = 0.25; τ_0=1 GPa)

Number of water molecules between layers	Creep constant 1/C [GPa^{-1}]	Characteristic 'time' N_0
24	0.1	300
12	0.07	400
0	0.063	500
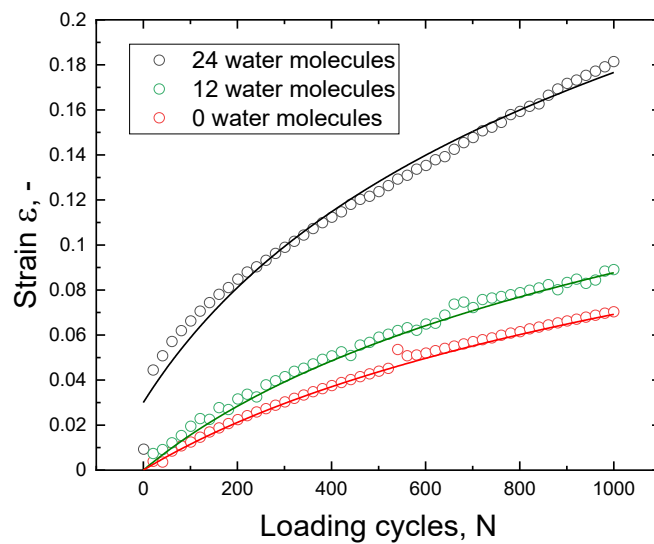
Figure 6.8 Creep strain of the tobermorite structure (mean chain length, MCL = 5) as a function of number of the loading cycles for various values of the interlayer water molecules. The simulation results were approximated with logarithmic function (6.1)

The simulation results show that changes in the amount of water in the interlayer space have an observable impact on the parameter values of the creep model, namely the creep constant *1/C* and the characteristic time *N_0* of the approximation function. The results support the hypothesis that the amount of interlayer water in the reaction products significantly affects the creep behaviour of the slag-based AAM.

The possible reason of this effect can be the role of interlayer water as a lubricant, effectively reducing the mechanical work required for generating creep deformation. This lubricating effect allows for smoother sliding between layers. Additionally, the equilibrium interlayer spacing of the tobermorite structure also depends on the hydration degree of the material [180, 212, 236]. The subsequent decrease of the cohesion via dispersive and electrostatic interactions can also facilitate easier sliding, promoting higher deformability.

6.4 Observations and conclusions

In this chapter, molecular dynamic simulations were used to investigate the creep behaviour of C(-A)-S-H gel at the molecular scale. The atomic arrangement of C(-A)-S-H gel structure resembles the naturally existing tobermorite mineral with a distance between layers of 1.4 nm (tobermorite-14Å) [117, 220]. The main parameters of the structures – mean chain length, Al/Si ratio and amount of interlayer water – were chosen based on the published studies [117, 222, 223] as close as possible to the gel formed in the mixtures described in Chapters 3-5. The virtual structures of tobermorite-14Å were subjected to a cyclic isostatic loading with amplitude ranging from 0.75 to 1.5 GPa to mimic the volume evolution, and hence creep, of the material caused by sustained loading. This method is called the stress-marching technique. Prior to the simulations the structures were optimized to minimize the potential energy. The mechanical properties (elastic modulus, bulk modulus and shear modulus) of the structures were calculated to justify the model. The simulated strain evolution curves were approximated by a logarithmic formula. The results of MD simulations were compared with the assumptions described in the observations and conclusions of Chapter 5 about the intrinsic properties of the C(-A)-S-H gel and creep mechanisms in the alkali-activated pastes (see section 5.3.4).

1. The simulation results showed that the reduction of the length of the silicate chains in molecular structure decreased the elastic modulus of the structure. This is in line with the fact that the elastic modulus of the low-crystalline alkali-activated paste measured by nanoindentation is lower than that of the cement paste (see Section 5.3.2). The reduction of the silicate chain length also increased the creep constant $1/C$ and decreased the creep characteristic time N_0. Therefore, we can assume that the low crystallinity of the molecular structure of the reaction products is one of the reasons of the relatively high creep strain and shorter characteristic time of creep strain evolution of alkali-activated materials.

2. The incorporation of Al into the molecular structure of tobermorite increased the elastic modulus E and shear modulus G of the structure. Therefore, the virtual structures with higher Al/Si ratio showed lower creep constant $1/C$ and slower creep development. These results support the assumption of dependence of the concrete creep compliance on the Ca/Si ratio and Al/Si ratio in the C(-A)-S-H gel.

3. The creep strain evolution of the modelled C-A-S-H structures was also affected by the quantity of interlayer water. The addition of extra water molecules in the interlayer space increased the creep constant $1/C$ and decreased the characteristic time N_0 of the creep strain evolution. This supports the hypothesis that a large amount of interlayer water promotes creep by reducing the cohesion between the silicate chains (layers), resulting in less mechanical work required for the initiation of creep. This can be related to the increase in interlayer distance and the lubrication function of interlayer water.

The insights gained from our molecular-scale investigations enhance our understanding of creep phenomena in alkali-activated materials. After moving from the macroscale in Chapters 3 and 4 to the micro- and nanoscale investigations in Chapter 5, we have now delved into the finest material scale reflecting material properties. The findings presented in these chapters highlight the multi-scale nature of the mechanisms underlying creep phenomena and provide quantitative estimates of the correlations between influencing factors (chemical composition, environmental conditions), mechanical properties and the evolution of creep strain. Building on this foundation, the modelling of the creep strain function will be addressed in the next chapter.

Chapter 7

Creep modelling

7.1 Introduction

This chapter explores the modelling of AAC creep based on the insights gained in the previous chapters, examining both the scientific and engineering aspects. Within structural engineering, a comprehensive understanding of concrete creep behaviour is of paramount importance, as it plays a crucial role in enhancing the resilience and safety of infrastructure. Accurate prediction of creep is essential for designing structures that can withstand sustained loads while maintaining their structural integrity and functionality over time. Two primary modelling approaches prevail to serve this purpose: theoretical models rooted in the activation energy approach and code-based engineering models.

Concrete creep modelling is attracting the attention of the scientific community because of its potential to unravel the complicated, time-dependent deformation processes down to molecular level. This takes into account variables, such as temperature and thermodynamic potential, which shed light on material properties and interactions that determine the long-term structural behaviour of concrete. On the other hand, engineering code-based models provide simplified methods for implementation in practice, but often lack the nuanced insights that more complicated theoretical models provide. This chapter aims to improve the understanding of the creep behaviour of AAC, by using both types of the models and distinguishing their attributes.

Existing code-type models use the macroscale mechanical properties of concrete as input parameters. Therefore, in Chapter 3 standard tests were performed to examine the evolution of compressive strength, splitting strength and elastic modulus. In Chapter 4 creep tests were performed to evaluate the strain evolution under sustained load in AAC.

The findings showed that creep of AAC is higher than that of OPC concrete. The creep functions of AAC were also dependent on the precursor composition and curing conditions.

Subsequently, the creep mechanism was investigated. The origin of concrete creep is commonly understood to be linked to the viscoelastic properties of the binder, and consequently, to the micro- and nanostructure of the paste. Therefore, the elastic modulus, porosity and atomic bonding were evaluated with nanoindentation, N_2 adsorption and tests. Finally, molecular dynamic (MD) simulations confirmed the hypothesis on the effect of crystallinity, Al content and interlayer water of the material structure on the creep process.

The results obtained from this study at different length scales can be used as the basis for developing a creep prediction model that directly relates to the creep mechanisms and evolution of mechanical properties of AAC. It is likely that the microprestress solidification (MPS) theory [92, 103, 179], originally developed for OPC concrete, can also be adapted for AAC by making certain adjustments to account for the unique microstructural features of the material.

In this chapter, two creep prediction formulas for AAC will be proposed, one based on the activation energy concept and one code-type model, like EuroCode 2 [8] or Model Code 2010 [137]. The models are based on earlier published findings on the mechanical properties of AAC and the results presented in this thesis. Predicted creep curves are compared to the creep test data discussed in Chapter 4.

7.2   Theoretical model and activation energy approach.

7.2.1   Theoretical models

Unlike phenomenological models, which describe observed phenomena without direct derivation from the first principles, theoretical models are based on principles widely accepted in mechanics, physics and chemistry. They can provide tangible and direct insights about phenomena, aiding understanding and validation of the hypothesis on the fundamental mechanisms. Specifically, the activation energy concept describes the energy required to initiate a particular process. The change in the height of the energy barrier $\Delta U = \sigma \Delta V$ is schematically shown in Figure 7.1 (see also section 2.4.2), where σ_0 is the applied stress and ΔV is a parameter called activation volume. The thermodynamic relation of the values of U and ΔV has been described by Gibbs [237].

It is assumed that the activation volume of creep in cementitious material does not change during the duration of loading and only depends on the composition of the paste [79]. Meanwhile, the value of the activation energy relates to the energy of underlying mechanisms that control the deformation process and thereby to the rate of creep deformation (mentioned in Chapters 2, 5 and 6 [238, 239]).
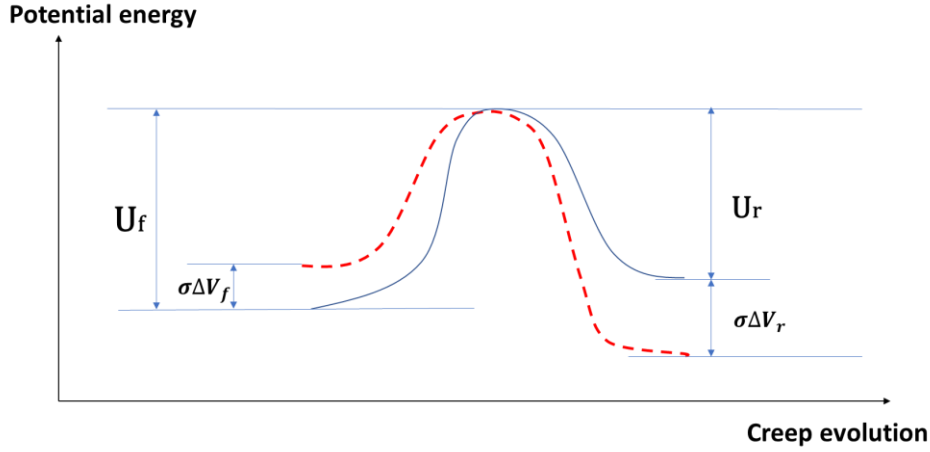
Figure 7.1 Scheme of potential energy path during the forward and reverse process activation. Initially (blue line), the states are separated by an energy barrier of height (U_f). When an external stress (σ) is applied the energy barrier is lowered (red dash line) from (U_f) to ($U_f - \sigma\Delta V_f$).

Creep deformation in concrete can be estimated using creep strain rate integration (see Chapter 2.6) [79-81, 240, 241].

$$\varepsilon_{cr}(t, t_0) = \int_{t_0}^{t} \frac{d\varepsilon_{cr}}{dt} dt = \frac{d\varepsilon_{cr}}{dt}(t - t_0) \tag{7.1}$$

The creep strain rate of concrete under the influence of sustained load can be written with the constitutive law [242]:

$$\frac{d\varepsilon_{cr}}{dt} = A_f exp\left(-\frac{(U_f - \sigma_0\Delta V_f)}{RT}\right) - A_r exp\left(-\frac{(U_r + \sigma\Delta V_r)}{RT}\right) \tag{7.2}$$

where $d\varepsilon_{cr}/dt$ is the creep strain rate, A_f the pre-exponent factor in forward activation, A_r the pre-exponent factor in reverse activation, U_f the activation energy in forward activation, U_r the activation energy in reverse activation, ΔV_f the activation volume in forward activation, ΔV_r the activation volume in reverse activation and σ_0 the applied stress.

At low stress levels, i.e. low compared to the strength, uniaxial load, and moderate temperature, it is usually assumed that the material characteristics associated with the forward and reverse activation have more or less the same magnitude, thus: $A_f \approx A_r \approx A$, $U_f \approx U_r \approx U$ and $\Delta V_f \approx \Delta V_r \approx \Delta V$. Under these conditions the creep rate can be written as:

$$\frac{d\varepsilon_{cr}}{dt} = 2A^* exp\left(-\frac{U}{RT}\right) sinh\left(\frac{\sigma\Delta V}{RT}\right) \tag{7.3}$$

Assuming that the temperature T is constant, and magnitude of the activation energy U and the activation volume ΔV are almost independent of the duration of the loading, the creep rate equation (7.3) after integration and further simplification of the result yields [79, 182] :

$$\varepsilon_{cr} = C\ t^{p*}\ \sigma_0 \qquad\qquad (7.4)$$

where C is an empirical ageing factor, which depends on the age at loading, the initial liquid-to-binder ratio, precursor composition and moisture content [79, 182]; t is the duration under load; $p*$ is a proportionality factor. The proportionality factor $p*$ for compression tests is often found equal 0.3 [79, 182, 243].

Wittmann [244] stated that the moisture content has a significant influence on the activation volume of concrete creep. The lower the moisture content of concrete, the lower creep strain will be monitored. So, creep of saturated specimens is at maximum. Therefore parameters of the equation (7.4) C and $p*$ need to be dependent on the moisture content of concrete and the RH. However, as shown in Chapter 4, the creep in AAC is mainly affected by the precursor composition of the mixture. Any possible effect of liquid-to-binder ratio and RH on the parameters C and $p*$ for AAC is still subject of further research.

7.2.2 Creep modelling using activation energy approach

The creep strain evolution was modelled using Eq. (7.4). Then the creep coefficient was calculated based on Eq. (4.2) (see Chapter 4):

$$\phi(t', t) = \frac{\varepsilon_{cc}(t,t')}{\varepsilon_{el}(t')} \qquad\qquad (4.2)$$

where $\varepsilon_{cc}(t,t')$ is the basic creep and $\varepsilon_{el}(t')$ the elastic strain measured on loading of a specimen at time t'.

The results of the creep tests (see Chapter 4) and modelled creep coefficient are shown in Figure 7.2. Non-linear numerical curve fitting was applied to find the parameters C and p. The adopted parameters for Eq. (7.4) are shown in Table 7.1.

<div align="center">b. Moist curing until 28 days   b. Sealed curing until 28 days</div>
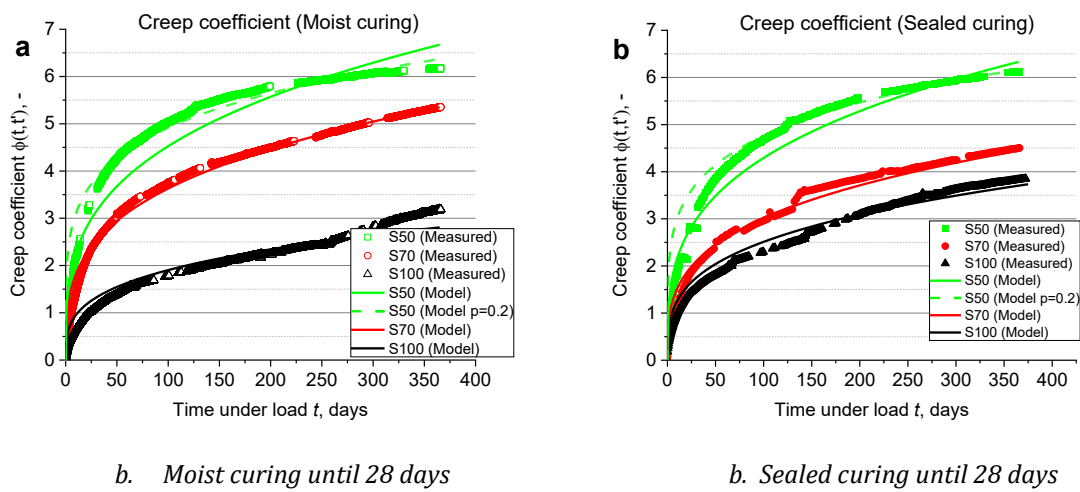
Figure 7.2 Evolution of the creep coefficient during 365 days after 28 days of (a) moist and (b) sealed curing and loading initiation and creep modelling results Eq. (7.4).

Table 7.1. Parameters of the model based on the activation energy approach

Tested mixture	Ageing factor C		Proportionality factor $p*$		Applied stress σ, MPa	
	moist curing	sealed curing	moist curing	sealed curing	moist curing	sealed curing
S100	1.3	1.8	0.3	0.3	35.3	34.7
S70	2.5	2.2	0.3	0.3	23.7	23.4
S50	3.6	3.3	0.3	0.3	22.1	23.2
S50	6.2	5.8	0.2	0.2	22.1	23.2

The approximation of creep test results using the Eq. (7.4) and (4.2) with parameter $p*=0.3$ results provide a good approximation for the creep evolution data for S100 and S70 mixtures up to 365 days. The same approximation function for S50 mixture also gives satisfying estimation of the creep coefficient.

The parameter $p*=0.2$ provides a better fit for the creep coefficient function of the S50 mixture. The aging parameter p for the creep model in AAC can be adjusted based on the composition of the precursors. Notably, $p*$ decreases when blending slag with fly ash. However, to establish this relationship more accurately, additional experimental data is needed.

The values of ageing factor C of the model show correlation with the precursor ratio of the material and with the 28 days compressive strength (Figure 7.3). C linearly decreased with the decrease of the fly ash content in the binder and with the increase of the compressive strength. However, to clearly demonstrate the dependence of these parameters, additional experimental data is required.
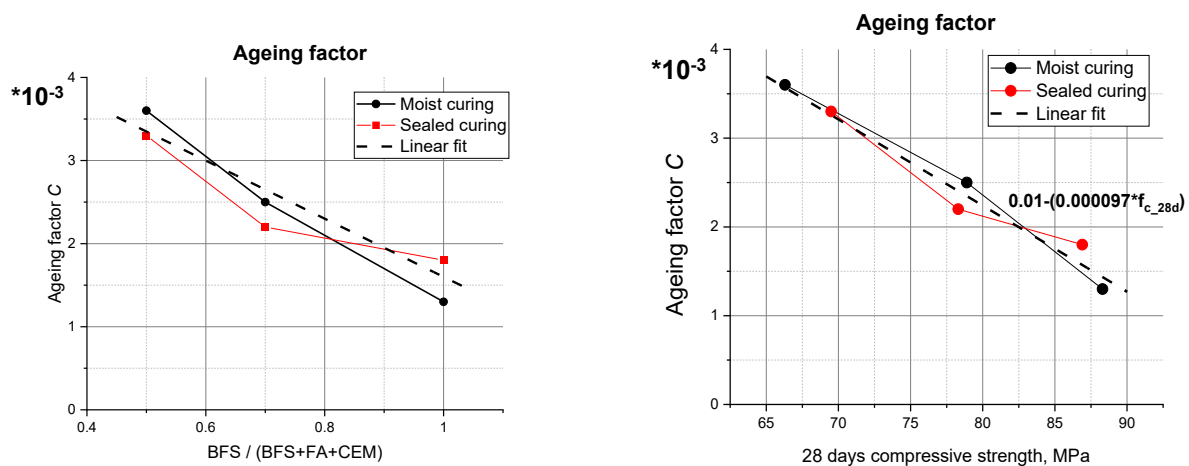
Figure 7.3 Ageing factor of creep strain in AAC. vs. precursor ratio of alkali-activated pastes (left) and vs. the 28 days compressive strength of the tested concrete.

7.3 Code-type modelling.

The code-type creep models, like those mentioned in Chapter 2, are formulated without an explicit description of creep mechanisms. They are calibrated and fitted according to the concrete strength class and type of structural element.

The two code-type models most widely used in Europe are the EuroCode (EC) 2 [8] and the fib Model Code 2010 [137]. The fib Model Code 2010 (MC2010) treats the creep coefficient, $\varphi(t,t_0)$, as a product of two components: $\varphi_{bc}(t,t_0)$ for the basic creep coefficient and $\varphi_{dc}(t,t_0)$ for the drying creep coefficient. The results of our creep tests on AAC specimens (Chapter 4), however, are hard to interpret as a sum of separate basic and drying components, as the samples were not sealed during the tests. Therefore, we choose the EC2 model for modelling creep in AAC. However, modelling the creep behaviour of AAC using EC2 is also not straightforward. As shown in Chapter 4, the mechanical properties of AAC differ from those of OPC. Furthermore, it lacks comprehensive creep data for model calibration. Because of differences in microstructure, the sensitivity of AAC to temperature and environmental conditions is expected to be different from that of OPC concrete. Factors used in EC2 to describe this sensitivity of OPC concrete do not necessary apply for AAC. This means that engineers have to conduct extensive material testing in order to make the code applicable for AAC.

7.3.1 Eurocode 2 approximation

The EuroCode 2 standard (BS EN 1992-1-1:2004) [8] provides basic equations for determining the evolution of the creep coefficient over time. The creep coefficient function $\varphi(t,t_0)$ is calculated as the product of the notional creep coefficient, φ_0, and a factor which describes the development of creep with time, $\beta_c(t,t_0)$ (with: $\beta_c(t,t_0=0) = 0$, and $\beta_c(t, t_0= \infty) = 1$). In formula form:

$$\varphi(t,t_0) = \varphi_0 \cdot \beta_c(t,t_0) \tag{7.6}$$

in which:

$$\varphi_0 = \varphi_{RH} \cdot \beta(f_{cm}) \cdot \beta(t_0) \tag{7.7}$$

$$\beta_c(t,t_0) = [(t - t_0)/(\beta_H + t - t_0)]^n \tag{7.8}$$

where β_H should have the dimension time, and n is a power, by default n=0.3.

φ_{RH} is the factor for the effect of relative humidity RH and the fictitious thickness h_0:

$$\varphi_{RH} = \left[1 + \frac{1-RH/100}{0.1 \cdot \sqrt[3]{h_0}} \cdot \alpha_1\right] \cdot \alpha_2 \qquad \text{for } f_{cm} > 35 \text{ MPa} \tag{7.9}$$

The fictitious thickness h_0 is calculated as $h_0 = 2A/u$, with A the cross-sectional area of concrete in mm^2 and u the perimeter of the member in contact with the atmosphere in mm. For the parameters α_1 and α_2 is holds: $\alpha_1 = (35/f_{cm})^{0.7}$ and $\alpha_2 = (35/f_{cm})^{0.2}$.

The factor $\beta(f_{cm})$ in eq. (7.7) is based on the mean compressive strength f_{cm} of concrete in MPa:

$$\beta(f_{cm}) = 16.8/(f_{cm}^{0.5}) \tag{7.10}$$

while the factor $\beta(t_0)$ in eq. (7.7) accounts for the age of concrete at time of loading t_0:

$$\beta(t_0) = \frac{1}{(0.1 + t_0^{0.2})} \tag{7.11}$$

The factor β_H depends of the relative humidity RH according to:

$$\beta_H = 1.5 \cdot [1 + (0.012\,RH)^{18}] \cdot h_0 + 250 \cdot \alpha_3 \qquad \text{for } f_{cm} > 35 \text{ MPa} \tag{7.12}$$

in which α_3 is a parameter calculated from the compressive strength f_{cm} with:

$$\alpha_3 = (35/f_{cm})^{0.5} \tag{7.13}$$

In the first attempt to assess the suitability of the EC2 model for predicting the creep of AAC, the equations (7.6)-(7.13) of the EC2 were used for determining the creep factors of the different AAC mixtures. Calculated parameter values are summarized in Table 7.2.

The parameters of the model were taken according to our creep tests on the AAC, namely t_0=28 days, RH=55%, h_0=50 mm and compressive strength f_{cm} (see section 4.2.1). Figure 7.4 presents the results of the creep tests (presented earlier in Chapter 4) and the predictions according the EC2 developed for OPC concrete.

The curves in Figure 7.4 show large discrepancies between the predictions with the EC2 model and the measured creep data. The EC2 model significantly underestimates the magnitude of the measured creep of AAC. The shape of the predicted curves also differs significantly from the curves predicted with the EC2. The next section deals with a proposal for modifications of the EC2 creep concept in order to eliminate the perceived discrepancies.

Table 7.2. Parameter values for AAC mixtures of EuroCode 2 creep model (original EC2 concept)

Creep coefficient factor		S100	S70	S50	S100	S70	S50
		moist curing			sealed curing		
RH [%]		55	55	55	55	55	55
h_0 [mm]		50	50	50	50	50	50
f_{cm} [MPa]		88.3	78.9	66.3	86.9	78.3	69.5
φ_{RH}	$\left[1 + \dfrac{1 - RH/100}{0.1 \cdot \sqrt[3]{h_0}} \cdot \alpha_1\right] \cdot \alpha_2$	1.36	1.44	1.57	1.37	1.44	1.53
α_1	$(35/f_{cm})^{0.7}$	0.52	0.57	0.64	0.53	0.57	0.62
α_2	$(35/f_{cm})^{0.2}$	0.83	0.85	0.88	0.83	0.85	0.87
$\beta(f_{cm})$	$16.8/(f_{cm})^{0.5}$	1.79	1.89	2.06	1.8	1.9	2.01
$\beta(t_0)$	$\dfrac{1}{(0.1 + t_0^{0.2})}$	0.49	0.49	0.49	0.49	0.49	0.49
φ_0	$\varphi_{RH} \cdot \beta(f_{cm}) \cdot \beta(t_0)$	1.19	1.33	1.58	1.21	1.34	1.51
β_H	$1.5[1 + (0.012\,RH)^{18}]h_0 + 250 \cdot \alpha_3$	232	242	257	234	242	252
α_3	$(35/f_{cm})^{0.5}$	0.63	0.67	0.73	0.63	0.67	0.71
β_c	$((t - t_0)/(\beta_H + t - t_0))^{0.3}$						
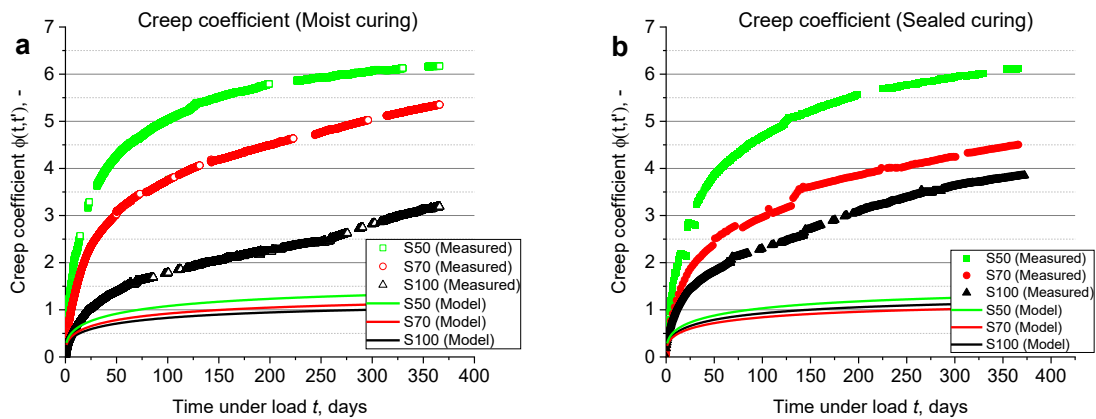
Figure 7.4 Evolution of the creep coefficient during 365 days after 28 days of (a) moist and (b) sealed curing and loading initiation and creep modelling results Eq. (7.6)-(7.13).

7.3.2 Proposed modifications of EC2 creep model for AAC

For an attempt to make EC2 applicable for predicting creep of AAC mixtures, we first refer to the measured creep strain curve of AAC and OPC concrete presented in Chapter 4. There was found that the evolution of the creep coefficient can be approximated with an exponential function (4.6):

$$\phi(t) = \phi_0 \cdot (1 - B'' \cdot \exp(-t/t_0^*)) \tag{4.6}$$

where ϕ_0 is an ultimate creep coefficient, B'' is a fitting parameter close to 1, and t_0^* is the characteristic time.

Note, that the shape of the creep coefficient curve is characterized by only two parameters, i.e. ϕ_0 and t_0^*, which both depend on the precursor composition. As shown in the Figures 4.14 and 4.15, the ultimate creep coefficient ϕ_0 slightly decreased and the characteristic time t_0^* strongly increased with increasing BFS/(BFS+FA) ratio in the mixture (see section 4.3.2.4).

It is worth noting that, although the ultimate creep coefficient ϕ_0 appeared to be only slightly dependent on the precursor ratio, its value was much higher than that of OPC concrete mixtures (about 4 times higher than that of the reference OPC C65; see Figure 4.14). Furthermore it is emphasized that the shape of the exponential function (4.6) strongly depends on the characteristic time t_0^*. This parameter described the rate of the creep process, particularly in the early stage of the creep process.

For the attempt to make EC2 applicable for predicting creep of AAC mixtures, it is good to realise that, in essence, also creep predictions according EC2 contain two components, which determines the shape of the creep curve, namely a maximum creep factor φ_0, and a factor $\beta_C(t,t_0)$. In formula form (eq. (7.6)):

$$\varphi(t,t_0) = \varphi_0 \cdot \beta_c(t,t_0) \tag{7.6}$$

In EC2 the factor $\beta_C(t,t_0)$ is a power function with power n. For OPC concrete the default value of *n* is 0.3 (see eq. (7.8)). Note that the rate of creep is determined by the value of the power *n*. The role of the power *n* is comparable with the role of the characteristic time t_0^* in the exponential function (4.6).

Based on foregoing considerations the following adjustments of the EC2 are proposed to make this code applicable for creep predictions of AAC mixtures:

1. Adopting a *creep enhancement factor* $\varphi_{0,AAC}$, to account for the higher ultimate creep of AAC mixtures compared to OPC mixtures. This creep enhancement factor is inserted into equation (7.7) for calculation of φ_0 and thus equal:

$$\varphi_0 = \varphi_{RH} \cdot \beta(f_{cm}) \cdot \beta(t_0) \cdot \varphi_{0,AAC} \tag{7.14}$$

2. Adopting a *precursor-dependent* value of the power *n* in the rate factor $\beta_c(t,t_0)$:

$$\beta_c(t,t_0) = [(t - t_0)/(\beta_H + t - t_0)]^{\,n(B/F)} \tag{7.15}$$

where B/F stands for the precursor ratio BFS/(BFS+FA).

All other factors used in the EC2 for calculating the creep factor $\varphi(tt_0)$, shown already in Table 7.2, are left unchanged.

The values of the parameters $\varphi_{0,AAC}$ and *n(B/F)*, for a which a good fit of measured creep coefficients was obtained, are presented in Figure 7.5. The values for the factor $\varphi_{0,AAC}$ are indeed close to 4, as expected. $\varphi_{0,AAC}$ for the specimens cured in both moist and sealed conditions exhibits a slight dependency on the type of mixtures, i.e. on the precursor ratio (B/F), as (with rounded numbers):

$$\varphi_{0,AAC}(B/F) = 6.68 - 3.29 \cdot B/F \qquad (0.5 < B/F < 1.0, \text{ moist curing}) \tag{7.16a}$$

$$\varphi_{0,AAC}(B/F) = 5.9 - 1.93 \cdot B/F \qquad (0.5 < B/F < 1.0, \text{ sealed curing}) \tag{7.16b}$$

where B/F stands for the precursor ratio BFS/(BFS+FA).

The values of the power coefficient *n* turn out to be strongly dependent on the mixture composition. There is also a non-negligible difference between *n*-value for moist and sealed cured specimens, leading to two separate linear dependencies between *n(B/F)* and the precursors' ratio, viz. (with rounded numbers):

$$n(B/F) = 0.581 \cdot B/F + 0.053 \qquad (0.5 < B/F < 1.0, \text{ moist curing}) \tag{7.17a}$$

$$n(B/F) = 0.395 \cdot B/F + 0.21 \qquad (0.5 < B/F < 1.0, \text{ sealed curing}) \tag{7.17b}$$

where B/F stands for the precursor ratio BFS/(BFS+FA).

Note, that for the sealed specimens with precursor ratio of 0.5 (S50) the value of *n* is not much higher than 0.3. This is the default value in the EC2 for OPC concrete. This observation is consistent with the earlier found values for the characteristic time t_0^* of the S50 mixture and the reference concrete mixture C65, shown in Figure 4.15. That figure indicates that both S50 and the reference mixture have about the same characteristic time, which means a similar evolution of creep with time. This illustrates that the characteristic time t_0^* in the exponential function for creep plays the same role as the power *n(B/F)* in EC2 (the latter operating with a power function).
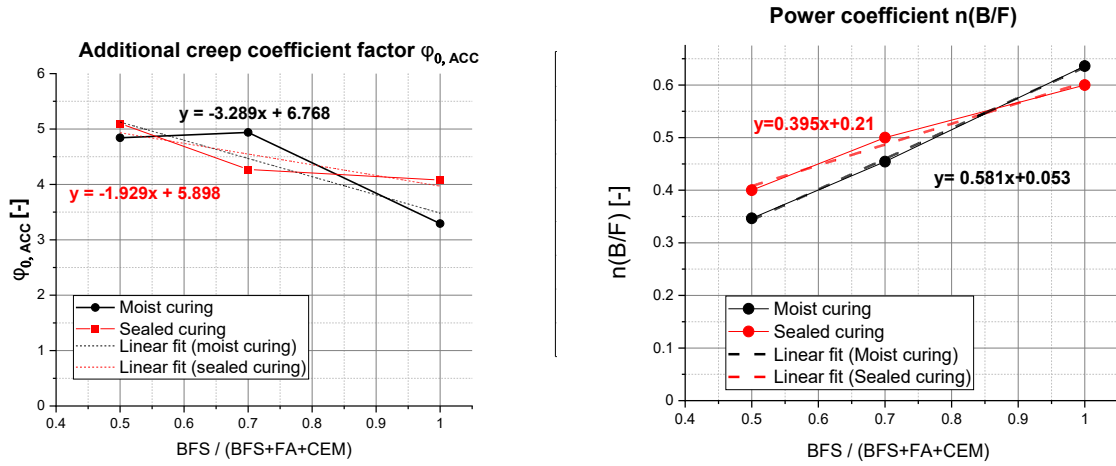
Figure 7.5 Additional creep factor φ₀,ₐₐ𝒸 (left) and power n(B/F) (right) as function of the precursor composition. Values obtained from curve fitting of experimental creep coefficient data (shown in Figure 7.4) with EC2 equations (7.6) – (7.13).

The equations (7.16) for the addition creep factor $\varphi_{0,AAC}$, as well as equation (7.17) for the power n(B/F), are now inserted into the EC2 calculation scheme for the creep coefficient. Table 7.3 shows the proposed modifications of the calculation scheme compared to the scheme of Table 7.2. The modifications are indicated in red.

Note, that in practice most of the concrete will harden under, more or less, sealed condition. This certainly holds for the interior of concrete elements. Hence, the results obtained from the sealed series are supposed to simulate reality better than that of the moist series.

The results of the modelling are shown in Figure 7.6. The adjustment of $\varphi_{0,AAC}$ and n(B/F) was enough to achieve good agreement of the EC2 model and the experimental data.
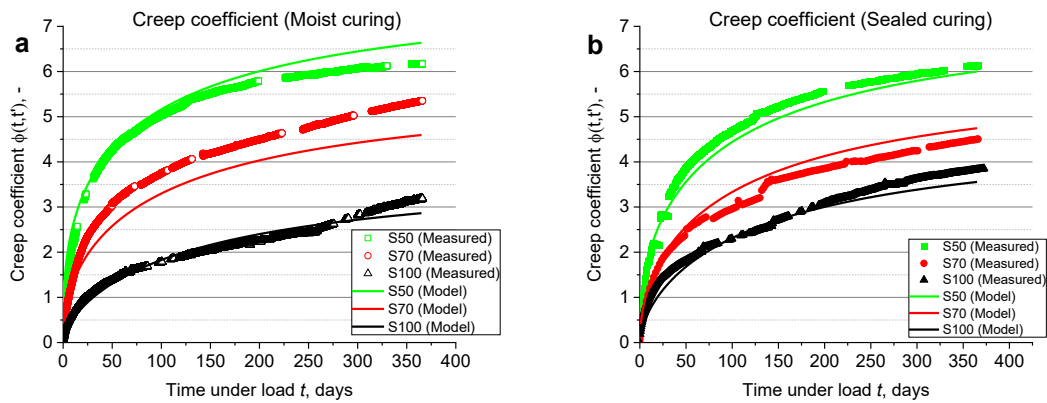
Figure 7.6 Evolution of the creep coefficient during 365 days after 28 days of (a) moist and (b) sealed curing and loading initiation and creep modelling results (Table 7.3).

123

Table 7.3. Factors of the code-type model of creep adjusted for AAC

Factor	Formula	S100	S70	S50	S100	S70	S50
			moist curing			sealed curing	
RH [%]		55	55	55	55	55	55
h_0 [mm]	$2A/u$	50	50	50	50	50	50
B/F	BFS/(BFS+FA)	1.0	0.7	0.5	1.0	0.7	0.5
f_{cm}		88.3	78.9	66.3	86.9	78.3	69.5
φ_{RH}	$\left[1 + \dfrac{1 - RH/100}{0.1 \cdot \sqrt[3]{h_0}} \cdot \alpha_1\right] \cdot \alpha_2$	1.36	1.44	1.57	1.37	1.44	1.53
α_1	$(35/f_{cm})^{0.7}$	0.52	0.57	0.64	0.53	0.57	0.62
α_2	$(35/f_{cm})^{0.2}$	0.83	0.85	0.88	0.83	0.85	0.87
$\beta(f_{cm})$	$16.8/(f_{cm})^{0.5}$	1.79	1.89	2.06	1.8	1.9	2.01
$\beta(t_0)$	$\dfrac{1}{(0.1 + t_0^{0.2})}$	0.49	0.49	0.49	0.49	0.49	0.49
$\varphi_{0, AAC}$	$6.68 - 3.29 \cdot$ B/F (moist curing)	3.29	4.37	5.035	--	--	--
$\varphi_{0, AAC}$	$5.9 - 1.93 \cdot$ B/F (sealed curing)	--	--	--	3.97	4.55	4.94
φ_0,	$\varphi_{0, AAC} \cdot \varphi_{RH} \cdot \beta(f_{cm}) \cdot \beta(t_0)$	3.92	5.82	7.98	4.79	6.1	7.44
β_H	$1.5[1 + (0.012 \, RH)^{18}]h_0 + 250 \cdot \alpha_3$	232	242	257	234	242	252
α_3	$(35/f_{cm})^{0.5}$	0.63	0.67	0.73	0.63	0.67	0.71
n(B/F)	$0.581 \cdot$ B/F + 0.053 (moist curing)	0.634	0.46	0.34	--	--	--
n(B/F)	$0.395 \cdot$ B/F + 0.21 (sealed curing)	--	--	--	0.605	0.49	0.41
β_c	$[(t - t_0)/(\beta_H + t - t_0)]^{n(B/F)}$						

To further validate the proposed modified model, findings obtained with the modified model were compared with the experimental results presented in Un [18] and Ma et al. [135], as shown in Figure 7.7. In the referenced studies experiments were conducted on slag-based AAC under conditions similar to those in our study. Further details are available in the references.

This additional validation step was intended to underscore the robustness of the proposed model. The results of Un [18] after 120 days of loading closely align with the values predicted by our model, suggesting a favourable outcome. On the other hand, the results of Ma [135] show considerable deviation from the model. A plausible explanation for this deviation is the notably different quality of the slag used as a precursor for the AAC. Although the model appears to perform satisfactory, further experimental data is essential to broaden the scope of model applicability.
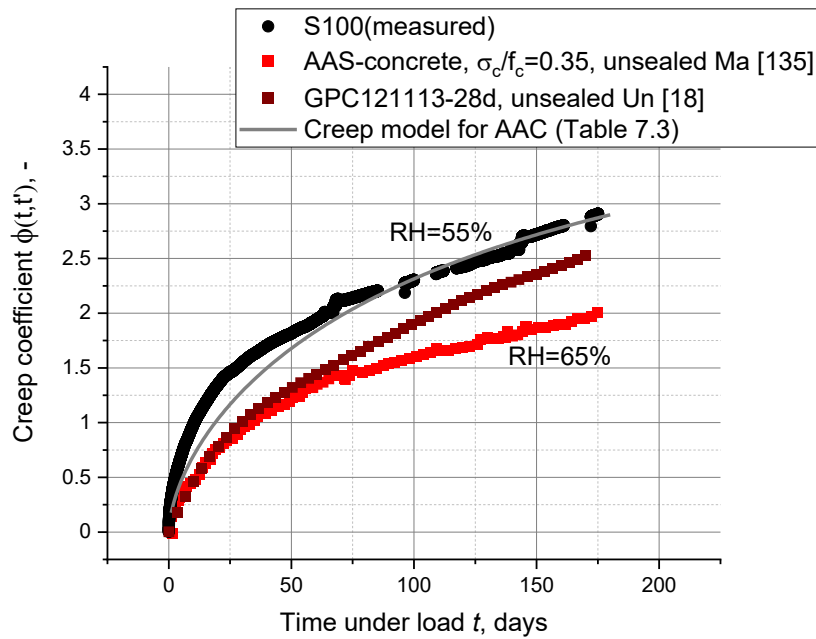
Figure 7.7 Evolution of the creep coefficient during 175 days after 28 days of sealed curing and loading initiation and the creep modelling results. The results of this thesis are compared with the results from the references [18, 135].

7.4 Conclusions

This chapter aimed to formulate two creep prediction models for AAC. The first model was developed based on activation energy approach; the second model adjusted the EC2 creep model (developed for OPC concrete) for AAC. For both models the results from the previous chapters were considered. The results were compared to the creep test data (see also Chapter 4). Based on the findings the following conclusions and suggestions are made:

- The model based on activation energy approach showed good agreement with the experimental data over the considered time range. The parameters of the model were determined by fitting the curves with the creep tests results.

- The ageing factor C (Eq. 7.4) decreased linearly with a increase of BFS content in the concrete mixture and subsequently with an increase of the 28-days compressive strength.
- The proportionality factor of the model p^*=0.3 (Eq. 7.4) provided a good fit for mixtures S100 and S70, and satisfactory fit for the S50 concrete mixture.

Although good fits were obtained for the adjusted parameter values, additional experimental research is required to establish the relationship between p and the precursor composition, thus expanding the precision and limits of the model applicability.

- The EC2 model developed for OPC concrete does not take into account higher creep observed in AAC, nor the dependence of the creep coefficient on the precursor ratio for AAC. The suggested adjustments of the model concern a creep enhancement factor $\varphi_{0,AAC}$ (to account for the higher ultimate creep of AAC mixtures compared to OPC mixtures) and a precursor-dependent value of the power coefficient n in the rate factor $\beta_c(t,t_0)$. These proposed adjustments have been calibrated with six curves of creep evolution data for AAC, three for moist and three for sealed type of curing separately. The modelling results were in good agreement with the experimental data.

- In order to improve the applicability of the engineering code-type model, more creep test data is needed to consider the effects of other affecting factors, such as RH, age at the moment of loading, type of activator, low strength (under 40 MPa), different loading levels, size and dimensions of elements, etc.

Chapter 8

Conclusions and recommendations

8.1 Retrospection

These days, climate change has emerged as the most pressing global concern, driving a paradigm shift in various industries, including the construction industry. The conventional cement, which is known for significant carbon emissions during its manufacturing process, needs to be gradually replaced by environmentally friendlier alternatives. AAMs are emerging as promising alternatives to OPC in many regions, offering a sustainable, low-carbon footprint solution for the construction industry. The introduction of a new construction material requires full certification, supported by confirmed and reproducible results of mechanical testing.

The current EuroCode 2 (EN 1995-1-1) (EC2) [8] does not include recommendations for the use of AAC, and producers still lack essential experimental data and reliable prediction models for long-term mechanical properties, especially with regard to creep and shrinkage phenomena. The impact of creep and shrinkage on the durability and long-term performance of concrete structures is a major concern. Creep and shrinkage can lead to substantial deflections in bridges, undesirable shortening of structural elements and surface cracks, promoting water ingress and reinforcement corrosion. This thesis aimed to evaluate the creep behaviour of AAC, clarify creep mechanisms in AAC and develop an creep model for AAC. To achieve these goals, the creep and mechanical properties of AAC were tested and compared with those of OPC concrete. Then, microstructure and nanoscale viscoelastic properties of alkali-activated paste were investigated. Molecular-scale creep of the main reaction products was simulated using molecular dynamics. Finally, the two creep prediction functions, based on activation energy approach and EC2

model, were developed and partially validated using our creep test results. A summary of the key observations of this thesis is given below.

The research started by performing tests on the mechanical properties of AAC mixtures, as described in **Chapter 3.** Compressive strength, splitting tensile strength and elastic modulus of concrete mixtures were tested on specimens of AAC and the reference ordinary OPC concrete C65 at different ages.

o The AAC mixtures showed the ability to achieve the compressive strength level of reference OPC concrete C65, but showed lower elastic modulus and splitting tensile strength.

o Blending slag with fly ash decreased the overall compressive strength, splitting tensile strength and elastic modulus of concrete samples cured under both moist and sealed conditions during first 28 days after casting.

o The AAC specimens cured in sealed conditions during the first 28 days showed higher compressive strength, elastic modulus and splitting strength compared to the same specimens cured in the fog room. However, the long-term storage at 55% RH almost nullified the effect of the initial curing regime.

o The evolution of compressive strength with time was different from the evolution of the elastic modulus and splitting tensile strength of the AAC. The compressive strength increased with time until maximum value, followed by an almost constant value with only some minor decrease. The elastic modulus and splitting tensile strength of the AAC specimens showed maximum values at the age of about 28 days. Then the values of these mechanical properties decreased by 20-30% at the age 90 days at 55% RH. In contrast, the elastic modulus and the splitting tensile strength of the reference concrete C65 were almost stable in time at 55% RH.

Chapter 4 described the program and results of the long-term creep and free shrinkage tests on AAC mixtures and the C65 reference concrete mixture.

o The AAC mixtures showed significantly higher creep than the reference OPC concrete C65. Moreover, in contrast to C65, the creep curves of the AAC mixtures showed continuous growth, even after one year under load.

o The diagrams of the ultimate creep coefficient and ultimate creep compliance versus 28-day compressive strength and elastic modulus did not show a clear correlation between measured mechanical properties. Despite similar 28-day compressive strength and elastic modulus, all AAC mixtures showed significantly higher creep coefficients than the reference OPC concrete.

o The free shrinkage of AAC specimens, subjected to 55% RH at an age of 28 days, was, in general, higher than that of the reference C65 concrete. The shrinkage strain developed rapidly up to the certain value and continued to develop at a low rate.

In **Chapter 5** creep mechanisms in alkali activated pastes were studied and discussed. Primary investigations on the evolution of the microstructure of the material and

nanoscale elastic modulus of the paste specimens with different FA and BFS ratios were performed in order to find out the origin of specific creep mechanisms in the alkali-activated pastes. For this purpose nanoindentation, N_2 adsorption and XRD tests were conducted.

o   XRD analysis showed, that the crystalline phases of the tested alkali-activated materials were stable over time. Meanwhile, the results of nanoindentation and N_2 adsorption tests indicated the process of filling the pores.

o   The nanoindentation tests have shown that the microscale elastic modulus of alkali-activated pastes depends on the precursor composition. Average values of the elastic modulus of S100 paste (100% slag) and S50 paste (50% fly ash-blended) after 28 days were 24.7 GPa and 22.7 GPa, respectively. These elastic moduli are lower than the typical value of high-density C-S-H gel. For both mixtures, the elastic modulus increased with time. After 365 days the microscale elastic modulus of S100 and S50 (sealed specimens) were 27.9 GPa and 23.2 GPa, respectively.

o   Nitrogen adsorption tests have shown that blending slag with fly ash resulted in a material with higher porosity. It also affected the pore size distribution and maximum pore size. In slag and fly ash based alkali-activated paste the overall pore volume decreased with time and an increase of pores smaller than 150 Å was observed. The BET surface area and maximum pore size correlated with the average value of the microscale elastic modulus.

Chapter 6 was devoted to the molecular dynamic simulations of creep in alkali activated reaction products. Atomistic simulations were performed using the incremental stress-marching technique to investigate creep behaviour of C-S-H and C-A-S-H gels at the molecular level and to evaluate the effect of C(-A)-S-H gel structure on the creep strain development.

o   The simulation results showed that the reduction of the length of the silicate chains of the molecular structure of tobermorite reduced its elastic modulus. This is in line with the fact that the elastic modulus of low-crystalline alkali-activated paste measured by nanoindentation is lower than that of cement paste. The reduction of the silicate chain length also increased the ultimate creep value and decreased the creep characteristic time.

o   The incorporation of Al into the molecular structure of tobermorite increased the elastic and shear modulus of the structure. Therefore, virtual structures with higher Al/Si ratio showed lower creep values and slower creep development.

o   The creep strain evolution of the modelled C-A-S-H structures was also affected by the amount of interlayer water. The addition of extra water molecules in the interlayer space increased the creep magnitude and decreased the characteristic time of the creep strain evolution.

Finally, in **Chapter 7** two creep models were used as basis for developing creep functions for AAC. The first model is starts from the activation energy approach and the evolution

of creep is described with a power function. The second model adapts the EC2 creep model, originally designed for OPC concrete, to the characteristics of AAC. The EC2 model consists of a set of formulas, each of them accounting for specific creep-influencing factors. For validating proposed modifications for these models, simulation results with the modified models were compared to creep test data presented in Chapter 4.

o The power function for describing creep, based on the activation energy approach, operates with an ageing factor C and a power of time p. A fit procedure was performed to determine the factors C and p as function of the composition of the AAC mixture, particularly the precursor ratio of these mixtures.

o The development of the code-type model took into account the higher creep observed in AAC compared to OPC concrete with equivalent strength values, and the dependence of creep coefficient rate on the precursor ratio for AAC. The suggested adjustments of the model consider an enhancement factor for creep coefficient $\varphi_{0,AAC}$ and a linear relationship of the power function coefficient and the precursor ratio. The proposed adjustments have been calibrated with six curves of creep evolution data for AAC, three for moist and three for sealed type of curing separately. The creep predictions with the modified model were in good agreement with the experimental data.

8.2   Conclusions and recommendations

This PhD thesis contributes to the research and development of an environment friendly alternative to ordinary cement based on alkaline activated fly ash and blast furnace slag. In particular, it contributes to the systematic multi-scale investigation and understanding of the creep mechanism in alkali activated pastes and concretes. The study helped the identification of the governing parameters of creep in AAC at multiple scales. The main conclusions of the thesis are:

- In this research, we succeeded in developing a framework for the systematic assessment of the time-dependent deformation and mechanical behaviour of AAC under sustained loads, as formulated in the goals of the project. The evolution of creep strain of concrete, expressed by its magnitude and characteristic time, depends on many intrinsic properties and external factors (e.g. mixture design, curing conditions, temperature and RH) and correlates with the material properties at different scales. This approach allowed to trace creep back to the material structure of concrete. The research addressed experimental and theoretical methods to investigate the effect of macroscale mechanical properties of concrete, microstructure and microscale mechanical properties of pastes and the molecular structure of reaction products on the creep behaviour of AAC.
- AAC mixtures showed significantly higher creep strain values than OPC C65 concrete, despite their comparable 28-day compressive strength and elastic modulus. Assuming that the creep behaviour of AAC is a consequence of the viscoelastic properties of the binder [10, 93], the evolution of the creep coefficient

of AAC should correlate with the viscoelastic properties and packing density of the alkali-activated binder. Therefore, the characterization of the pore structure of binder was studied to gain insights into the mechanical properties of the material. The curve-fitted relationship of compressive strength and total porosity of the alkali-activated pastes suggest a much lower 'intrinsic' strength (f_{01}) of AAC than of OPC paste. The value of f_{01} is a crucial microscale property that strongly correlates with the macroscale viscoelastic properties of the binder. Therefore, a lower intrinsic strength f_{01} appears to be one of the most likely reasons for the higher creep observed in AAC compared to OPC concrete. Manipulating the parameters of mixture design has the potential to significantly influence the intrinsic strength f_{01} of the material. However, further comprehensive research is warranted to elucidate the precise mechanisms underlying this property.

- In this study atomistic simulation of creep in C-S-H and C-A-S-H gels demonstrated that modification of the reaction products, i.e. the building block of the gel structure, namely a reduction of the length of the silicate chains and incorporation of extra Al molecules and free interlayer water into the molecular structure of tobermorite (C(-A)-S-H gel), dramatically affected the mechanical properties, creep magnitude and creep characteristic time. This is in line with the opinion of researchers who attributed creep to rearrangements of particles within the microstructure of the binder and can be described as a complex process of stress-induced local shear transformation (including sliding of gel layers) and atomic diffusion [114, 211].

- The model based on activation energy approach showed good agreement with the experimental data within the considered time range. The ageing factor C decreased linearly with an increase of BFS content in the concrete mixture and respectively with an increase of the 28-days compressive strength. The proportionality factor of the model p^*=0.3 (the same as for OPC concrete) provided a good fit for mixtures S100 and S70, and satisfactory fit for the S50 concrete mixture. Nevertheless, additional experimental research is required to establish the relationship between p^* and the precursors' composition, thus expanding the precision and limits of the model applicability.

Based on the results of the research presented in this thesis, some recommendations are given for adjustments of the EuroCode 2 creep model to make the code applicable for AAC:

1. Adopting a *creep enhancement factor* $\varphi_{0,AAC}$, to account for the higher ultimate creep of AAC mixtures compared to OPC mixtures. This creep enhancement factor is inserted into equation (7.7) for calculation of φ_0 and thus equal:

$$\varphi_0 = \varphi_{RH} \cdot \beta(f_{cm}) \cdot \beta(t_0) \cdot \varphi_{0,AAC}$$

$$\varphi_{0,AAC}(B/F) = 6.68 - 3.29 \cdot B/F \qquad \text{(for } 0.5 < B/F < 1.0, \text{ moist curing)}$$

$$\varphi_{0,AAC}(B/F) = 5.9 - 1.93 \cdot B/F \qquad \text{(for } 0.5 < B/F < 1.0, \text{ sealed curing)}$$

where B/F the precursor ratio BFS/(BFS+FA).

2. Adopting a *precursor-dependent* value of the power n in the rate factor $\beta_c(t,t_0)$:

$$\beta_c(t,t_0) = [(t - t_0)/(\beta_H + t - t_0)]^{\,n(B/F)}$$

n(B/F) = 0.581 · B/F + 0.053   (0.5 < B/F < 1.0, moist curing)

n(B/F) = 0.395 · B/F + 0.21   (0.5 < B/F < 1.0, sealed curing)

where B/F stands for the precursor ratio BFS/(BFS+FA).

3. In order to improve the applicability of the engineering code-type model, more creep test data is needed to consider the effects of other affecting factors, such as RH, temperature, age at the moment of loading, low strength (under 40 MPa), different loading levels, etc.

8.3   Further research

Further research is recommended to fully understand and predict the creep deformation of AAC.

- **Creep tests in sealed conditions.**

  One potential extension of this project could involve conducting creep tests on AAC under sealed conditions. In this research the creep tests were performed according to the Australian standard developed for OPC concrete [14]. In agreement with this standard, the creep tests and shrinkage test were performed in parallel on specimens exposed to 55% RH. However, due to the dense nature of the alkali-activated binder, the diffusion of water in AAC differs significantly from that in OPC, which significantly affects the interaction between shrinkage and creep of AAC. Creep tests on sealed specimens would enable the separation of basic creep and drying creep, providing valuable insights in the effect of the drying process on the creep of AAC. In the end, this information can be used for the calibration of the factors in the EC2 model that depend on RH.

- **The influence of liquid-to-binder ratio and curing conditions on creep in AAC.**

  Exploring the influence of the liquid-to-binder ratio on creep in AAC is a crucial research avenue. The l/b ratio and internal moisture significantly impact concrete creep by affecting the microstructure and creating humidity gradients, which in turn modify its viscoelastic properties. Unlike PC concrete, where the water-to-cement

ratio directly correlates with compressive strength, AAC shows a less straightforward relationship between the l/b ratio and mechanical properties. Investigating how variations of the l/b ratio impact the creep properties of AAC would yield valuable insights into understanding of creep mechanisms. Furthermore, a description of the interplay between the l/b ratio and creep behaviour in AAC can contribute to refining specific creep models.

- **The role of aggregates in creep development.**

  Another important direction of research is investigating the impact of utilizing various types and amount of aggregates in AAC. Previous research has shown that the interaction between the binder and aggregates in AAC differs significantly from that in OPC concrete [245, 246]. This dissimilarity arises from variations in material structure at micro- and nano- scales which might lead to unexpected correlations. Moreover, as the use of recycled aggregates in AAC is becoming more widespread due to its eco-friendliness, it is crucial to determine how such aggregates may affect creep behaviour. Further research in this area would not only help to identify more sustainable and cost-effective options for producing AAC, but also provide insight into how different aggregates may affect the long-term performance of concrete structures.

- **Evaluation of the effect of admixtures on creep.**

  Another promising direction for research could be the assessment of how various admixtures influence the creep behaviour of AAC. Admixtures like superplasticizers and silica fume are frequently used in concrete mixtures to improve their compressive strength and elastic modulus. However, the influence of the admixtures on creep behaviour of AAC remains uncertain yet. In our research, it was shown that the microstructure of the binder plays a substantial role in the viscoelastic properties of AAC. It is likely that specific admixtures might affect the nano- and microstructure of the paste, altering its intrinsic properties and, as a result of this, concrete creep. Further research on this topic will allow manipulation and prediction the creep properties of AAC by introducing specific admixtures into the concrete mixture design.

- **MD simulations of creep in (C-)N-A-S-H gel.**

  One more interesting area of scientific research involves the use of molecular dynamic simulations for exploring creep behaviour at the nanoscale of other alkali-activated binder phases, particularly the N-A-S-H and the C-N-A-S-H gels. The (C-)N-A-S-H gel, as a main reaction product of fly ash-based alkali-activated materials, is agreed to play a critical role in their mechanical properties. MD simulations offer a powerful tool for gaining insights into the deformation mechanisms at the molecular level, allowing for a deeper understanding of the impact of various parameters, such as Ca/Si ratio and water content on creep behaviour of the material.

References

1.	Spani, R.C., *The New Circular Economy Action Plan.* Briefs, 2020.

2.	Shi, C., A.F. Jiménez, and A. Palomo, *New cements for the 21st century: The pursuit of an alternative to Portland cement.* Cement and concrete research, 2011. **41**(7): p. 750-763.

3.	Whiting, J., *Manufacture of cement.* . 1895.

4.	Purdon, A., *The action of alkalis on blast-furnace slag.* Journal of the Society of Chemical Industry, 1940. **59**(9): p. 191-202.

5.	Glukhovsky, V., *Soil silicate-based products and structures.* Gosstroiizdat Publish, 1957.

6.	Provis, J.L., *Alkali-activated materials.* Cement and Concrete Research, 2018. **114**: p. 40-48.

7.	McLellan, B.C., et al., *Costs and carbon emissions for geopolymer pastes in comparison to ordinary portland cement.* Journal of cleaner production, 2011. **19**(9-10): p. 1080-1090.

8.	ECf, S., *Eurocode 2: Design of Concrete Structures‐Part 1‐1: General rules and rules for buildings.* 2002, EN 1995‐1‐1.

9.	Bazant, Z.P., et al., *Explanation of excessive long-time deflections of collapsed record-span box girder bridge in Palau.* Preliminary Report, 2008(08-09): p. A222e.

10.	Bažant, Z.P. and M. Jirásek, *Creep and hygrothermal effects in concrete structures.* Vol. 38. 2018: Springer.

11.	Li, Z., *Autogenous shrinkage of alkali-activated slag and fly ash materials From mechanism to mitigating strategies.*

12.	Provis, J.L. and S.A. Bernal, *Geopolymers and related alkali-activated materials.* Annual Review of Materials Research, 2014. **44**: p. 299-327.

13.	García-Lodeiro, I., et al., *Cimenturi hibride alcaline. Partea I: Fundamente*/hybrid alkaline cements. Part I: Fundamentals.* Revista Romana de Materiale, 2012. **42**(4): p. 330.

14.	Standard, A., *AS 1012.16: Determination of Creep of Concrete Cylinders in Compression.* 1996, Standards Australia, Sydney.

15.	Nedeljković, M., *Carbonation mechanism of alkali-activated fly ash and slag materials: In view of long-term performance predictions.* 2019.

16.	Bazant, Z.P., M.H. Hubler, and Q. Yu, *Pervasiveness of excessive segmental bridge deflections: Wake-up call for creep.* ACI Structural Journal, 2011. **108**(6): p. 766.

17.	Bazant, Z.P., Q. Yu, and G.-H. Li, *Excessive long-time deflections of prestressed box girders. I: Record-span bridge in Palau and other paradigms.* Journal of Structural Engineering, ASCE, 2012. **138**(6).

18.	Un, C.H., *Creep Behaviour of Geopolymer Concrete.* 2017.

19.   Davidovits, J., *Ancient and modern concretes: What is the real difference?* Concrete International, 1987. **9**(12): p. 23-28.

20.   Palomo, A., et al., *Hybrid binders: A journey from the past to a sustainable future (opus caementicium futurum).* Cement and Concrete Research, 2019. **124**: p. 105829.

21.   Kuehl, H., *Slag cement and process of making the same.* 1908, Google Patents.

22.   Glukhovsky, V., I. Pashkov, and G. Yavorsky, *New building material, in Russian.* Bull. Tech, Info. GlavKievStroy Kiev, 1957.

23.   Davidovits, J., *Synthetic Mineral Polymer Compound of The Silicoaluminates Family and Preparation Process, United States Patent-4,472,199 (pp. 1-12).* 1984, USA.

24.   Zhang, P., et al., *Fabrication and engineering properties of concretes based on geopolymers/alkali-activated binders-A review.* Journal of Cleaner Production, 2020. **258**: p. 120896.

25.   Krivenko, P., *Why alkaline activation–60 years of the theory and practice of alkali-activated materials.* Journal of Ceramic Science and Technology, 2017. **8**(3): p. 323-333.

26.   Lee, N. and H.-K. Lee, *Setting and mechanical properties of alkali-activated fly ash/slag concrete manufactured at room temperature.* Construction and Building Materials, 2013. **47**: p. 1201-1209.

27.   Duxson, P., et al., *Geopolymer technology: the current state of the art.* Journal of materials science, 2007. **42**(9): p. 2917-2933.

28.   Palomo, A., M. Grutzeck, and M. Blanco, *Alkali-activated fly ashes: A cement for the future.* Cement and concrete research, 1999. **29**(8): p. 1323-1329.

29.   Fernández-Jiménez, A. and F. Puertas, *Alkali-activated slag cements: kinetic studies.* Cement and concrete research, 1997. **27**(3): p. 359-368.

30.   Palomo, A. and F. Glasser, *Chemically-bonded cementitious materials based on metakaolin.* British ceramic. Transactions and journal, 1992. **91**(4): p. 107-112.

31.   Provis, J.L. and J.S. Van Deventer, *Alkali activated materials: state-of-the-art report, RILEM TC 224-AAM*. Vol. 13. 2013: Springer Science & Business Media.

32.   Falah, M. and K.J. MacKenzie, *Photocatalytic nanocomposite materials based on inorganic polymers (Geopolymers): a review.* Catalysts, 2020. **10**(10): p. 1158.

33.   Piatak, N.M., M.B. Parsons, and R.R. Seal II, *Characteristics and environmental aspects of slag: A review.* Applied Geochemistry, 2015. **57**: p. 236-266.

34.   Wang, G.C., *The utilization of slag in civil infrastructure construction*. 2016: Woodhead Publishing.

35.   Nedeljković, M., Z. Li, and G. Ye, *Setting, strength, and autogenous shrinkage of alkali-activated fly ash and slag pastes: Effect of slag content.* Materials, 2018. **11**(11): p. 2121.

36.   Pacheco-Torgal, F., J. Castro-Gomes, and S. Jalali, *Alkali-activated binders: A review: Part 1. Historical background, terminology, reaction mechanisms and hydration products.* Construction and building Materials, 2008. **22**(7): p. 1305-1314.

37.   Fernández-Jiménez, A., et al., *Alkaline activation of metakaolin–fly ash mixtures: Obtain of Zeoceramics and Zeocements.* Microporous and mesoporous materials, 2008. **108**(1-3): p. 41-49.

38.   Elimbi, A., H. Tchakoute, and D. Njopwouo, *Effects of calcination temperature of kaolinite clays on the properties of geopolymer cements.* Construction and Building Materials, 2011. **25**(6): p. 2805-2812.

39.   Kuenzel, C., et al., *Ambient temperature drying shrinkage and cracking in metakaolin‐based geopolymers.* Journal of the American Ceramic Society, 2012. **95**(10): p. 3270-3277.

40.   Wu, Y., et al., *Geopolymer, green alkali activated cementitious material: Synthesis, applications and challenges.* Construction and Building Materials, 2019. **224**: p. 930-949.

41.   Marvila, M.T., A.R.G.d. Azevedo, and C.M.F. Vieira, *Reaction mechanisms of alkali-activated materials.* Revista IBRACON de Estruturas e Materiais, 2021. **14**.

42.   Wattimena, O.K., Antoni, and D. Hardjito. *A review on the effect of fly ash characteristics and their variations on the synthesis of fly ash based geopolymer.* in *AIP Conference Proceedings.* 2017. AIP Publishing LLC.

43.   Fernández-Jiménez, A. and A. Palomo, *Composition and microstructure of alkali activated fly ash binder: Effect of the activator.* Cement and concrete research, 2005. **35**(10): p. 1984-1992.

44.   Fernández‐Jiménez, A., et al., *Structure of calcium silicate hydrates formed in alkaline‐activated slag: influence of the type of alkaline activator.* Journal of the American Ceramic Society, 2003. **86**(8): p. 1389-1394.

45.   Escalante‐García, J.I., et al., *Hydration products and reactivity of blast‐furnace slag activated by various alkalis.* Journal of the American Ceramic Society, 2003. **86**(12): p. 2148-2153.

46.   Bernal, S.A., et al., *Effect of silicate modulus and metakaolin incorporation on the carbonation of alkali silicate-activated slags.* Cement and Concrete Research, 2010. **40**(6): p. 898-907.

47.   Bernal, S.A., et al., *Evolution of binder structure in sodium silicate-activated slag-metakaolin blends.* Cement and Concrete Composites, 2011. **33**(1): p. 46-54.

48.   Bernal, S.A. and J.L. Provis, *Durability of alkali‐activated materials: progress and perspectives.* Journal of the American Ceramic Society, 2014. **97**(4): p. 997-1008.

49.   Abdolhosseini Qomi, M.J., F.J. Ulm, and R.J.M. Pellenq, *Evidence on the dual nature of aluminum in the calcium‐silicate‐hydrates based on atomistic simulations.* Journal of the American Ceramic Society, 2012. **95**(3): p. 1128-1137.

50.   Richardson, I.G., *Model structures for c-(a)-sh (i).* Acta Crystallographica Section B: Structural Science, Crystal Engineering and Materials, 2014. **70**(6): p. 903-923.

51.   Davidovits, J., *Geopolymers: inorganic polymeric new materials.* Journal of Thermal Analysis and calorimetry, 1991. **37**(8): p. 1633-1656.

52.   Ismail, I., et al., *Modification of phase evolution in alkali-activated blast furnace slag by the incorporation of fly ash.* Cement and Concrete Composites, 2014. **45**: p. 125-135.

53.   Samal, S. and I. Blanco, *An Application Review of Fiber-Reinforced Geopolymer Composite.* Fibers, 2021. **9**(4): p. 23.

54.   Criado, M., A. Fernández-Jiménez, and A. Palomo, *Alkali activation of fly ash. Part III: Effect of curing conditions on reaction and its graphical description.* Fuel, 2010. **89**(11): p. 3185-3192.

55.   García-Lodeiro, I., et al., *Compatibility studies between NASH and CASH gels. Study in the ternary diagram Na2O–CaO–Al2O3–SiO2–H2O.* Cement and Concrete Research, 2011. **41**(9): p. 923-931.

56.   Walkley, B., et al., *Phase evolution of C-(N)-ASH/NASH gel blends investigated via alkali-activation of synthetic calcium aluminosilicate precursors.* Cement and Concrete Research, 2016. **89**: p. 120-135.

57.   Bentz, D.P. and P.E. Stutzman, *Curing, hydration, and microstructure of cement paste.* ACI materials journal, 2006. **103**(5): p. 348.

58.   Ekolu, S., *A review on effects of curing, sheltering, and CO2 concentration upon natural carbonation of concrete.* Construction and Building Materials, 2016. **127**: p. 306-320.

59.   Yuwei, M., *Microstructure and Engineering Properties of Alkali Activated Fly Ash-as an environment friendly alternative to Portland cement.* TU Delft, Netherland, 2013.

60.   Collins, F. and J. Sanjayan, *Microcracking and strength development of alkali activated slag concrete.* Cement and Concrete Composites, 2001. **23**(4-5): p. 345-352.

61.   Aldea, C.-M., et al., *Effects of curing conditions on properties of concrete using slag replacement.* Cement and concrete research, 2000. **30**(3): p. 465-472.

62.   Chi, M., *Effects of dosage of alkali-activated solution and curing conditions on the properties and durability of alkali-activated slag concrete.* Construction and Building Materials, 2012. **35**: p. 240-245.

63.   Neville, A.M., *Properties of concrete*. Vol. 4. 1995: Longman London.

64.   Bernal, S.A., et al., *Effect of binder content on the performance of alkali-activated slag concretes.* Cement and concrete research, 2011. **41**(1): p. 1-8.

65.   Fernandez-Jimenez, A.M., A. Palomo, and C. Lopez-Hombrados, *Engineering properties of alkali-activated fly ash concrete.* ACI Materials Journal, 2006. **103**(2): p. 106.

66.   Ding, Y., J.-G. Dai, and C.-J. Shi, *Mechanical properties of alkali-activated concrete: A state-of-the-art review.* Construction and Building Materials, 2016. **127**: p. 68-79.

67.   Sun, B., G. Ye, and G. de Schutter, *A review: Reaction mechanism and strength of slag and fly ash-based alkali-activated materials.* Construction and Building Materials, 2022. **326**: p. 126843.

68.   Nath, P. and P.K. Sarker, *Effect of GGBFS on setting, workability and early strength properties of fly ash geopolymer concrete cured in ambient condition.* Construction and Building materials, 2014. **66**: p. 163-171.

69.   Yang, K.-H., A.-R. Cho, and J.-K. Song, *Effect of water–binder ratio on the mechanical properties of calcium hydroxide-based alkali-activated slag concrete.* Construction and Building Materials, 2012. **29**: p. 504-511.

70.   Sofi, M., et al., *Engineering properties of inorganic polymer concretes (IPCs).* Cement and concrete research, 2007. **37**(2): p. 251-257.

71.   Alexander, M. and T. Milne, *Influence of cement blend and aggregate type on the stress-strain behavior and elastic modulus of concrete.* Materials Journal, 1995. **92**(3): p. 227-235.

72.   Topçu, I.B., T. Bilir, and A.R. Boğa, *Estimation of the modulus of elasticity of slag concrete by using composite material models.* Construction and Building Materials, 2010. **24**(5): p. 741-748.

73.   Mithun, B. and M. Narasimhan, *Performance of alkali activated slag concrete mixes incorporating copper slag as fine aggregate.* Journal of Cleaner Production, 2016. **112**: p. 837-844.

74.   Hardjito, D., et al., *The stress-strain behaviour of fly ash-based geopolymer concrete.* Development in Mechanics of Structures and Materials, 2004. **35**: p. 831-834.

75.   Fang, G. and M. Zhang, *Multiscale micromechanical analysis of alkali-activated fly ash-slag paste.* Cement and Concrete Research, 2020. **135**: p. 106141.

76.   Hojati, M. and A. Radlińska, *Shrinkage and strength development of alkali-activated fly ash-slag binary cements.* Construction and Building Materials, 2017. **150**: p. 808-816.

77.   Prinsse, S., et al., *Time‐dependent material properties and reinforced beams behavior of two alkali‐activated types of concrete.* Structural Concrete, 2020. **21**(2): p. 642-658.

78.   Laidler, K.J., *The development of the Arrhenius equation.* Journal of chemical Education, 1984. **61**(6): p. 494.

79.   Wittmann, F., *Bestimmung physikalischer Eigenschaften des Zementsteins*. 1974.

80.   Klug, P. and F. Wittmann, *Activation energy and activation volume of creep of hardened cement paste.* Materials science and Engineering, 1974. **15**(1): p. 63-66.

81.   Bouquet, G., *Effect of relaxation on eigenstresses and microcracking in concrete under imposed deformation*. 2019, Delft University of Technology.

82.   Wittmann, F.H., *Fundamental research on creep and shrinkage of concrete*. 2012: Springer Science & Business Media.

83.   Van Breugel, K., *Relaxation of young concrete. Department of Structural Concrete, Faculty of Civil Engineering.* Delft University of Technology, Research Report, 1980(5-80): p. D8.

84.   Rabotnov, J., *Mechanics of the Deformable Solid (in Russisch)*. 1979, Nauka, Moskva.

85. Soderberg, C.R., *The interpretation of creep tests for machine design.* Trans. ASME, 1936. **58**(8): p. 733-743.

86. Nadai, A., *The influence of time upon creep, the hyperbolic sine creep law.* Stephen Timoshenko Anniversary, 1938. **1938**.

87. Naumenko, K., *Modeling of high-temperature creep for structural analysis applications.* 2006: Professional Thesis, Martin Luther University Halle-Wittenberg, Germany.

88. Bažant, Z.P., *Prediction of concrete creep and shrinkage: past, present and future.* Nuclear engineering and Design, 2001. **203**(1): p. 27-38.

89. Wittmann, F.H., *Creep and shrinkage mechanisms.* Creep and shrinkage in concrete structures, 1982: p. 129-161.

90. Neville, A.M., *Creep of plain and structural concrete.* 1983.

91. Bažant, Z.P. and S. Prasannan, *Solidification theory for concrete creep. I: Formulation.* Journal of engineering mechanics, 1989. **115**(8): p. 1691-1703.

92. Bažant, Z.P., et al., *Microprestress-solidification theory for concrete creep. I: Aging and drying effects.* Journal of Engineering Mechanics, 1997. **123**(11): p. 1188-1194.

93. Bažant, Z., P. Havlásek, and M. Jirásek. *Microprestress-solidification theory: Modeling of size effect on drying creep.* in *EURO-C 2014 Conference.* 2014.

94. Vandamme, M., Z.P. Bažant, and S. Keten, *Creep of lubricated layered nano-porous solids and application to cementitious materials.* Journal of Nanomechanics and Micromechanics, 2015. **5**(4): p. 04015002.

95. Sinko, R., et al., *Transient effects of drying creep in nanoporous solids: understanding the effects of nanoscale energy barriers.* Proceedings of the Royal Society A: Mathematical, Physical and Engineering Sciences, 2016. **472**(2191): p. 20160490.

96. Sinko, R., Z.P. Bažant, and S. Keten, *A nanoscale perspective on the effects of transverse microprestress on drying creep of nanoporous solids.* Proceedings of the Royal Society A: Mathematical, Physical and Engineering Sciences, 2018. **474**(2209): p. 20170570.

97. Rahimi-Aghdam, S., Z.P. Bažant, and G. Cusatis, *Extended microprestress-solidification theory for long-term creep with diffusion size effect in concrete at variable environment.* Journal of Engineering Mechanics, 2019. **145**(2): p. 04018131.

98. Ghosh, R., *A hypothesis on mechanism of maturing creep of concrete.* Matériaux et Construction, 1973. **6**: p. 23-27.

99. Timusk, J. and R. Ghosh. *Maturing creep of Portland cement paste.* in *Journal Proceedings.* 1971.

100. Bažant, Z.P., *Viscoelasticity of solidifying porous material—concrete.* Journal of the Engineering Mechanics Division, 1977. **103**(6): p. 1049-1067.

101. Bažant, Z.P., *Thermodynamics of solidifying or melting viscoelastic material.* Journal of the Engineering Mechanics Division, 1979. **105**(6): p. 933-952.

102.   Bažant, Z.P. and S. Prasannan, *Solidification theory for aging creep.* Cement and Concrete Research, 1988. **18**(6): p. 923-932.

103.   Jirásek, M. and P. Havlásek, *Microprestress–solidification theory of concrete creep: Reformulation and improvement.* Cement and Concrete Research, 2014. **60**: p. 51-62.

104.   Bažant, Z.P. and S. Baweja, *Justification and refinements of model B3 for concrete creep and shrinkage 1. statistics and sensitivity.* Materials and structures, 1995. **28**: p. 415-430.

105.   Bažant, Z.P. and G.-H. Li, *Comprehensive database on concrete creep and shrinkage.* Infrastructure Technology Institute, McCormick School of Engineering and Applied Science, Northwestern University, 2008.

106.   Bažant, Z.P. and L. Najjar, *Drying of concrete as a nonlinear diffusion problem.* Cement and concrete research, 1971. **1**(5): p. 461-473.

107.   Bažant, Z., *Constitutive equation for concrete creep and shrinkage based on thermodynamics of multiphase systems.* Matériaux et constructions, 1970. **3**: p. 3-36.

108.   Bažant, Z. and L. Najjar, *Nonlinear water diffusion in nonsaturated concrete.* Matériaux et Construction, 1972. **5**: p. 3-20.

109.   Jennings, H. and P. Tennis, *A model for two types of calcium silicate hydrate in the microstructure of Portland cement paste.* Cem Concr Res, 2000. **30**: p. 855-863.

110.   Jennings, H.M., *A model for the microstructure of calcium silicate hydrate in cement paste.* Cement and concrete research, 2000. **30**(1): p. 101-116.

111.   Feldman, R.F., *Mechanism of creep of hydrated Portland cement paste.* Cement and concrete research, 1972. **2**(5): p. 521-540.

112.   Powers, T., *The thermodynamics of volume change and creep.* Matériaux et construction, 1968. **1**(6): p. 487-507.

113.   Wu, S.T., *Creep and shrinkage in concrete structures: Edited by ZP Bazant and FH Wittmann. John Wiley & Sons, Ltd., 1982 (363 pp).* 1984, Pergamon.

114.   Haist, M., et al., *Creep in reactive colloidal gels: A nanomechanical study of cement hydrates.* Physical Review Research, 2021. **3**(4): p. 043127.

115.   Manzano, H., et al., *Shear deformations in calcium silicate hydrates.* Soft Matter, 2013. **9**(30): p. 7333-7341.

116.   Morshedifard, A., S. Masoumi, and M. Abdolhosseini Qomi, *Nanoscale origins of creep in calcium silicate hydrates.* Nature communications, 2018. **9**(1): p. 1-10.

117.   Puertas, F., et al., *A model for the CASH gel formed in alkali-activated slag cements.* Journal of the European Ceramic Society, 2011. **31**(12): p. 2043-2056.

118.   Li, J., W. Zhang, and P.J. Monteiro, *Preferred orientation of calcium aluminosilicate hydrate compacts: Implications for creep and indentation.* Cement and Concrete Research, 2021. **143**: p. 106371.

119.   Lolli, F., et al., *Molecular model of geopolymers with increasing level of disorder in the atomic structure.* 2018.

120. Chen, Y., et al., *A molecular dynamics study of N‐A‐S‐H gel with various Si/Al ratios.* Journal of the American Ceramic Society, 2022.

121. Bazant, Z.P. and F.H. Wittmann, *Creep and shrinkage in concrete structures.* 1982.

122. Neville, A.M. and J.J. Brooks, *Concrete technology.* Vol. 438. 1987: Longman Scientific & Technical England.

123. Bentz, D.P. and W.J. Weiss, *Internal curing: a 2010 state-of-the-art review.* 2011: US Department of Commerce, National Institute of Standards and Technology ….

124. Pickett, G. *The effect of change in moisture-content on the crepe of concrete under a sustained load.* in *Journal Proceedings.* 1942.

125. Wittmann, F. and P. Roelfstra, *Total deformation of loaded drying concrete.* Cement and Concrete Research, 1980. **10**(5): p. 601-610.

126. Iding, R. and B. Bresler, *Prediction of shrinkage stresses and deformations in concrete.* Fundamental research on creep and shrinkage of concrete, 1982: p. 341-352.

127. Altoubat, S.A. and D.A. Lange, *The Pickett effect at early age and experiment separating its mechanisms in tension.* Materials and Structures, 2002. **35**: p. 211-218.

128. Zhang, B., et al., *Shrinkage mechanisms and shrinkage-mitigating strategies of alkali-activated slag composites: A critical review.* Construction and Building Materials, 2022. **318**: p. 125993.

129. Collins, F. and J.G. Sanjayan, *Effect of pore size distribution on drying shrinking of alkali-activated slag concrete.* Cement and Concrete Research, 2000. **30**(9): p. 1401-1406.

130. Chen, H., et al., *Prediction of self-desiccation in low water-to-cement ratio pastes based on pore structure evolution.* Cement and concrete research, 2013. **49**: p. 38-47.

131. Lee, N., J.G. Jang, and H.-K. Lee, *Shrinkage characteristics of alkali-activated fly ash/slag paste and mortar at early ages.* Cement and Concrete Composites, 2014. **53**: p. 239-248.

132. Kumarappa, D.B., S. Peethamparan, and M. Ngami, *Autogenous shrinkage of alkali activated slag mortars: Basic mechanisms and mitigation methods.* Cement and Concrete Research, 2018. **109**: p. 1-9.

133. Ye, H. and A. Radlińska, *Shrinkage mechanisms of alkali-activated slag.* Cement and Concrete Research, 2016. **88**: p. 126-135.

134. Uppalapati, S. and Ö. Cizer, *Understanding the autogenous shrinkage in alkali-activated slag/fly-ash blends.* 2018.

135. Ma, J. and F. Dehn, *Shrinkage and creep behavior of an alkali‐activated slag concrete.* Structural Concrete, 2017. **18**(5): p. 801-810.

136. Gao, X., Q. Yu, and H. Brouwers, *Apply 29Si, 27Al MAS NMR and selective dissolution in identifying the reaction degree of alkali activated slag-fly ash composites.* Ceramics International, 2017. **43**(15): p. 12408-12419.

137. du Bétom, F.I., *Code-Type Models for Structural Behaviour of Concrete.* Fédération Internationale du Béton: Bulletin, Lausanne, Switzerland, 2013.

138. Un, C., et al., *Predictions of long-term deflection of geopolymer concrete beams.* Construction and Building Materials, 2015. **94**: p. 10-19.

139. Castel, A., et al., *Creep and drying shrinkage of a blended slag and low calcium fly ash geopolymer Concrete.* Materials and Structures, 2016. **49**(5): p. 1619-1628.

140. Müller, H.S., et al., *Concrete: treatment of types and properties in fib Model Code 2010.* Structural concrete, 2013. **14**(4): p. 320-334.

141. Walraven, J.C., *Model Code 2010-Final draft: Volume 1*. Vol. 65. 2012: fib Fédération internationale du béton.

142. Du, Y., et al., *Experimental study on creep of short performance-based alkali-activated concrete column.* Journal of Building Engineering, 2022. **60**: p. 105158.

143. *Methods of testing concrete -Determination of the drying shrinkage of concrete for samples prepared in the field or in the laboratory. AS 1012.15-2015.* 2015: Australia, Standards. .

144. Blackledge, G.F. and R. Binns, *Concrete practice*. 2002.

145. Grant Norton, M. and J.L. Provis, *1000 at 1000: Geopolymer technology—the current state of the art.* Journal of Materials Science, 2020. **55**(28): p. 13487-13489.

146. Nedeljković, M., Z. Li, and G. Ye, *Setting, Strength, and Autogenous Shrinkage of Alkali-Activated Fly Ash and Slag Pastes: Effect of Slag Content.* Materials, 2018. **11**(11).

147. Brooks, G., M. Hasan, and M. Rhamdhani. *Slag basicity: what does it Mean?* in *10th International Symposium on High-Temperature Metallurgical Processing*. 2019. Springer.

148. EN, B., *Cement-Part 1: Composition, Specifications and Conformity Criteria for Common Cements (BS EN 197-1).* British European Standards Specifications, 2011.

149. Oelkers, E.H., J. Schott, and J.-L. Devidal, *The effect of aluminum, pH, and chemical affinity on the rates of aluminosilicate dissolution reactions.* Geochimica et Cosmochimica Acta, 1994. **58**(9): p. 2011-2024.

150. Winnefeld, F., et al., *Influence of slag composition on the hydration of alkali-activated slags.* Journal of Sustainable Cement-Based Materials, 2015. **4**(2): p. 85-100.

151. International, A., *ASTM C618–19: Standard Specification for Coal Fly Ash and Raw or Calcined Natural Pozzolan for Use in Concrete.* Annual Book of ASTM Standards 2019, 2019.

152. Zuo, Y., *Experimental Study and Numerical Simulation of the Reaction Process and Microstructure Formation of Alkali-Activated Materials*. 2019, Delft University of Technology.

153. Wang, P., R. Trettin, and V. Rudert, *Effect of fineness and particle size distribution of granulated blast-furnace slag on the hydraulic reactivity in cement systems.* Advances in cement research, 2005. **17**(4): p. 161-167.

154. Garcia-Lodeiro, I., A. Palomo, and A. Fernández-Jiménez, *Crucial insights on the mix design of alkali-activated cement-based binders*, in *Handbook of alkali-activated cements, mortars and concretes*. 2015, Elsevier. p. 49-73.

155. *BS EN 12390 - Testing hardened concrete.* British Standards Institution, 2002.

156. ASTM, C., *Standard test method for static modulus of elasticity and Poisson's ratio of concrete in compression.* Annual book of ASTM standards, 2002. **4**: p. 469.

157. Cadoni, E., et al. *Behavior of plain concrete subjected to tensile loading at high strain-rate.* in *Proceedings of the 4th international conference on fracture mechanics of concrete and concrete structures.* 2001.

158. Hordijk, D. and H. Reinhardt, *Fracture of concrete in uniaxial tensile experiments as influenced by curing conditions.* Engineering Fracture Mechanics, 1990. **35**(4-5): p. 819-826.

159. Ross, C.A., et al., *Moisture and strain rate effects on concrete strength.* Materials Journal, 1996. **93**(3): p. 293-300.

160. Wittmann, F., *Interaction of hardened cement paste and water.* Journal of the American ceramic society, 1973. **56**(8): p. 409-415.

161. Wittmann, F.H., *Grundlage eines Modells zur beschreibung charakteristischer Eigenschaften des betons.* Deutscher Ausschuss für Stahlbeton, 1978(290).

162. Li, Z., et al., *Mechanisms of autogenous shrinkage of alkali-activated slag and fly ash pastes.* Cement and Concrete Research, 2020. **135**: p. 106107.

163. Shen, W., et al., *Magnesia modification of alkali-activated slag fly ash cement.* Journal of Wuhan University of Technology-Mater. Sci. Ed., 2011. **26**(1): p. 121-125.

164. Myers, R.J., et al., *The Role of Al in cross‐linking of alkali‐activated slag cements.* Journal of the American Ceramic Society, 2015. **98**(3): p. 996-1004.

165. Nedeljković, M., et al., *Effect of curing conditions on the pore solution and carbonation resistance of alkali-activated fly ash and slag pastes.* Cement and Concrete Research, 2019. **116**: p. 146-158.

166. Lura, P., O.M. Jensen, and J. Weiss, *Cracking in cement paste induced by autogenous shrinkage.* Materials and structures, 2009. **42**(8): p. 1089-1099.

167. Gilbert, R.I. and G. Ranzi, *Time-dependent behaviour of concrete structures.* 2010: CRC Press.

168. Acker, P. and F.-J. Ulm, *Creep and shrinkage of concrete: physical origins and practical measurements.* Nuclear engineering and design, 2001. **203**(2-3): p. 143-158.

169. Sagoe-Crentsil, K., T. Brown, and A. Taylor, *Drying shrinkage and creep performance of geopolymer concrete.* Journal of Sustainable Cement-Based Materials, 2013. **2**(1): p. 35-42.

170. Li, Z., et al. *Autogenous shrinkage of alkali-activated slag-fly ash pastes*. in *5th Int. Slag Valoris. Symp., Leuven*. 2017.

171. Li, Z., et al., *Mitigating the autogenous shrinkage of alkali-activated slag by metakaolin.* Cement and Concrete Research, 2019. **122**: p. 30-41.

172. Humad, A.M., et al., *The effect of blast furnace slag/fly ash ratio on setting, strength, and shrinkage of alkali-activated pastes and concretes.* Frontiers in Materials, 2019. **6**: p. 9.

173. Humad, A.M., et al., *Creep and long-term properties of alkali-activated swedish-slag concrete.* Journal of Materials in Civil Engineering, 2021. **33**(2).

174. Palacios, M. and F. Puertas, *Effect of shrinkage-reducing admixtures on the properties of alkali-activated slag mortars and pastes.* Cement and concrete research, 2007. **37**(5): p. 691-702.

175. Thomas, R., D. Lezama, and S. Peethamparan, *On drying shrinkage in alkali-activated concrete: Improving dimensional stability by aging or heat-curing.* Cement and Concrete Research, 2017. **91**: p. 13-23.

176. Bentz, D.P., E.J. Garboczi, and D.A. Quenard, *Modelling drying shrinkage in reconstructed porous materials: application to porous Vycor glass.* Modelling and Simulation in Materials Science and Engineering, 1998. **6**(3): p. 211.

177. Prinsse, S., *Alkali-activated concrete: development of material properties (strength and stiffness) and flexural behaviour of reinforced beams over time.* 2017.

178. Hojati, M., F. Rajabipour, and A. Radlińska, *Creep of alkali-activated cement mixtures.* Case Studies in Construction Materials, 2022. **16**: p. e00954.

179. Bažant, Z.P., A.B. Hauggaard, and S. Baweja, *Microprestress-solidification theory for concrete creep. II: Algorithm and verification.* Journal of Engineering Mechanics, 1997. **123**(11): p. 1195-1201.

180. Brooks, A.E. and K. Newman, *The structure of concrete and its behaviour under load: proceedings of an international conference, London, September 1965*. 1968: Cement & Concrete Association of Great Britain.

181. Bazant, Z.P. and S. Prasannan, *Solidification theory for concrete creep. I: Formulation.* Journal of engineering mechanics, 1989. **115**(8): p. 1691-1703.

182. Van Breugel, K., *Relaxation of young concrete.* Report Stevin Laboratory, Concrete Structures 5-80-D8, 1980.

183. Van Breugel, M. *Additional Remarks on the Risk of Cracking in Hardening Concrete*. in *Proceedings of Rilem International Conference on Concrete at Early Ages, Paris*. 1982.

184. Constantinides, G., F.-J. Ulm, and K. Van Vliet, *On the use of nanoindentation for cementitious materials.* Materials and structures, 2003. **36**(3): p. 191-196.

185. Hu, C. and Z. Li, *A review on the mechanical properties of cement-based materials measured by nanoindentation.* Construction and Building Materials, 2015. **90**: p. 80-90.

186. Ma, Y., G. Ye, and J. Hu, *Micro-mechanical properties of alkali-activated fly ash evaluated by nanoindentation.* Construction and Building Materials, 2017. **147**: p. 407-416.

187. Zhang, H., et al., *Experimentally validated multi-scale modelling scheme of deformation and fracture of cement paste.* Cement and Concrete Research, 2017. **102**: p. 175-186.

188. Oliver, W.C. and G.M. Pharr, *Measurement of hardness and elastic modulus by instrumented indentation: Advances in understanding and refinements to methodology.* Journal of materials research, 2004. **19**(1): p. 3-20.

189. Jennings, H.M., et al., *Characterization and modeling of pores and surfaces in cement paste: correlations to processing and properties.* Journal of Advanced Concrete Technology, 2008. **6**(1): p. 5-29.

190. Brunauer, S., P.H. Emmett, and E. Teller, *Adsorption of gases in multimolecular layers.* Journal of the American chemical society, 1938. **60**(2): p. 309-319.

191. Scrivener, K., R. Snellings, and B. Lothenbach, *A practical guide to microstructural analysis of cementitious materials*. Vol. 540. 2016: Crc Press Boca Raton, FL, USA:.

192. Gregg, S., *Adsorption of gases-tool for the study of the texture of solids*, in *Studies in Surface Science and Catalysis*. 1982, Elsevier. p. 153-164.

193. Constantinides, G. and F.-J. Ulm, *The effect of two types of CSH on the elasticity of cement-based materials: Results from nanoindentation and micromechanical modeling.* Cement and concrete research, 2004. **34**(1): p. 67-80.

194. Constantinides, G. and F.-J. Ulm, *The nanogranular nature of C–S–H.* Journal of the Mechanics and Physics of Solids, 2007. **55**(1): p. 64-90.

195. Mikhail, R. and S. Selmin, *Highway research board.* Spec. report, 1966. **90**: p. 123-134.

196. Thomas, J.J., H.M. Jennings, and A.J. Allen, *The surface area of cement paste as measured by neutron scattering: evidence for two CSH morphologies.* Cement and Concrete Research, 1998. **28**(6): p. 897-905.

197. Powers, T.C., *Physical properties of cement paste*. 1960.

198. Eden, N. and J. Bailey, *The mechanical properties and tensile failure mechanism of a high strength polymer modified Portland cement.* Journal of materials science, 1984. **19**: p. 2677-2690.

199. Ryshkewitch, E., *Compression strength of porous sintered alumina and zirconia: 9th communication to ceramography.* Journal of the American Ceramic Society, 1953. **36**(2): p. 65-68.

200. Soroka, I. and P.J. Sereda, *Interrelation of hardness, modulus of elasticity, and porosity in various gypsum systems.* Journal of the American Ceramic Society, 1968. **51**(6): p. 337-340.

201. Schiller, K., *Strength of porous materials.* Cement and Concrete Research, 1971. **1**(4): p. 419-422.

202. Rößler, M. and I. Odler, *Investigations on the relationship between porosity, structure and strength of hydrated portland cement pastes I. Effect of porosity.* Cement and Concrete Research, 1985. **15**(2): p. 320-330.

203. Carol, I. and Z.P. Bažant, *Viscoelasticity with aging caused by solidification of nonaging constituent.* Journal of engineering mechanics, 1993. **119**(11): p. 2252-2269.

204. Sousa Coutinho, A., *A contribution to the mechanism of concrete creep.* Matériaux et Construction, 1977. **10**: p. 3-16.

205. Siebenbürger, M., M. Ballauff, and T. Voigtmann, *Creep in colloidal glasses.* Physical review letters, 2012. **108**(25): p. 255701.

206. Sentjabrskaja, T., et al., *Creep and flow of glasses: Strain response linked to the spatial distribution of dynamical heterogeneities.* Scientific reports, 2015. **5**(1): p. 1-11.

207. Cao, P., M.P. Short, and S. Yip, *Understanding the mechanisms of amorphous creep through molecular simulation.* Proceedings of the National Academy of Sciences, 2017. **114**(52): p. 13631-13636.

208. Liu, C., K. Martens, and J.-L. Barrat, *Mean-field scenario for the athermal creep dynamics of yield-stress fluids.* Physical Review Letters, 2018. **120**(2): p. 028004.

209. BOWMAN, E.T. and K. Soga, *Creep, ageing and microstructural change in dense granular materials.* Soils and foundations, 2003. **43**(4): p. 107-117.

210. Vandamme, M. and F.-J. Ulm, *Nanogranular origin of concrete creep.* Proceedings of the National Academy of Sciences, 2009. **106**(26): p. 10552-10557.

211. Morshedifard, A., S. Masoumi, and M. Abdolhosseini Qomi, *Nanoscale origins of creep in calcium silicate hydrates.* Nature communications, 2018. **9**(1): p. 1785.

212. Duque-Redondo, E., P.A. Bonnaud, and H. Manzano, *A comprehensive review of CSH empirical and computational models, their applications, and practical aspects.* Cement and Concrete Research, 2022. **156**: p. 106784.

213. Argon, A., *Plastic deformation in metallic glasses.* Acta metallurgica, 1979. **27**(1): p. 47-58.

214. Spaepen, F., *A microscopic mechanism for steady state inhomogeneous flow in metallic glasses.* Acta metallurgica, 1977. **25**(4): p. 407-415.

215. Newlands, K.C., et al., *Early stage dissolution characteristics of aluminosilicate glasses with blast furnace slag‐and fly‐ash‐like compositions.* Journal of the American Ceramic Society, 2017. **100**(5): p. 1941-1955.

216. Myers, R.J., et al., *Generalized structural description of calcium–sodium aluminosilicate hydrate gels: the cross-linked substituted tobermorite model.* Langmuir, 2013. **29**(17): p. 5294-5306.

217. Jiao, D. and G. De Schutter, *Insights into the viscoelastic properties of cement paste based on SAOS technique.* Construction and Building Materials, 2022. **357**: p. 129320.

218. Sanchez, F. and K. Sobolev, *Nanotechnology in concrete–a review.* Construction and building materials, 2010. **24**(11): p. 2060-2071.

219. González, M., *Force fields and molecular dynamics simulations.* École thématique de la Société Française de la Neutronique, 2011. **12**: p. 169-200.

220. Bonaccorsi, E., S. Merlino, and A.R. Kampf, *The crystal structure of tobermorite 14 Å (plombierite), a C–S–H phase.* Journal of the American Ceramic Society, 2005. **88**(3): p. 505-512.

221. Pellenq, R.J.-M., et al., *A realistic molecular model of cement hydrates.* Proceedings of the National Academy of Sciences, 2009. **106**(38): p. 16102-16107.

222. Abdolhosseini Qomi, M., et al., *Combinatorial molecular optimization of cement hydrates.* Nature communications, 2014. **5**(1): p. 4960.

223. Yan, Y., et al., *Effect of alkali hydroxide on calcium silicate hydrate (CSH).* Cement and Concrete Research, 2022. **151**: p. 106636.

224. Kapeluszna, E., et al., *Incorporation of Al in CASH gels with various Ca/Si and Al/Si ratio: Microstructural and structural characteristics with DTA/TG, XRD, FTIR and TEM analysis.* Construction and Building Materials, 2017. **155**: p. 643-653.

225. Fan, D. and S. Yang, *Mechanical properties of CSH globules and interfaces by molecular dynamics simulation.* Construction and Building Materials, 2018. **176**: p. 573-582.

226. Geng, G., et al., *Aluminum-induced dreierketten chain cross-links increase the mechanical properties of nanocrystalline calcium aluminosilicate hydrate.* Scientific reports, 2017. **7**(1): p. 44032.

227. Wang, J., et al., *Effect of Ca/Si and Al/Si on micromechanical properties of C (-A)-SH.* Cement and Concrete Research, 2022. **157**: p. 106811.

228. Kittel, C. and P. McEuen, *Introduction to solid state physics*. 2018: John Wiley & Sons.

229. Van Duin, A.C., et al., *ReaxFF: a reactive force field for hydrocarbons.* The Journal of Physical Chemistry A, 2001. **105**(41): p. 9396-9409.

230. Manzano, H., et al., *Hydration of calcium oxide surface predicted by reactive force field molecular dynamics.* Langmuir, 2012. **28**(9): p. 4187-4197.

231. Van Duin, A.C., et al., *ReaxFFSiO reactive force field for silicon and silicon oxide systems.* The Journal of Physical Chemistry A, 2003. **107**(19): p. 3803-3811.

232. Joshi, K.L., et al., *Reactive molecular simulations of protonation of water clusters and depletion of acidity in H-ZSM-5 zeolite.* Physical Chemistry Chemical Physics, 2014. **16**(34): p. 18433-18441.

233. Gale, J., *GULP manual.* GULP manual, 1998.

234. Fletcher, R., *Practical methods of optimization*. 2013: John Wiley & Sons.

235. Bauchy, M., et al., *Topological control on the structural relaxation of atomic networks under stress.* Physical review letters, 2017. **119**(3): p. 035502.

236. Pellenq, R.-M., N. Lequeux, and H. Van Damme, *Engineering the bonding scheme in C–S–H: The iono-covalent framework.* Cement and Concrete Research, 2008. **38**(2): p. 159-174.

237. Gibbs, G., *The thermodynamics of creep deformation.* physica status solidi (b), 1964. **5**(3): p. 693-696.

238. Baranikumar, A., C.E. Torrence, and Z. Grasley, *Thermorheological approach to predict long-term creep of cement mortar from short-term tests.* Mechanics of Time-Dependent Materials, 2022. **26**(2): p. 289-307.

239. Kai, M., L. Zhang, and K. Liew, *New insights into creep characteristics of calcium silicate hydrates at molecular level.* Cement and Concrete Research, 2021. **142**: p. 106366.

240. Eyring, H., *The activated complex and the absolute rate of chemical reactions.* Chemical Reviews, 1935. **17**(1): p. 65-77.

241. Vandamme, M., *Two models based on local microscopic relaxations to explain long-term basic creep of concrete.* Proceedings of the Royal Society A, 2018. **474**(2220): p. 20180477.

242. Krausz, A.S. and H. Eyring, *Deformation kinetics.* 1975: Wiley.

243. Lyu, W., *Effect of micro-cracking and self-healing on long-term creep and strength development of concrete.* 2020.

244. Wittmann, F.H., *Useful fundamentals of shrinkage and creep of concrete*, in *CONCREEP 10*. 2015. p. 84-93.

245. Ji, T., et al., *Interfacial transition zone of alkali-activated slag concrete.* ACI Materials Journal, 2017. **114**(3): p. 347.

246. Lee, W. and J. Van Deventer, *The interface between natural siliceous aggregates and geopolymers.* Cement and Concrete Research, 2004. **34**(2): p. 195-206.

245. F.G. Collins, J.G. Sanjayan, *Workability and mechanical properties of alkali activated slag concrete,* Cem. Concr. Res. **29** (1999) 455–458

246. M.R. Islam, *Creep and shrinkage behavior of fly ash based geopolymer concrete*, (2015).

247. C. Gunasekera, S. Setunge, D.W. Law, *Creep and drying shrinkage of different fly-ash-based geopolymers*, ACI Mater. J. **116** (2019) 39–49

248. S.E. Wallah, B.V. Rangan, *Low-calcium fly ash-based geopolymer concrete: long-term properties.* Research Report GC 2, Faculty of Engineering, Curtin University of Technology, Perth, Australia, 2006.

249. X. Zhou, Y. Wang, W. Zheng, P. Chen, Y. Zeng, *Effect of stress--strength ratio on creep property of sodium silicate--based alkali-activated slag concrete*, Appl. Sci. **9** (2019) 3643.

250. H. Le Chatelier, *Sur les changements de volume qui accompagnent le durcissement des ciments*, Bull. Soc. l´encouragagement Pour l´industrie Natl. 5 (1900)

251. H. E. Davis, *Autogenous volume change of concrete.* Proc. ASTM, 40. (1940) 1103–1110.

252. H. A. Neville, H. C. Jones, *The study of hydration changes by a volume–change method*, in Colloid Symp. Monogr. VI (1928) 309–318.

253. A.M. Neville, *Creep in concrete*: *plain, reinforced, and prestressed.* 1971: North Holland Publishing Co.

254. Nikhil Awasthy, Erik Schlangen, Dick Hordijk, Branko Šavija, Mladena Luković, *The role of eigen-stresses on apparent strength and stiffness of normal, high strength, and ultra-*

high performance fibre reinforced concrete. Developments in the Built Environment, 2023. Volume **16**, 100277, ISSN 2666-1659

Summary

Climate change is the main global concern today, triggering a transformative shift in several sectors, especially the construction industry. High carbon emissions during Portland cement (PC) production necessitate a gradual shift toward more environmentally friendly alternatives, such as alkali-activated materials (AAMs). AAMs offer a promising, low-carbon solution for the production of alternative building materials. Introduction of these materials, however, require certification backed by well-documented test results. The widely used EuroCode 2 (EN 1995-1-1) (EC2) for PC concrete currently lacks guidelines for the use of AAC. Experimental data and reliable models for estimating long-term mechanical properties, especially creep and shrinkage phenomena, are still missing. The aim of this thesis is to evaluate creep behaviour of AAC, clarify underlying mechanisms and develop a creep model that takes into account specific microstructural and nanoscale properties of alkali-activated paste.

The research started with an experimental study of mechanical properties of AAC mixtures, analysing compressive strength, splitting tensile strength, and elastic modulus compared to the standard PC concrete C65 at different ages. AAC mixtures showed the ability to match the strength of C65, but showed lower elastic modulus and splitting tensile strength. Mixtures containing a blend of slag and fly ash showed a reduced compressive strength, splitting tensile strength, and elastic modulus of samples cured under moist and sealed conditions during the first 28 days after casting. While AAC specimens cured in sealed conditions initially showed higher strength than moist cured specimens, prolonged storage at 55% relative humidity reduced the initial curing effects. Over time, the compressive strength of AAC stabilized after an initial increase, while the elastic modulus and splitting tensile strength peaked around 28 days and decreased by 20-30% on day 90 at 55% RH, in contrast to the stable properties of the C65 under similar humidity conditions.

Long-term creep and free shrinkage tests were then performed on AAC mixtures alongside the C65 concrete. AAC mixtures showed significantly higher creep than the PC reference concrete, with the AAC creep curves showing a continuous increase, even beyond a year under load, unlike C65. Despite similar 28-day compressive strength and elastic modulus, there was no clear correlation between mechanical properties and creep coefficient. All AAC mixtures showed significantly higher creep coefficients than the reference PC concrete, despite similar strength and modulus of elasticity. Moreover, the free shrinkage of AAC specimens, stored at 55% RH until the age of 28 days, was generally higher than that of the C65. The shrinkage strain increased rapidly until a specific value ε_0 was reached and then continued to increase at a slower rate.

The complex creep mechanisms in alkali-activated pastes were then investigated and discussed, with the evolution of their microstructure and nanoscale elastic modulus being examined for different FA/BFS ratios. Several test methods, including nanoindentation, N_2 adsorption and XRD analyses, were used to investigate these specific mechanisms. XRD analysis revealed the stability of crystalline phases in the alkali-activated materials over

time, while nanoindentation and N_2 adsorption tests indicated the formation of new material filling the pores in these pastes. The research revealed the dependency of the nanoscale elastic modulus of alkali-activated pastes on the composition of the precursor. Moreover, the tests indicated that mixing slag with fly ash affected the porosity of the paste, affecting the pore size distribution and maximum pore size. Over time, changes in pore volume and pore size distribution were observed, which correlated with changes in the elastic modulus at the nanoscale.

The next step of the project focused on molecular dynamic simulations for investigating the creep behaviour in alkali-activated reaction products. These simulations used the incremental stress-marching technique to explore the creep behaviour of C-S-H and C-A-S-H gels at a molecular level, with the aim to understand the impact of the gel structure on creep. The results indicated that reducing the length of silicate chains in the molecular structure of tobermorite led to a decrease in its modulus of elasticity. Shortening the silicate chains increased the ultimate creep values and reduced the characteristic time of the creep process. The incorporation of Al into the molecular structure of tobermorite increased the elastic modulus E and shear modulus G of the structure. Therefore, the virtual structures with higher Al/Si ratio showed lower creep values and slower creep development. These results support the assumption that creep of concrete depends on the Ca/Si ratio and Al/Si ratio of the C(-A)-S-H gel. Furthermore, the amount of interlayer water had a significant effect on the creep behaviour of modelled C-A-S-H structures. Adding extra water molecules in the interlayer space amplified creep strain and accelerated the characteristic time of the creep process.

Finally, two different creep models were proposed for describing the creep of AAC. The first model uses the activation energy approach and describes the creep evolution with a power function with an aging factor C and a time exponent p. A fitting procedure was carried out to determine these factors as a function of AAC mixture composition, in particular the precursor ratio. The second model adapted the EC2 creep model, originally designed for OPC concrete. The adaptation accounted for higher observed creep in AAC compared to OPC concrete at equivalent strength and included the dependence of creep coefficient rate on AAC's precursor ratio. The proposed modifications involved an enhancement factor $\varphi_{0,AAC}$ for the creep coefficient and a linear relationship between the power function coefficient and the precursor ratio. Calibration of these adjustments was conducted using six measured creep curves for AAC, which included moist and sealed curing.

Samenvatting

Klimaatverandering is vandaag de dag de belangrijkste wereldwijde zorg, die aanleiding geeft tot transities in verschillende sectoren, met name ook in de bouwindustrie. Hoge koolstofemissies tijdens de productie van Portlandcement (PC) vereisen een geleidelijke overgang naar meer milieuvriendelijke alternatieven, zoals alkali-geactiveerde materialen (AAM's). AAM's bieden een veelbelovende, koolstofarme oplossing voor de productie van alternatieve bouwmaterialen. De introductie van deze materialen vereist echter certificering die wordt ondersteund door goed gedocumenteerde testresultaten. De veelgebruikte EuroCode 2 (EN 1995-1-1) (EC2) voor PC-beton ontbeert momenteel richtlijnen voor het gebruik van AAC. Experimentele gegevens en betrouwbare modellen voor het bepalen van de mechanische eigenschappen, met name langetermijn kruip en krimpverschijnselen, ontbreken nog steeds. Het doel van dit proefschrift is om het kruipgedrag van AAC te onderzoeken, de onderliggende mechanismen te verduidelijken en een kruipmodel te ontwikkelen dat rekening houdt met specifieke eigenschappen van alkali-geactiveerde materialen op micro- en nano schaal.

De studie begint met een experimenteel onderzoek naar de mechanische eigenschappen van AAC-mengsels, waarbij de druksterkte, de splijttreksterkte en de elasticiteitsmodulus worden geanalyseerd en vergeleken met standaard PC-beton C65 op verschillende leeftijden. AAC-mengsels evenaarden de druksterkte van C65 mengsels, maar vertoonden een lagere elasticiteitsmodulus en splijttreksterkte. Mengsels met een combinatie van slakken en vliegas vertoonden een lagere druksterkte, splijttreksterkte en elasticiteitsmodulus gedurende de eerste 28 dagen na storten verharden onder water-verzadigde en verzegelde omstandigheden. AAC-proefstukken die onder verzegelde omstandigheden verhardden vertoonden aanvankelijk een hogere sterkte dan proefstukken die verharden onder waterverzadigde omstandigheden. Bij langdurige opslag bij 55% relatieve vochtigheid verdwenen het effect van de initiële verhardingscondities. Na verloop van tijd stabiliseerde de druksterkte van AAC. De elasticiteitsmodulus en de splijttreksterkte piekten rond dag 28 en namen vervolgens met 20% tot 30% af op dag 90, in tegenstelling tot de stabiele eigenschappen van de C65 onder vergelijkbare vochtigheidsomstandigheden.

Vervolgens werden langetermijn kruip- en krimpproeven uitgevoerd op zowel AAC-mengsels als C65-beton. AAC-mengsels vertoonden aanzienlijk hogere kruip dan het PC-referentiebeton. De kruipcurves van AAC lieten een voortdurende stijging zien, zelfs na meer dan een jaar onder belasting, in tegenstelling tot C65. Ondanks vergelijkbare druksterkte en elasticiteitsmodulus na 28 dagen was er geen duidelijk verband tussen mechanische eigenschappen en de kruipcoëfficiënt. Alle AAC-mengsels vertoonden significant hogere kruipcoëfficiënten dan het referentie-PC-beton, ondanks vergelijkbare sterkte en elasticiteitsmodulus. Bovendien was de vrije krimp van AAC-monsters, verhard bij 55% RV gedurende de eerste 28 dagen na storten, over het algemeen hoger dan die van de C65. De krimp nam snel toe tot een specifieke waarde ε_0 werd bereikt en bleef daarna in een langzamer tempo toenemen.
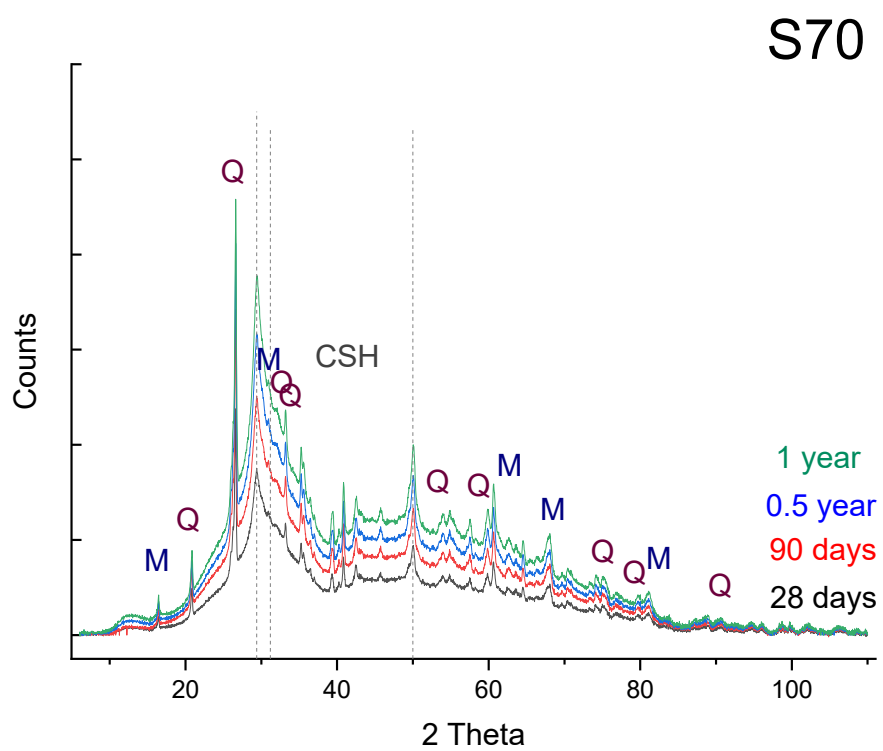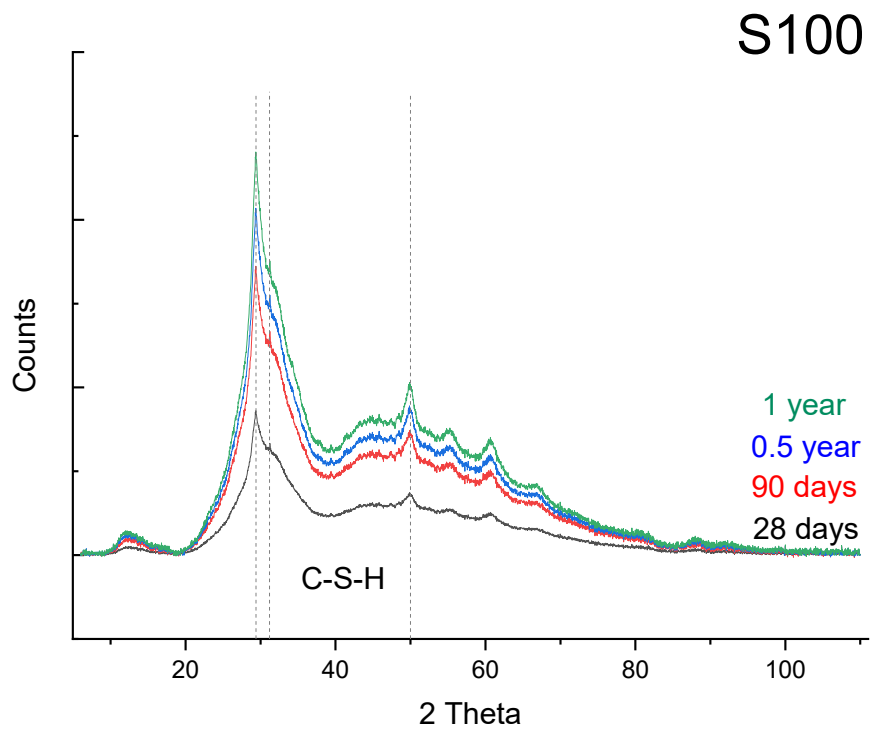
De complexe kruipmechanismen in alkali-geactiveerde pasta's werden vervolgens onderzocht en besproken, waarbij de ontwikkeling van de microstructuur en elasticiteitsmodulus (nanoschaal) werden onderzocht voor mengsels met verschillende FA/BFS-verhoudingen. Diverse testmethoden, waaronder nano-indentatie, N_2-adsorptie en XRD-analyses, werden gebruikt om deze specifieke mechanismen te onderzoeken. XRD-analyse onthulde de stabiliteit van kristallijne fasen in alkali-geactiveerde materialen, terwijl nano-indentatie en N2-adsorptieproeven de vorming van nieuw materiaal aantoonden in de poriën van de microstructuur. Het onderzoek toonde aan dat de (nanoschaal) elasticiteitsmodulus van alkali-geactiveerde pasta's afhankelijk is van de samenstelling van de precursor. Bovendien gaven de proefresultaten aan dat het mengen van slakken met vliegas invloed had op de porositeit van de pasta, wat de verdeling van de poriegrootte en maximale poriegrootte beïnvloedde. In de loop van de tijd werden veranderingen in het porievolume en de verdeling van de poriegrootte waargenomen, die correleerden met veranderingen in de elasticiteitsmodulus op nanoschaal.

De volgende stap van het project richtte zich op 'molecular dynamic (MD)' simulaties om het kruipgedrag in alkali-geactiveerde reactieproducten te onderzoeken. Deze simulaties gebruikten de incrementele stress-marching techniek om het kruipgedrag van C-S-H en C-A-S-H gels op moleculair niveau te verkennen, met als doel het begrijpen van de impact van de gelstructuur op kruip. De resultaten gaven aan dat het verminderen van de lengte van silicaatketens in de moleculaire structuur van tobermoriet leidde tot een afname van de elasticiteitsmodulus. Het verkorten van de silicaatketens verhoogde de uiteindelijke kruipwaarden en verminderde de karakteristieke tijd van het kruipproces. Opname van Al in de moleculaire structuur van tobermoriet verhoogde de elasticiteitsmodulus E en schuifmodulus G van de structuur. Daarom vertoonden virtuele structuren met een hogere Al/Si-verhouding een lagere kruip en langzamere ontwikkeling van de kruip. Deze resultaten ondersteunen de veronderstelling van de afhankelijkheid van het kruipgedrag van beton van de Ca/Si-verhouding en Al/Si-verhouding van de C(-A)-S-H-gel. Bovendien had de hoeveelheid tussenlaagwater (Eng.: interlayer water) een aanzienlijk effect op het kruipgedrag van gemodelleerde C-A-S-H-structuren. Het toevoegen van extra watermoleculen in de tussenlaag vergrootte de kruipvervorming en verkortte de karakteristieke tijd van het kruipproces.
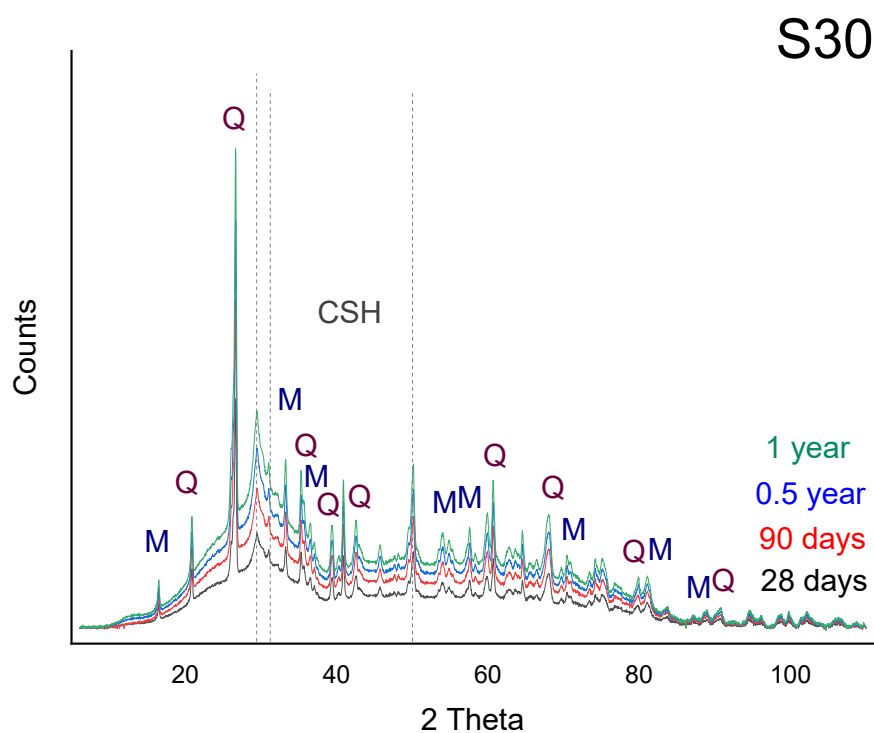
Tenslotte werden twee verschillende kruipmodellen voorgesteld om het kruipgedrag van AAC te beschrijven. Het eerste model is gebaseerd op het activeringsenergie concept en beschrijft het kruipgedrag met een machtsfunctie met een verouderingsfactor C en een tijdexponent p. Een fit-procedure werd uitgevoerd om deze factoren te bepalen als functie van de samenstelling van het AAC-mengsel, met name de precursorsamenstelling (i.c. verhouding slag/vliegas). Het tweede model paste het EC2-kruipmodel aan, oorspronkelijk ontworpen voor PC-beton. De aanpassing hield rekening met een hogere waargenomen kruip in AAC vergeleken met PC-beton bij vergelijkbare sterkte en omvatte de afhankelijkheid van de kruipcoëfficiënt van de precursorsamenstelling van AAC. De voorgestelde wijzigingen omvatten een vergrotingsfactor $\varphi_{0,AAC}$ voor de kruipcoëfficiënt en een lineaire relatie tussen de coëfficiënt van kruipfunctie (i.c. een machtsfunctie) en de precursorsamenstelling. De kalibratie van deze aanpassingen werd uitgevoerd op basis

van zes gemeten kruipkrommen voor AAC, gemeten aan waterverzadigde en verzegelde proefstukken.

A. XRD results

S100

C-S-H

1 year
0.5 year
90 days
28 days

S70

Q

M
CSH
Q
Q

M
Q
Q
M
M

Q
Q
M
Q

1 year
0.5 year
90 days
28 days

Figure A. XRD patterns of AAS and AASF pastes (S100, S70, S50 and S30) cured in sealed conditions at T=21 °C for 28 days, 90 days, 0.5 year and 1 year. CSH, M and Q stand for Calcium Silicate Hydrate, mullite and quartz, respectively.

CURRICULUM VITAE

PERSONAL INFORMATION

Name: Albina Kostiuchenko
Place of birth: Saint-Petersburg, Russia
Date of birth: 22 November 1992
Email: albina.a.kostiuchenko@gmail.com

EDUCATION AND WORK EXPERIENCE

- September 2009–June 2013: B.Sc. in Applied Mechanics
Faculty of Physics and Mechanics
Polytechnical University of St-Petersburg, Russia

- September 2015–June 2017 M.Sc. in Applied Physics,
Faculty of Applied Science
ITMO University, St-Petersburg, Russia

- October 2017–February 2022 Ph.D. Researcher,
Faculty of Civil Engineering and Geosciences
Delft University of Technology, The Netherlands